

# NAVIGATING REACTOR SAFETY IN CATALYTIC MICROCHANNEL REACTORS

by

**Sudipta Chattopadhyay**

B. Tech in Chemical Engineering, University of Calcutta, India, 1997

M. E in Chemical Engineering, Jadavpur University, India, 1999

Submitted to the Graduate Faculty of

School of Engineering in partial fulfillment

of the requirements for the degree of

Doctor of Philosophy

University of Pittsburgh

2004

**UNIVERSITY OF PITTSBURGH**  
**SCHOOL OF ENGINEERING**

This dissertation was presented

by

**Sudipta Chattopadhyay**

It was defended on

November 22<sup>nd</sup>, 2004

and approved by

Götz Vesper, Professor, Chemical and Petroleum Engineering Department

Irving Wender, Professor, Chemical and Petroleum Engineering Department

Robert M. Enick, Professor, Chemical and Petroleum Engineering Department

George Gallaher, Professor, Sunoco Chemical Company

Dissertation Director: **Götz Vesper**, Professor, Chemical and Petroleum Engineering

# NAVIGATING REACTOR SAFETY IN CATALYTIC MICROCHANNEL REACTORS

Sudipta Chattopadhyay, PhD

University of Pittsburgh, 2004

High temperature catalytic reactions are being intensely studied since many decades due to their large industrial potential, such as in pyrolysis, total oxidation (i.e. combustion) and partial oxidation of hydrocarbons. The reactions are characterized by extreme reaction temperatures ( $T > 1000^{\circ}\text{C}$ ) where homogeneous (i.e. non-catalytic gas phase) reactions can occur in parallel to catalytic reactions. This occurrence of homogeneous reactions is typically an undesired feature, since it complicates the understanding of reaction mechanisms, leads to selectivity losses, and often poses a safety hazard due to potentially explosive behavior [1]. Since free surfaces tend to bind radical species, eventually lead to a quenching of gas-phase reactions.

Microreactors, i.e. chemical reactors with characteristic dimensions in the sub-millimeter range, hold great promise for fundamental studies of existing processes offering small thermal inertia, high heat and mass transport rates, compactness etc. Due to their large surface-to-volume ratio, microreactors can be expected to suppress undesirable gas phase reactions and thus form safe reactor configurations for highly explosive processes.

In the present study, we numerically investigate the reactive flow of  $\text{H}_2/\text{air}$  mixtures in a microchannel to gain insights into the reason for the absence of explosion observed in previous experiments [2, 3]. The  $\text{H}_2$  oxidation reaction is chosen as model reaction due to its high exothermicity and wide flammability range. It also constitutes an important sub-set of reactions in hydrocarbon oxidation.

In a two-dimensional boundary layer numerical model, we used coupled mechanisms with detailed elementary-step kinetics for gas-phase and catalytic surface reactions. The influence of different wall materials, reactor dimension, feed conditions and reaction pressure on the coupling of heterogeneous and homogeneous reaction pathways in the microreactor was studied. The results demonstrate that the attainability of ‘intrinsic safety’ in microchannel reactors is strongly dependent on a complex interplay between homogeneous and heterogeneous reaction pathways in the individual reaction system. In particular, it is found that intrinsic reactor safety breaks down at sufficiently high reactor pressure. Generalized equations for the current reaction systems are derived.

As an outlook, other industrially relevant reaction systems, i.e. CO oxidation and NO<sub>x</sub> formation, are preliminary investigated with respect to the effect of heterogeneous-homogeneous interactions and radical quenching in particular, on the behaviour of these reaction systems.

## TABLE OF CONTENTS

ACKNOWLEDGEMENTS .....	xvii
1.0 INTRODUCTION .....	1
2.0 FUNDAMENTALS .....	6
2.1 MICROCHEMICAL SYSTEMS.....	6
2.2 IGNITION STUDIES .....	8
2.3 REACTOR SIMULATIONS.....	11
3.0 NUMERICAL SIMULATION.....	14
3.1 REACTOR MODEL.....	14
3.2 KINETIC MODEL .....	16
3.2.1 Gas Phase Chemistry .....	16
3.2.2 Surface Chemistry.....	17
3.3 SIMULATION PARAMETERS & NUMERICS .....	18
4.0 SIMULATION RESULTS & DISCUSSION: H <sub>2</sub> OXIDATION IN MICROCHANNEL REACTORS.....	20
4.1 ISOTHERMAL CALCULATION: REFERENCE CASE - INERT WALL .....	20
4.2 ISOTHERMAL CALCULATION: CATALYTIC MATERIAL - PLATINUM.....	25
4.2.1 Influence of catalyst on ignition behavior .....	25
4.2.2 Size effect in a Pt-microchannel reactor .....	29
4.2.3 Variation of Catalyst Loading.....	36
4.2.4 Limits of reactor safety .....	39
4.2.5 Influence of equivalence ratio on ignition .....	53
4.2.6 Influence of oxidant .....	55

4.2.7	Influence of reactor geometry.....	58
4.3	ISOTHERMAL CALCULATION: CATALYTIC MATERIALS – PALLADIUM...	60
4.3.1	Effect of wall material on ignition behavior.....	61
4.3.2	Size effects in a Pd-microchannel reactor.....	64
4.3.3	Limits of reactor safety: Pt vs. Pd.....	66
4.4	ISOTHERMAL CALCULATION: NON-CATALYTIC MATERIAL - ‘RADICAL RECOMBINATION’.....	68
4.4.1	Ignition in H <sub>2</sub> -oxidation over a ‘Radical-Recombination Wall’.....	68
4.4.2	Size effects in a RR-microchannel reactor.....	71
4.5	ADIABATIC CALCULATION: INERT & Pt WALLS.....	89
4.5.1	Influence of reactor dimension on quenching – Pt.....	93
4.6	RELEVANT REACTION SYSTEMS.....	98
4.6.1	CO Oxidation: Isothermal Calculations.....	98
4.6.2	Interaction between homogeneous and heterogeneous reactions.....	100
4.6.3	Microchannel size effects: CO oxidation.....	104
4.6.4	Microchannel size effects in RR wall: CO-H <sub>2</sub> oxidation.....	106
4.6.5	NO <sub>x</sub> formation.....	109
5.0	SUMMARY.....	116
6.0	OUTLOOK.....	120
6.1	POSSIBLE APPLICATION TO OTHER REACTIONS.....	120
6.2	DESIGN & FABRICATION OF A MICROREACTOR.....	122
APPENDIX A.....		126
MODEL DESCRIPTION & DETAILED KINETICS.....		126
APPENDIX B.....		141
VALIDATION OF BOUNDARY LAYER MODEL & MEAN FREE PATH CALCULATION.....		141

APPENDIX C .....	143
CALCULATION OF PRESSURE DROP IN MICROCHANNEL .....	143
APPENDIX D.....	146
INFLUENCE OF VELOCITY DISTRIBUTION ON OVERALL IGNITION.....	146
APPENDIX E .....	149
VARIATION OF PLATINUM SURFACE KINETICS ON IGNITION .....	149
APPENDIX F.....	154
VALIDATION OF Pd SURFACE KINETICS FOR H <sub>2</sub> O <sub>2</sub> PRODUCTION.....	154
BIBLIOGRAPHY .....	159

## LIST OF TABLES

<b>Table 1:</b> Calculated apparent activation energy from the mathematical expression mentioned above for diameters from 250 to 100 $\mu\text{m}$ in case of RR wall. ....	82
<b>Table 2:</b> Governing equations of the boundary layer model.....	127
<b>Table 3:</b> Gas-phase kinetics of $\text{H}_2$ – air mixture .....	128
<b>Table 4:</b> Surface reaction steps and rate parameters by Andrae et.al [9]. ....	130
<b>Table 5:</b> Surface reaction steps and rate parameters by Park et.al [9]. ....	131
<b>Table 6:</b> Surface reaction steps and rate parameters by Aghalayam et.al [17] .....	132
<b>Table 7:</b> Detailed surface kinetics of $\text{H}_2$ -oxidation on Pd surface [67].....	133
<b>Table 8:</b> Surface reaction steps and rate parameters by Andrae et.al [63].....	134
<b>Table 9:</b> Modified surface kinetics of Radical Recombination wall.....	135
<b>Table 10:</b> Individual radical kinetics on Radical Recombination surface.....	137
<b>Table 11:</b> The gas phase CO oxidation mechanism from Yetter et.al [42].....	138
<b>Table 12:</b> The Catalytic CO oxidation mechanism on clean polycrystalline platinum ( $\theta_{\text{PT}}=1$ )	140
<b>Table 13:</b> The Catalytic $\text{NH}_3$ oxidation mechanism on clean polycrystalline platinum [73] ....	140
<b>Table 14:</b> Pressure drop calculation in microreactor for two limiting cases.....	144
<b>Table 15:</b> Rate constants calculation of $\text{H}_2\text{O}_2$ formation from H.Sellers surface kinetics.....	155
<b>Table 16:</b> Energetics of Pd surface under low surface coverage.....	156
<b>Table 17:</b> Surface coverage of main species on Pd surface at 713K with modified kinetics.....	158

## LIST OF FIGURES

- Figure 1:** A Schematic overview of the microreactor used in the simulation..... 14
- Figure 2:** Velocity (left) and temperature (right) profile versus reactor length (z) and radius (r) of the microreactor with 1mm diameter and inert wall at 1173K. .... 21
- Figure 3:** Concentration contour plots of H<sub>2</sub> (left), O<sub>2</sub> (middle) and H<sub>2</sub>O (right) versus reactor length (z) and radial distance (r) at 1173K with 1mm diameter. .... 22
- Figure 4:** Ignition distance vs. reaction temperature in a microreactor with 1mm diameter and inert wall. .... 24
- Figure 5:** Ignition distance vs. reaction temperature for a reactor with 1mm diameter and inert wall (filled circles), Pt-coated catalytic wall (filled squares) and a catalytic wall without gas-phase reactions (open squares)..... 26
- Figure 6:** Contour plot of O<sub>2</sub> concentration using an inert wall (left) and contour plot of O<sub>2</sub> concentration with Pt wall (right) versus reactor length (z) and radius of the reactor (r). The reaction temperature is maintained at 1113K. .... 28
- Figure 7:** Ignition distance versus reaction temperature for a reactor with catalytic Pt-wall varying channel diameters. .... 30
- Figure 8:** Contour plot of O<sub>2</sub> concentration (top row) and H radical concentration (bottom row) using Pt wall with 1 mm (left), 500 μm (middle) and 300 μm (right) microreactor diameters as a function of axial (z) and radial (r) distances keeping temperature constant at 1113K. . 32
- Figure 9:** H<sub>2</sub> concentration (mol fraction) versus reactor length (cm) in a microreactor with 1mm diameter (left) and 300 μm diameter (right). At inlet stoichiometric feed mixture of H<sub>2</sub>-air is fed in the microchannel reactor with 9 m/s velocity at ambient pressure..... 35
- Figure 10:** Concentration contour plots of O<sub>2</sub> consumption (left column) and H radical formation (right column) for Pt wall with 300 μm diameter varying catalyst loading at 1113K..... 38
- Figure 11:** Ignition distance versus reaction temperature at the centerline of a 300μm reactor diameter at 1bar (left), 5bar (middle) and 10bar (right). Filled symbols represent both homogeneous and heterogeneous reactions while open symbols represent the purely homogeneous case. .... 40

- Figure 12:** Ignition distance versus reaction temperature at the centerline of a 300  $\mu\text{m}$  reactor diameter at 0.5 bar (reversed triangles), 1 bar (circles) and 5 0bar (squares), 10 bar (triangles) and 20 bar (diamonds) solely with Pt wall. .... 41
- Figure 13:** Contour plot of  $\text{O}_2$  concentration in a 300  $\mu\text{m}$  microreactor using Pt wall at 1 bar (left), 5 bar (middle) and 10 bar (right) reaction pressure. The reaction temperature is maintained at 1253 K. The Pt catalyst is deposited at the top wall ( $r = 0.015$  cm), while  $r = 0$  cm denotes the center line of the reactor. Feed gas mixture flows from left to right. .... 42
- Figure 14:** Contour plot of  $\text{O}_2$  concentration in a 300  $\mu\text{m}$  microreactor using Pt wall at 1 bar (left), 5 bar (middle) and 10 bar (right) reaction pressure. The reaction temperature is maintained at 1113 K. The Pt catalyst is deposited at the top wall ( $r = 0.015$  cm), while  $r = 0$  cm denotes the center line of the reactor. Feed gas mixture flows from left to right. .... 44
- Figure 15:** Reaction path analysis of Pt surface kinetics where the sensitivity of individual net reaction is shown in the bar graph at right corresponding to the reaction mentioned at the left. .... 48
- Figure 16:** Net surface reaction rate ( $r_s$ ) of 9 reversible reactions on Pt surface at 1113K as a function of reactor length ( $z$ ) of 2.5 cm in primary axis and overall conversion across the length in secondary axis to identify the dominant influence of true surface reaction. Reactions corresponding to the surface rate consequently are written above each rate denoting line..... 49
- Figure 17:** 3D plot of critical ignition distance ( $X_c$ ) versus reaction pressure ( $P$ ) ranging from 1 bar to 20 bar and reactor diameter ( $D$ ) varying from 50  $\mu\text{m}$  to 1000  $\mu\text{m}$  ( $y$  axis) for  $\text{H}_2$  oxidation in a Pt coated reaction channel. .... 51
- Figure 18:** Critical diameter in mm ( $y$  axis) derived from the mathematical expression as a function of reaction pressure in bar ( $x$  axis) shows the exponential dependency..... 52
- Figure 19:** In left graph ignition distance versus reaction temperature at the centerline of a 300  $\mu\text{m}$  reactor diameter at 1 bar with  $\phi = 2.0$  (open squares),  $\phi = 1.0$  (filled circles) and  $\phi = 0.5$  (open triangles) with full homogeneous-heterogeneous kinetics. In right, ignition distance versus temperature with  $\phi = 2.0$  varying pressure from 1 bar to 10 bar. .... 54
- Figure 20:** Ignition distance versus temperature using  $\text{H}_2$ -air and  $\text{H}_2$ -pure  $\text{O}_2$  stoichiometric feed mixture in a 300 $\mu\text{m}$  microreactor at 1 bar. Filled squares with dotted line represent ignition distance using  $\text{H}_2$ -air mixture and filled circles with solid line shows ignition distance using  $\text{H}_2$ -pure  $\text{O}_2$  mixture. .... 56
- Figure 21:** O coverage (left) and free surface coverage (right) on Pt surface versus reactor length ( $z$ ) using  $\text{H}_2$ - $\text{O}_2$  and  $\text{H}_2$ - air as feed mixture in a reactor with 300 micrometer diameter at 1113K..... 57

<b>Figure 22:</b> Concentration contour plots of O <sub>2</sub> (top row) and H radical (bottom row) versus height (h) and reactor length (z) for 1 mm and 300 μm reactor diameters with planar geometry. Stoichiometric H <sub>2</sub> -air mixture is fed at inlet with 9 m/s velocity at 1 bar for isothermal operation. Temperature is set to 1113K.....	59
<b>Figure 23:</b> Ignition distance vs. reaction temperature for a microreactor with 1 mm diameter and inert wall (circles), Pd coated (diamond) and Pt coated catalytic wall (squares). .....	62
<b>Figure 24:</b> Contour plots of O <sub>2</sub> concentration (left column) and H concentration (right column) with 1mm diameter at 1113K using inert (top), Pt wall (middle) and Pd wall (bottom).....	63
<b>Figure 25:</b> Ignition distance versus reaction temperature for a reactor with Pd coated wall and varying channel diameter from 1 mm to 100 μm. ....	64
<b>Figure 26:</b> Contour plot of O <sub>2</sub> concentration (top row) and H radical concentration (bottom row) using Pd wall with 1 mm (left), 500 μm (middle) and 300 μm (right) microreactor diameters keeping temperature constant at 1113K.....	65
<b>Figure 27:</b> 3D plot of critical ignition distance (z axis) versus reaction pressure (x axis) ranging from 1 bar to 20 bar and reactor diameter varying from 1000 μm to 50 μm (y axis). ....	67
<b>Figure 28:</b> Ignition distance vs. reaction temperature for a microreactor with 1 mm diameter and a radical recombination wall (triangles), inert wall (circles) and Pt coated catalytic wall (squares).....	69
<b>Figure 29:</b> Contour plots of O <sub>2</sub> concentration (top row) and H concentration (bottom row) with 1mm diameter at 1113K using inert (left), RR wall (middle) and Pt wall (right). ....	70
<b>Figure 30:</b> Ignition distance versus reaction temperature for a reactor with a "radical recombination" wall varying channel diameters from 1 mm to 100 μm. Stoichiometric H <sub>2</sub> -air mixture is fed in the microreactor with 9 m/s velocity and at 1 bar pressure.....	72
<b>Figure 31:</b> Free surface coverage ( $\Theta_{\text{free}}$ ) versus reactor length (z) with 1mm and 250μm reactor diameters at 1513K using RR wall. ....	73
<b>Figure 32:</b> Ignition distance (circles, solid line) on the left axis and temperature (diamonds, dashed line) on the right axis at quenching point are plotted vs. reactor diameter in case of RR wall. ....	74
<b>Figure 33:</b> Rate of O <sub>2</sub> consumption (circles) and formation (triangles) with 1mm (solid line) and 250 μm (dashed line) diameters at 1513 K versus reactor length (z). ....	76
<b>Figure 34:</b> H <sub>2</sub> concentration (C <sub>H2</sub> ) versus reactor length (z) is plotted with 1mm diameter using RR wall. ....	77

- Figure 35:**  $H_2$  concentration ( $C_{H_2}$ ) versus reactor length ( $z$ ) is plotted using 250  $\mu\text{m}$  diameter with 250 mm (left) and 3 mm axial distances (right) using RR wall..... 78
- Figure 36:** Temperatures at transition point (seen with lower diameters) and at quenching point with different reactor diameters with RR wall for a stoichiometric  $H_2$ -air mixture at 1 bar. 80
- Figure 37:**  $H_2$  concentration profile along reactor length for 250  $\mu\text{m}$  diameter with full RR wall kinetics (solid line), kinetics only with H radical containing steps (dashed), kinetics only with OH radical containing steps (dot dot dashed), kinetics only with  $H_2O_2$  radical containing steps (dot dashed) and kinetics only with O radical involving steps (dotted). Temperature is kept constant at 1513K. .... 84
- Figure 38:** Rate of formation (left) and consumption (right) of surface species H, OH, and O at 1513K with 300  $\mu\text{m}$  (top row) and 250  $\mu\text{m}$  diameters in case of RR wall..... 86
- Figure 39:** Reduction in overall conversion (%) and increase in quenching temperature versus reactor diameter (mm) using RR wall at 1513K..... 88
- Figure 40:** Concentration (in mol fraction) of major reactant, intermediate and product species for  $H_2$  oxidation versus axial reactor length (cm) for adiabatic case (left graph) and for isothermal operation (right graph) where temperature profile is plotted in secondary axis. 90
- Figure 41:** Ignition distance versus inlet reaction temperature ( $T_{in}$ ) for an adiabatic microreactor with 1 mm diameter and inert wall (open circles) and Pt-coated catalytic wall (filled circles)..... 92
- Figure 42:** Ignition distance versus reaction temperature for an adiabatic reactor with catalytic Pt-wall varying channel diameter from 1 mm to 5  $\mu\text{m}$  (left) and comparing adiabatic (open symbols) and isothermal (filled symbols) operation (right) for 1mm (squares), 500  $\mu\text{m}$  (circles) and 300  $\mu\text{m}$  (triangles)..... 93
- Figure 43:** Ignition distance versus temperature of a microreactor with 1mm diameter for adiabatic operation varying inlet temperature from 300 to 1200K (squares) and for isothermal operation with inlet temperature added with adiabatic temperature rise for  $H_2$  oxidation system. .... 95
- Figure 44:** Concentration contour plots of  $O_2$  (top row), H radical (middle row) and temperature profile (bottom row) along axial and radial direction at 993K with 1mm (left column), 300  $\mu\text{m}$  (middle column) and 5  $\mu\text{m}$  (right column) diameters..... 97
- Figure 45:** Ignition distance vs. reaction temperature in a microreactor for CO oxidation with 1mm diameter and inert wall where left plot is with Yetter et.al kinetics and right plot is with GRI mechanism (Appendix A)..... 101

<b>Figure 46:</b> Ignition distance vs. reaction temperature in a microreactor for CO oxidation with 1mm diameter and inert wall in case of CO with pure O <sub>2</sub> (left graph) and CO – air mixture with 1.5% OH addition (right plot).....	102
<b>Figure 47:</b> Homogeneous – heterogeneous interaction of CO oxidation in terms of ignition distance versus reaction temperature, (I) coupled case (circles) and only heterogeneous ignition (squares); (II) inert wall (open circles), inert wall with OH addition (filled circles), coupled case (squares); (III) inert wall (open circles), coupled case (filled circles), coupled case with OH addition (squares).....	103
<b>Figure 48:</b> Ignition distance versus reaction temperature for 1.5% OH added CO-air reaction mixture with diameters 1mm (filled squares), 500 μm (filled circles) and 300 μm (filled triangles).....	105
<b>Figure 49:</b> Ignition distance versus reaction temperature in case of CO-air oxidation with 300 μm diameter (dashed line, open squares), CO-air oxidation with 1.5% OH addition (solid line, open circles) and in case of H <sub>2</sub> oxidation with 300 μm (dotted line, reverse triangle).....	108
<b>Figure 50:</b> Concentration of nitric oxide (C <sub>NO</sub> ) versus reactor length (z) varying with reaction temperature from 1803K to 2273K in case of purely homogeneous case (left plot) and for the coupled case (right plot). H <sub>2</sub> -air mixture with nitrogenous species is fed in microreactor with 1 mm diameter and at 1 bar pressure while inlet velocity is set to 9 m/s.....	111
<b>Figure 51:</b> Concentration of NO versus reactor length (z) with 1 mm, 500 μm and 300 μm reactor diameters at 600K temperature. H <sub>2</sub> -air is fed in a Pt-coated microreactor at the same inlet conditions.....	113
<b>Figure 52:</b> Concentration of NO (C <sub>NO</sub> ) along the reactor length (z) at 1803K with H <sub>2</sub> /air equivalence ratio of 0.1 (dashed line), 1.0 (solid line) and 2.0 (dotted line) with 1 mm (left graph) and 500 μm (right graph) diameters. This is for purely homogeneous ignition.....	114
<b>Figure 53:</b> 3-dimensional microreactor design in AutoCAD program.....	122
<b>Figure 54:</b> Imported view of the new microreactor in Fluent software.....	125
<b>Figure 55:</b> Mathematical fit of ignition distance vs. pressure at 1758K (left) and at 973K (right).....	145
<b>Figure 56:</b> Velocity distribution in a microreactor with 1 mm diameter and inert wall for fully developed flow (left) and the flow having a flat entrance with gradually developing parabolic velocity (right) versus axial and radial length of the reactor at 1173K.....	146

**Figure 57:** Ignition distance (y axis) versus reaction temperature(x axis) for a reactor with catalytic Pt-wall varying channel diameters with a constant velocity at the reactor entrance and subsequent parabolic velocity profile for stoichiometric H<sub>2</sub> oxidation..... 147

**Figure 58:** Ignition distance vs. temperature using Andrae et.al (filled diamonds and solid lines), Park et.al (filled circles and dotted lines) and Aghalayam et.al (filled triangles and dashed lines) surface kinetics. Kinetics by Park et.al is based on a clean Pt surface (full case:  $\Theta_{\text{H}}+\Theta_{\text{O}}$ ). The simulation is performed using 300 $\mu\text{m}$  reactor diameter..... 150

**Figure 59:** Ignition distance vs. temperature using Park et.al where surface mechanism is based on a surface having  $\Theta_{\text{O}}=1$ (filled diamonds and dotted lines), on a clean surface having  $\Theta_{\text{free}}=1$ (filled squares and solid lines) and on a surface having  $\Theta_{\text{O}}+\Theta_{\text{H}}$ , full case (filled circles and dotted lines). The simulation is performed for a 300 $\mu\text{m}$  reactor diameter. .... 152

## NOMENCLATURE

Symbol	Description	CGS Units
T	Temperature	K
u	Axial velocity of fluid mixture (x direction)	cm/s
x	Spatial coordinate along principal flow	cm
$\xi$	Normalized stream function	none
M	Mass in at inlet of the reactor	g
$M_l$	Mass loss at the exit	g
p	Pressure	dynes/cm <sup>2</sup>
$\mu$	Mixture viscosity	g/cm.s
y	Cross stream coordinate	cm
$\alpha$	Coordinate index: 1 for radial, 0 for planar	none
g	Acceleration due to gravity	cm/sec <sup>2</sup>
$\rho_i$	Mass density at the reactor inlet	g/cm <sup>3</sup>
$\rho$	Mass density of a gas mixture	g/cm <sup>3</sup>
$Y_k$	Mass fraction of the k <sup>th</sup> species	none
$\dot{\omega}_k$	Chemical production rate of k <sup>th</sup> species due to gas phase reactions	mole/(cm <sup>3</sup> .sec)
$W_k$	Molecular weight of the k <sup>th</sup> species	g/mole
$V_{k,y}$	Diffusion velocity of kth species in y direction	cm/s
$c_p$	Specific heat at constant pressure of gas	ergs/g.K

$c_{pk}$	Specific heat at constant P of $k^{\text{th}}$ species	ergs/g.K
$\lambda$	Thermal conductivity of the gas mixture	erg/cm.s.K
$\bar{W}$	Mean molecular weight of a mixture	g/mole
s	Sticking coefficient	none
$\Theta_k$	Surface coverage of $k^{\text{th}}$ species	none

## ACKNOWLEDGEMENTS

I would foremost like to thank my advisor Dr. Götz Vesper for his constant support, the important detailed discussions about my work and his genial and delicate way of leading the research group. It has been an absolute pleasure working in his team during the course of entire PhD. I cordially thank all of my committee members Dr. Wender, Dr. Enick and Dr. Gallaher for providing me with many helpful insights on my work.

Furthermore, I would like to thank my lab mates Dirk Neumann, Mark Kirchoff, Uli Specht, Klaus Mehler, Tengfei Liu, Tom Sanders, Vanessa Gepar, Anthony Mitri and Craig Anderson for the fun we had in the squad which made my work a lot more pleasurable.

In addition, I would like to thank the ‘Max-Planck-Institute für Kohlenforschung’, Germany, where I started my PhD, and the theoretical chemistry group in there under the supervision of Dr. Walter Thiele for their help in learning me Gaussian ab-initio method for calculating transport properties of larger molecules.

Finally, I would like to thank the faculty, staff and students (namely Ade, Yannick, Sevgi, Felipe, John, Jeff, Dhruv, Abhishek and a long list) of the Chemical Engineering Department at the University of Pittsburgh for their friendly support that made my stay in Pittsburgh a lot more enjoyable.

Furthermore, I do acknowledge the support from the Mechanical Engineering Department for the MEMS design regarding the fabrication of new microreactor.

Most importantly I am entirely indebted to my parents Mr. Swadhin Kr. Chattopadhyay, Professor of Chemistry in India, and Mrs. Laxmishree Chattopadhyay for their constant enthusiasm, inspiration and loving support since the beginning of my life. I am also thankful to

my in-laws Mr. & Mrs. Goswami for their moral support in pursuing my PhD indeed. To my husband, Subhendu, I am endlessly grateful to you for your entire warm support, encouragement and indefinite sacrifices which boosted me up to finally finish this dissertation work and I thank you very much.

## 1.0 INTRODUCTION

Ignition, i.e. the transition from an unreactive to a reactive state, is a necessary prerequisite for any chemical reaction. However, the ignition of undesired reactions is also the reason for selectivity losses in sequential as well as parallel reaction networks and can lead to safety hazards such as run-away and explosive behavior in industrial reactors [1]. A well-controlled and safe chemical process therefore requires a good understanding of the reaction mechanism underlying the specific process as well the main influences of operating parameters on the ignition behavior. Therefore, many studies have been dedicated to the understanding of the ignition of chemical reactions, both for homogeneous (i.e. non-catalytic gas-phase) as well as catalytic processes[1, 4]. Since the addition of a catalyst opens up a new reaction pathway with a different (typically lower) activation energy and thus different ignition behavior, catalytic processes constitute a particularly interesting case, both from an applied as well as a scientific point. In most chemical processes, the ignition of only one of the low-temperature catalytic reaction is desired in order to avoid excessive temperatures, unwanted side reactions, and, particularly, the occurrence of open flames or explosions.

An important example for such processes is high temperature catalysis. High temperature catalytic reactions are being intensely studied since many decades due to their industrial importance, such as in pyrolysis, total oxidation (i.e. combustion) for energy production and partial oxidation of hydrocarbons for the production of numerous petrochemical intermediates [5]. The reactions are characterized by extreme reaction temperatures ( $T > 1000^{\circ}\text{C}$ ) where

homogeneous reactions can occur in parallel to catalytic reactions. This occurrence of homogeneous reactions is typically undesired, since it significantly complicates the fundamental understanding of reaction mechanisms and often poses a safety hazard due to potentially explosive behavior [3]. Hence, care must be taken to control or avoid homogeneous gas-phase reactions, in order to avoid selectivity losses during partial oxidation, and uncontrolled process temperatures, open flames and explosions in both total and partial oxidation processes [2].

In these days, scientific research in the energy sector is moving towards the production of H<sub>2</sub> as an alternative source of clean and efficient fuel via various “Hydrogen Solution” projects [6]. As a consequence, during production and transportation of H<sub>2</sub> in large scale, a major issue arises concerning “safety”. Each of the drawbacks faced by hydrogen economy, i.e. production, storage, safety, fuel cells, etc. is thorny enough on its own. In particular, resolving this “safety” issue, hydrogen oxidation reactions system needs to be carried out in a safe way.

Catalytic oxidation of hydrogen is an important, yet simple, sub-set of hydrocarbon oxidation, i.e. high temperature catalytic reactions. The reaction has been studied for many years and is therefore well understood [7-10]. Beyond its importance as a subset of hydrocarbon oxidations, it is also an important combustion reaction in itself which is used in rocket propulsion and more recently as a key reaction in fuel cells. The reaction is characterized by particularly wide flammability limits (about 3-75 vol% H<sub>2</sub> in air) and very high flame velocities, i.e. strong explosions [1]. Its strong exothermicity ( $\Delta H \approx -240$  kJ/mol) makes it a possible energy (heat) source, but the danger of strong explosions restricts its use for practical applications to feed mixtures below the lower flammability limits.

H<sub>2</sub> oxidation proceeds via a radical-chain branching mechanism like all hydrocarbon oxidations (gas phase-homogeneous). Surfaces are known to capture radicals and hence sufficient surface

area could help to suppress homogeneous reactions. Large surface-to-volume ratios are achievable in miniaturized structures, such as in microfabricated devices with which elimination of undesired homogeneous reactions can be probable.

We have recently been able to show that the explosion hazard in H<sub>2</sub> oxidation can be strongly reduced through the use of micromachined catalytic reactors [2, 3, 11]. Such “microreactors”, defined here as chemical reactors with characteristic dimensions in the sub-millimeter range, show a number of advantages over conventional “macroscopic” reactors [12]. Among the advantages of microreactors for chemical processes are their small reactant volumes, short pathways for heat and mass transport, and very large surface-to-volume ratios. On top of these, their small overall dimensions make them ideal for applications where space requirements are critical, such as in mobile devices.

It is the aim of this study to investigate the use of catalytic microreactors for potentially explosive reactions via detailed numerical simulations. The objective of these simulation studies is to evaluate the intricate interplay between homogeneous and heterogeneous reaction pathways, investigate how and under what conditions reactor dimensions can lead to a quenching of explosions, test the influence of different wall materials and ultimately to test the applicability of this approach to different reaction systems.

After a brief overview of current technologies in the field of microchemical systems and especially the importance of ignition studies in high temperature catalysis, chapter 2 discusses the role of numerical simulations in these studies. In particular, it will be discussed how simulations help to gain a better and precise understanding of experimental observations.

In this study, simulations are based on a two-dimensional boundary layer model using the Creslaf module of the commercially available software CHEMKIN 3.6. Detailed descriptions of

homogeneous and heterogeneous reaction pathways were included through elementary-step kinetics of surface and gas-phase reactions inside the microreaction channel. Details of the model and numerics are presented in chapter 3.

Chapter 4 then presents the results from the simulation studies. Four different wall materials were studied: a completely inert wall as a reference case, catalytically active noble metal surfaces (Pt, Pd) and a generic ‘radical recombination’ surface (RR), representing non-catalytic radical-scavenging materials such as quartz glass. While the RR wall showed an ignition-inhibiting effect, suppressing all reactions at sufficiently small channel diameters, the catalytic walls showed a transition from an ignition-promoting effect at lower reaction temperatures to an ignition-inhibiting effect at high reaction temperatures due to interactions between homogeneous and catalytic reaction pathways [13]. In qualitative agreement with previous experiments, a complete quenching of homogeneous reactions is also observed for any temperature and at atmospheric pressure for reactor diameters below 285  $\mu\text{m}$ . Since increasing pressure can lead to a break-down of this quenching, the effect of reaction pressure on overall ignition behaviour of  $\text{H}_2$  oxidation in catalytic microreactors is studied next. All simulations are performed in an isothermal microreactor [14] to decouple the kinetic effect from thermal effect. In addition to that, it is of interest to investigate non-isothermal operation of explosive reactions in microreactors as temperature strongly influences ignition behaviour. Therefore, adiabatic simulations were also conducted to study the influence of non-isothermal conditions on the ignition behaviour and those are illustrated in chapter 4.

Though the present work is quantitatively valid particularly for hydrogen oxidation reaction system on catalytic and non-catalytic materials but qualitatively a similar behaviour is expected to be observed for other similar (industrially relevant) reactions systems such as in particular CO

oxidation, CO-air/H<sub>2</sub>-air oxidation, NO<sub>x</sub> formation in combustion. Those systems are studied and are discussed in the last section of the same chapter.

Overall, our study indicates that microreactors can be intrinsically safe reactors for the study of high-temperature catalytic reactions, and hold the potential to be developed into highly sensitive tools for the study of the homogeneous-heterogeneous interactions.

Chapter 6 concludes this work with a summary and an extended outlook of this work is in chapter 7. We are currently designing a new microreactor to verify our numerical results in future experimental studies. The design and fabrication are briefly introduced in chapter 7.

## **2.0 FUNDAMENTALS**

Microfabrication techniques have led to dramatic advancements in the electronics industry since the past four decades. More recently these techniques have also found applications in the chemical and biological field. New horizons open up in the application to the reaction engineering toolbox. The real value of this chemical process miniaturization effort lies in researches in exploring new reaction pathways, concerning safety and finding economical and environmentally benign solutions to chemical manufacturing. Ignition studies in micromachined reactors add new perspectives in terms of safe reactor operation and those are being evaluated with numerical approach as in [13].

### **2.1 MICROCHEMICAL SYSTEMS**

Microchemical systems, microreaction technology [15], “lab-on-a-chip” [16], “plant-on-a-chip” have gone from buzzwords to major research paradigms in the field of engineering in the last decade. Microfabrication techniques [17] have originally developed from microelectronics applications. The application of such systems promise to offer compactness, low weight, low cost, high efficiency, mobility and performance characteristics that are significantly different from full-scale engineering processes. Furthermore, such micromachined systems can be mass

produced and replicated in parallel after standardizing and thereby partially offset the economies of scale which are realized by traditional large scale processes.

Microchemical systems or “microreactors” used in such studies are “chip-scale” microfabricated reactors comprised of channels etched in the thin oxide layer coated silicon wafer using silicon bulk micromachining techniques involving photolithography and KOH etching techniques [18-20]. Glass or different metals can be used as substrate materials besides silicon, but due to the availability of well-developed and reliable photolithography and etching techniques in the microelectronics industry, silicon is typically favored as the substrate for micromachining.

Catalyst deposition is a particularly challenging part in developing those catalytic micromachined reactors. In one of the earliest studies with catalytic microreactor where channel walls were catalytically coated with a platinum catalyst, the authors reported degradation of the catalyst problem above 700°C [21]. That is due to thermal expansion mismatch between Si substrate and Pt thin film. Such problems can be avoided for example in the set-up of Veser et.al [3] by using Pt catalyst as a thin wire in the channel.

In a recent study, a wall coated silicon microchannel reactor is successfully fabricated for preferential oxidation of CO in excess of H<sub>2</sub> and the results were compared to a tubular packed bed micro-reactor [22]. The authors have successfully addressed the scale-up issue by stacking microreactors with glass-frit bonding and a double layer stack microreactor is fabricated which holds all the properties of microreactor. That stacking-bonding scale-up method also been used to fabricate a cross-flow heat-exchanger using the same design which showed numerous advantages in terms of heat integration over the conventional packed-bed reactors.

The large body of work on heterogeneously catalyzed gas phase reactions in micro-structured reactors have been reviewed by Kolb and Hessel of IMM in Germany [23]. They defined the

achievement of proper microfabrication techniques as Phase I which represents the time period since 1990-2000. The comprehensive characterization of micromachined devices mainly involving experts from heterogeneous catalysis is defined as Phase II. This covers a period starting from 1998 up to now. Since the last two years Phase III marks the commercial fabrication of microreactors.

Within the last decade various groups have successfully developed different microreactors for chemical processing applications such as phosgene synthesis [24], multiphase processing [25], chemical detection [26] and H<sub>2</sub> production for fuel cell applications [27]. A brief summary on the applications of such micromachined reactors is given by Wan et.al [28]. Different fabrication techniques and intricacy of catalyst deposition methods in microchannels is discussed in detail. These microchemical systems, still in its infancy, have the right potential to change the chemical engineering landscape.

## **2.2 IGNITION STUDIES**

Ignition, when a sufficient amount of reactive radicals are produced to start off the reaction by the free radical chain reactions, is the prerequisite of all chemical reactions in gas phase. After ignition, reactions proceed either catalytically or non-catalytically as a wave propagating from a localized source of ignition throughout the whole volume. Many studies have been conducted on ignition of different high temperature oxidation reactions since the 1950s [1, 9, 29-31]. In these gaseous fuel-oxidant systems, explosion limits are specified in terms of kinetic and diffusion parameters (which determine the rate of chain branching and chain breaking), temperature,

pressure, composition and especially the dimension of reaction vessel and the material of the inner vessel surface.

These explosion limits in absence of a catalytic material are investigated in detail and well illustrated in [1] for H<sub>2</sub> oxidation reaction system. H<sub>2</sub> oxidation is a typical example in the category of highly exothermic reactions which has several important applications in high temperature catalysis as an important subset reaction in the oxidation of all fossil fuels. In particular, the behavior of hydrogen-oxygen system was challenging to understand: the explosion behavior of this system is quite complex due to its wide range of flammability limits and clearly inconsistent with a set of simple global reactions which is generally unable to address the critical reaction steps influencing explosion. Homogeneous chemistry of various light fuels, i.e. hydrogen, methane is relatively known since 1980's, but the relative importance between homogeneous and heterogeneous chemistries of those fuels is still under rigorous research.

Detailed ignition study was made in the confined boundary layer with laser induced fluorescence (LIF) for OH and O radicals measurements [32, 33]. The gas-phase ignition of ethane-air in a boundary layer at ambient conditions over catalytic and non-catalytic surface was investigated. The authors measured the production rate of OH and O radicals near the wall in catalytically stabilized thermal (CST) combustor at the time of ignition. However, their boundary layer ignition experiment was unable to measure stable products for high temperature surface oxidation and also the intermediates prior to ignition. The experiment was set to in simulating the entrance region of a catalytically stabilized thermal (CST) combustor [34].

In addition to the mentioned LIF technique, an array of other different experimental techniques such as temperature programmed reaction (TPR) [35], molecular beam relaxation (MBRS) [36],

catalytic ignition temperatures [37], catalytic autotherms [38] have been employed in the context of H<sub>2</sub> oxidation reaction system.

The controlled oxidation of hydrogen in a microstructured stainless steel reactor/heat exchanger on a Pt impregnated alumina catalyst was studied by Schubert et.al [39] where they have observed hazardous mixture can be safely operated and a dramatic improvement of catalyst activity also was illustrated. On the contrary, they also described the difficulties faced in depositing catalyst on the wall which needs to be looked into in detail.

Other relevant reactions systems, such as, high temperature oxidation of moist CO air mixtures have been conducted in shock tubes [40] and stirred reactors [41]. Gas phase ignition of carbon monoxide/hydrogen/oxygen system has been reviewed in early 90's which has started since 30's by several researchers [42, 43] and surface ignition on Pt surface has been studied in ultra-high vacuum chamber and extrapolated to atmospheric pressure by Kasemo et.al [44]. Steady state as well as transient kinetics of CO oxidation on Pt wire was examined up to 1500K by Schmidt et.al [45]. Kasemo et.al [46] has shown in the experiment of CO oxidation over Pt (100) and also in a simulation with a three step kinetic model that a kinetic phase transition is observed from a CO covered surface to a O covered regime after ignition. In various works reaction rates of catalytic CO oxidation over Pt are studied as coverage dependent [47, 48] and global kinetic model were validated against experimental results [48, 49].

Ignition and extinction of homogeneous-heterogeneous combustion was studied on Pt catalyst for methane and propane oxidation [50, 51].

In mapping out the heat flux at cold wall as a function of wall temperature for hydrocarbon (methane, ethylene and propane)-air systems recent experiments and theoretical work have been performed [52, 53]. Comparing experimental and theoretical results failed to produce satisfactory

results and authors suggested that the coupling of detailed gas phase chemistry and wall is necessary to explain experiments by reactor simulations. This exemplifies the importance of numerical simulation as a crucial tool in understanding the experimental observations.

## 2.3 REACTOR SIMULATIONS

Detailed reactor simulations, in conjunction with experiments, play a critical role in microreactor technologies by providing analysis of specific microchemical reactor systems, design of new systems [54] and evaluation of potential performance advantages relative to conventional macroscale reactors. Simulations thus serve not only as a design tool, but also as a means to interpret experimental data [54, 55]. Such numerical simulations are particularly necessary for high temperature studies, which are exceedingly difficult to study experimentally due to the danger of explosions as well as very fast and highly complex kinetics. High temperature catalytic combustion of hydrocarbons has been extensively numerically modeled in different studies [56-58].

The role of radical wall quenching as a function of strain rate for H<sub>2</sub> oxidation reaction has been studied in numerical simulations by Aghalayam et al. for a conventional (macroscopic) reactor [59]. They showed that quenching of radicals retards the system at ignition due solely to kinetic effects. The role of quenching of various radicals in ignition and extinction at different strain rates was also investigated. Their simulations revealed that, at lower temperatures, surface chemistry and diffusion play a minor role. However, at higher wall temperatures, gas diffusion, adsorption and surface recombination of radicals are important for accurate prediction of heat flux at the wall. Park et.al [60] predicted coverage-dependent reaction parameters (activation

energy) of H<sub>2</sub> oxidation on platinum surface applying unity bond index – quadratic exponential potential (UBI-QEP) method pioneered by Shustorovich et.al [61]. In addition to that in the same research team Aghalayam et.al [62] optimized the frequency factors to stabilize the surface kinetics for H<sub>2</sub> oxidation reaction system on Pt surface.

Johan et al. studied the importance of chemical (kinetic) versus thermal wall effects of laminar hydrogen flames for a similar reactor configuration [63]. The importance of chemical wall effects compared to thermal wall effects caused by heat transfer to a cold wall was investigated by using different combustion systems at atmospheric pressure. They varied carrier gas from N<sub>2</sub> to He to see the effect of the enhanced mass and heat transfer rates on the surface due to higher diffusivity and conductivity of He than N<sub>2</sub>. For leaner mixtures, however, thermal and velocity boundary layers result in stronger wall effects than surface chemistry.

Finally, Vlachos [64] studied the influence of “reactor size” on the induction period during homogeneous H<sub>2</sub>-oxidation with an emphasis on finite size effects and fluctuations on the ignition of the gas phase reaction. He could show that finite size effects only become important for reactor volumes below 10<sup>-2</sup> μm<sup>3</sup>, i.e. well below the volumes relevant for microfabrication and thus outside the realm of this study.

Our group has previously shown experimentally that it is possible to completely suppress explosive reaction behavior in a microreactor [2, 3, 11]. The main two mechanisms which lead to homogeneous flames are kinetic and thermal explosions. Experimentally, these mechanisms are usually very difficult to distinguish since typical radical chain reactions are sufficiently exothermic to lead to a rapid increase in reaction temperature once the homogeneous reactions ignite. This increase in the reaction temperature is then accompanied by a strong increase in radical concentrations. Therefore, to separate kinetic and thermal effect and to gain a more

thorough understanding of the reaction mechanism of hydrogen oxidation in a microreactor, detailed numerical simulations are needed. These simulations are the topic of the present thesis.

## 3.0 NUMERICAL SIMULATION

### 3.1 REACTOR MODEL

The reactor is modeled with a two-dimensional boundary layer model which is coupled with a detailed description of the chemical reactions in the gas phase and on the surface. The reactor is a symmetric channel where catalyst (Pt) is deposited on the wall (Figure 1) and typical operating parameters are taken as closely as possible to the microreactor configuration in our experiments.

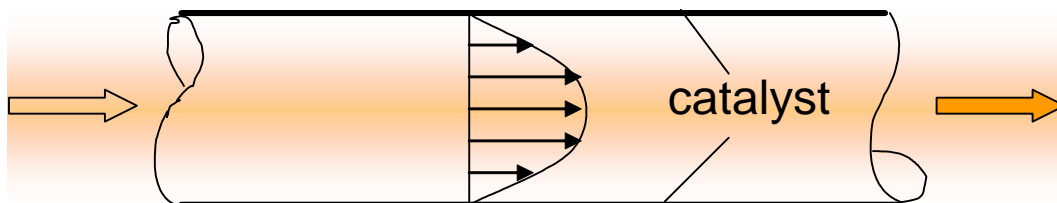


**Figure 1:** A Schematic overview of the microreactor used in the simulation

The gas phase is characterized by the gas temperature as well as mass fractions of the components  $O_2$ ,  $H_2$ ,  $N_2$ ,  $H_2O$ ,  $OH$ ,  $H_2O_2$ ,  $HO_2$ ,  $H$ ,  $O$ . The solid phase is characterized by the wall temperature, surface coverage of all reactants, intermediate species and products on the catalyst. The two-dimensional boundary layer model incorporates balance equations for mass, momentum and energy. An in depth description of the model as well as kinetics is given in Appendix A where model equations are tabulated in Table 2.

A commercially available simulation package CHEMKIN is used as the primary tool for the simulations. The CRESLAF (Chemically Reacting Shear-Layer Flow) routine is used to solve the two-dimensional partial differential equations (PDEs) for a reactive laminar flow. It has a modular structure with interfaces to CHEMKIN utility packages to acquire kinetic, thermodynamic and transport parameters. The mathematical set of equations for the boundary layer flow is described in detail in the CHEMKIN manual [65]. CRESLAF species equations describe the convective and diffusive transport of the chemical species as well as the production and destruction via chemical reactions. The small dimensions of microfabricated systems imply that  $Re = d.v.\rho/\mu$  and  $Pr = \mu.Cp/k$  for 1 mm reactor diameter [Appendix B] are very small for the transport processes for H<sub>2</sub>-air reaction system. As a consequence, the reactive flow in the microchannel is laminar and more easily quantified than the complex, turbulent flows, characteristic of macroscale chemical reactors. The continuum assumption in the boundary layer model [Appendix B] is valid provided the mean free path of the molecules is smaller than the characteristic dimension of the flow domain. The applicability of this approximation for our system has been validated and discussed in detail in Appendix A. One assumption has been taken underlying the boundary layer approximation is that the diffusive transport is negligible compared to the convective transport in the principal flow direction. This simplifying approximation of the reactor behavior in the BL approximation is justified by the fact that very high gas flow rates ( $\approx 9$  m/s) were realized in the experiments, rendering the system highly convection dominant. ( $Pe = Re*Pr \approx 70$ ).

In chapter 4, all simulations have been performed with a fully developed parabolic velocity profile. In practice, gases enter with a flat profile and then gradually develop a parabolic velocity distribution. Therefore, in addition to the fully developed parabolic velocity distribution we also

investigated the influence of the flat entrance velocity profile to ensure the consistency of our numerical results. The results show the same general trend we observe in our all simulations and that study is discussed in Appendix D in detail.

## 3.2 KINETIC MODEL

To describe the ignition behavior as well as quenching effect for different kinds of wall materials, the 2D boundary-layer flow pattern is used with a detailed description of gas phase chemistry as well as surface chemistry. We study the ignition behavior using three types of surfaces i.e. (a) **Inert** (In), (b) **Catalytic** (Pt, Pd) wall and (c) Non-Catalytic **Radical Recombination** (RR) as described in more detail further below.

### 3.2.1 Gas Phase Chemistry

In our simulation, we have used the GRI 3.0 gas phase mechanism given in Appendix A (Table 3). GRI-mechanism [66] is essentially a list of elementary chemical reactions and associated rate constant expressions. This is an optimized detailed chemical reaction mechanism capable of the best representation of natural gas flames and ignition which has been developed by the University of California at Berkeley, Stanford University, the University of Texas at Austin, and SRI International.

For our study we use a subset of this mechanism incorporating all reactions involving only H/O-containing species. It consists of 9 species and 19 reactions and is summarized in Table 3 in Appendix A.

### 3.2.2 Surface Chemistry

SURFACE CHEMKIN utilities are used to process the surface kinetics. An inert surface is an idealized situation which can be realized only computationally. This surface is used as a reference case in our study. SURFACE CHEMKIN is not needed for this wall as this case corresponds to purely homogeneous reactions.

A correct description of the detailed interplay between homogeneous gas phase reactions and heterogeneous surface reactions must consider all reactants and possible reaction intermediates to allow for a description of possible homogeneous-heterogeneous coupling mechanisms. In our study we have used three kinds of surfaces, (I) Platinum, (II) Palladium and (III) Non-Catalytic Radical Recombination walls.

- (I) *Catalytic wall-Platinum*: Surface kinetics of this wall is mentioned in Appendix A. We have employed three different surface mechanisms on Pt to compare the influence of kinetics on the flammable reaction system. These are also tabulated in Appendix A, Table 4-6. For all ignition studies with Pt wall discussed in chapter 4 in our study, the surface kinetics summarized in Table 6 is used. This mechanism seems reliable, since Aghalayam et al. used sensitivity analysis to identify key kinetic parameters, calculated the influence of adsorbate-adsorbate interaction on activation energies and applied numerical optimization to fit the pre-exponential factors. In the mechanism,

- PT(S) indicates a free Pt surface site and species followed by (S) denote adsorbed species. (Due to the isothermal nature of the presented simulations, the simulation results are in fact independent of the thermodynamics of the surface species as long as thermodynamic consistency of the overall mechanism is ensured.). The site density of the Pt surface is set to  $2.71 \times 10^{-9}$  mol/cm<sup>2</sup>, and thermodynamic data is calculated in agreement with the GRI thermodynamic database based on the adsorption-desorption energetics of the catalytic reaction mechanism.
- (II) Catalytic wall-*Palladium*: Surface kinetics of this wall is shown in Table 7 in Appendix A. It was developed by Johansson et.al [67]. In this mechanism, the site density of the Pd surface is set to  $2.52 \times 10^{-9}$  mol/cm<sup>2</sup>.
  - (III) Radical Recombination wall-*quartz glass*: This wall consumes gas phase radicals and mainly recombines them into reactants instead of forming products. It mimics the behavior of quartz or silica. Instead of promoting reactions, this wall hinders the overall reaction progress and basically acts as a “radical scavenger”. The detailed kinetics is also given in Appendix A in Table 8. A previously published kinetics [59] was not thermodynamically consistent and therefore reverse reactions were added to the kinetics in order to obtain a thermodynamically consistent kinetics. The site density of the RR surface is set to  $2.71 \times 10^{-9}$  mol/cm<sup>2</sup> similar to the clean Pt surface.

### 3.3 SIMULATION PARAMETERS & NUMERICS

The reactor was modeled as a symmetric tubular reaction channel. Unless states otherwise, the reaction conditions in all runs were: ambient pressure (1 bar), gas inlet velocity of 9 m/s, a

stoichiometric mixture of hydrogen in air and a fully developed laminar flow profile. The channel diameter was varied between 2 mm and 5  $\mu\text{m}$  and reactor length was adjusted as necessary to observe ignition. We have varied the surface temperature as well as gas phase temperature isothermally from 2000K to room temperature. In addition to reactor diameter, catalyst loading, wall materials, reaction pressure, equivalence ratio, fuel-to-oxygen ratio, oxidants and reaction systems were varied to study the impact of these variables on the ignition in a microreactor.

The simulations were conducted on a SUN Blade 100 workstation, using spatial discretisation of 30-100 mesh points in radial direction with non-uniform grid points distribution (more nodes accumulated around the reaction zone) when necessary. The axial discretisation is adapted by the program as necessary to achieve the desired numerical accuracy. Typical integration times varied between 1 to 10 minutes for a single run.

## **4.0 SIMULATION RESULTS & DISCUSSION: H<sub>2</sub> OXIDATION IN MICROCHANNEL REACTORS**

### **4.1 ISOTHERMAL CALCULATION: REFERENCE CASE - INERT WALL**

To gain a thorough understanding of the reaction mechanism in a microreactor, the highly explosive H<sub>2</sub> oxidation is numerically investigated in a microreactor with different wall materials including an inert wall, catalytic wall (Pt, Pd) and a non-catalytic radical-quenching wall.

The results of the comprehensive numerical investigation in section 4.1 explain the causes of the absence of explosions in microcatalytic reactor in the experimental observation [11] and sets the limits of microreactor operation for H<sub>2</sub> oxidation reaction system. Isothermal operation is simulated in order to focus on kinetic effects separately from thermal effects. While this is obviously difficult to ascertain in an experimental set-up, near-isothermal operation can be realized in appropriately designed microchannel heat-exchanger reactors, as for example demonstrated by Schüth and coworkers [14].

As a reference case, we first studied the ignition behavior of a stoichiometric H<sub>2</sub>-air mixture (H<sub>2</sub>:O<sub>2</sub> = 2:1) in an isothermal microreactor with an inert wall. An inert wall has no influence on the reaction mechanism, so that only homogeneous gas-phase reactions take place. The channel diameter is 1 mm and gas mixtures are fed with 9 m/s linear velocity according to the experiment. The flow in this microchannel reactor is laminar due to the small dimension of

microreactor. Hence the Reynolds number ( $Re$ ) is small (discussed in section 3.1). That justifies the boundary layer approximation (Appendix C) used in the simulation in the two-dimensional reactor model.

Figure 2 shows the 3-dimensional linear velocity profile (left plot) of the feed gases and the temperature distribution at 1173K for the purely homogeneous case. Linear velocity is plotted as a function of radial ( $r$ ) and axial distances ( $z$ ) of the reactor. In this velocity distribution in the left plot, a parabolic velocity profile gradually develops along the reactor length which characterizes the laminar flow in microreactor.

Right plot in Figure 2 shows a constant temperature of 1173K in axial ( $z$ ) and radial ( $r$ ) direction demonstrating the isothermicity maintained in our simulations. where the inlet temperature is set to 1173K and that demonstrates the isothermal operation in our simulation.

These results denoting isothermal operation and parabolic laminar flow distribution in microreactor verifies the basic applicability of the isothermal boundary layer model we used for our major work.

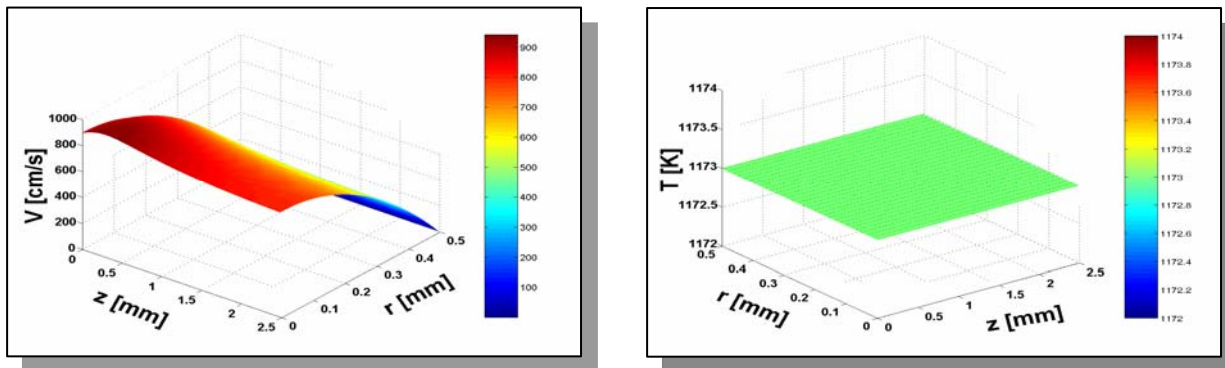


**Figure 2:** Velocity (left) and temperature (right) profile versus reactor length ( $z$ ) and radius ( $r$ ) of the microreactor with 1mm diameter and inert wall at 1173K.

The consumption and formation of main reactant and product gases in this reference case with the inert wall are shown in the concentration profile in Figure 3. A stoichiometric H<sub>2</sub>-air mixture is fed to the microchannel reactor with 9 m/s linear velocity at ambient pressure where temperature is set to 1173K.

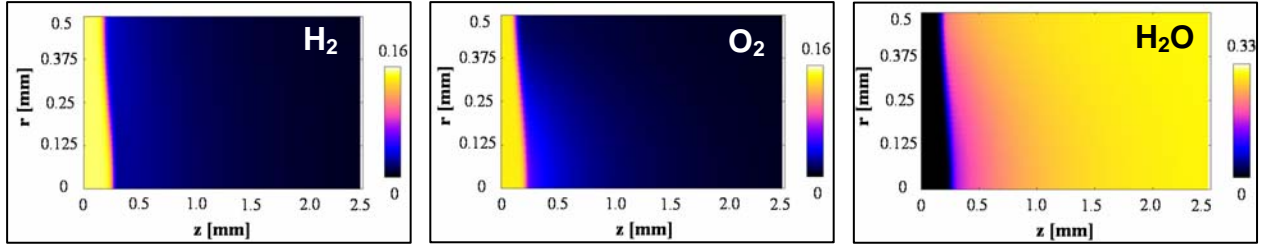


**Figure 3:** Concentration contour plots of H<sub>2</sub> (left), O<sub>2</sub> (middle) and H<sub>2</sub>O (right) versus reactor length (z) and radial distance (r) at 1173K with 1mm diameter.

Concentrations of H<sub>2</sub> (left) and O<sub>2</sub> (middle), and of product H<sub>2</sub>O in molar fraction are plotted Figure 3 within half of the reaction channel of 1 mm diameter. X axis represents the centerline of the flow tube reactor while y axis is the radius of the reactor. The wall is placed at the top end of the plot (r = 0.5 mm). Reactant gases flow from left to right.

We see in H<sub>2</sub> and O<sub>2</sub> concentration profile that ignition occurs with a sharp front which is similarly apparent in product formation (right plot). Furthermore the onset of that ignition front is delayed by 0.3 mm. This delay is termed as ignition delay. It is known that for homogeneous reactions a certain amount of radical pool is needed to ignite the gas mixture [1]. The time needed to build up this radical pool leads to a temporal ignition delay. By studying the reaction in a flow tube configuration, this temporal delay is here transposed into a spatial delay with  $x_{\text{ign}} = v * t_{\text{ign}}$  (where  $x_{\text{ign}}$  is the ignition distance,  $v$  is the flow velocity of the gases and  $t_{\text{ign}}$  is the

temporal ignition delay). Ignition distance in our simulation is defined as the distance from the entrance to the point within the reactor where 50 % of H<sub>2</sub> is converted at the centerline.

Rapid consumption of reactants and formation of product is particularly evident in these three plots near the wall while the plots get more smeared out at the centerline. This is due to the parabolic velocity distribution along the radial direction where maximum velocity is obtained at the center and no slip velocity is observed at the wall. Additionally, the concentration gradient along the radial direction becomes less prominent in case of H<sub>2</sub> concentration as H<sub>2</sub> being the lighter molecule diffuses much faster than O<sub>2</sub>.

It is clear from Figure 3 that homogeneous ignition occurs very fast at 1173K, since ignition, like any chemical reaction, is strongly temperature dependent [1]. At this point, fundamentally it is of interest how ignition behavior varies with temperature for inert wall in microreactor.

Figure 4 shows the ignition distance as a function of temperature. The microreactor has a diameter of 1 mm and the linear velocity is maintained at 9 m/s at ambient pressure.

The plot shows that the reaction ignites essentially immediately at the reactor entrance ( $X_{\text{ign}} \ll 1\text{mm}$ ) above 1000K. A strong increase in ignition distance occurs below 960K with an asymptotic behavior towards a limiting reaction temperature at about 930K.

This trend corresponds to the well-known temporal ignition delay in H<sub>2</sub>-oxidation reactions which has been studied for many decades [1]. Gas phase ignition of a reaction necessitates the build-up of a critical amount of radicals (radical pool). The formation of radicals is strongly temperature dependent and follows the Arrhenius rate expression. Thus, at lower temperatures, ignition occurs with increased spatial ignition delay.

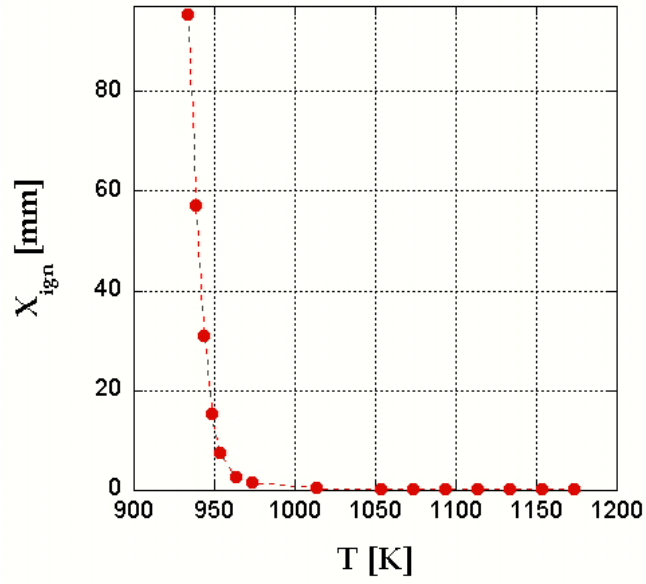


**Figure 4:** Ignition distance vs. reaction temperature in a microreactor with 1mm diameter and inert wall.

Furthermore, the asymptotic behavior of the curve indicates that at temperatures below 930K, no reaction can occur for any reactor length. This is due to the insufficient supply of radicals at these low temperatures. This temperature ( $T = 930\text{K}$ ) is addressed as critical ignition temperature for homogeneous ignition for  $\text{H}_2$  oxidation reaction system.

So far we studied the ignition for purely homogeneous reactions as a reference case. However, in industry, oxidation reactions are typically carried out in presence of catalysts. Therefore, as a next step we investigate the ignition behavior of  $\text{H}_2$ -oxidation in a catalytically coated microreactor using the same reactor conditions as above.

## 4.2 ISOTHERMAL CALCULATION: CATALYTIC MATERIAL - PLATINUM

### 4.2.1 Influence of catalyst on ignition behavior

In this study, Pt is chosen as catalyst for several reasons. Firstly it was used in our previous experiments [3, 11]. It is a well known catalyst for oxidation reactions which is widely used in industry. Furthermore, the kinetics of H<sub>2</sub>-oxidation on Pt have been extensively studied in the past [7, 30, 60, 62, 68, 69].

In addition to the inert wall (homogeneous reactions) and the Pt wall (homogeneous and heterogeneous reactions) we also studied the theoretical case of purely catalytic reactions (without homogeneous reactions) in order to clearly distinguish the influence of catalytic reactions from homogeneous reactions on overall ignition behavior in a coupled case (Pt).

Results for these three cases are summarized in Figure 5. Filled circles represent results with an inert wall (as seen in Figure 4), filled squares represent the Pt wall and open squares represent the purely catalytic case.

Below 1000K, the Pt wall and the purely catalytic case show identical behavior as ignition distance increases continuously with decreasing temperature. It indicates that at these lower temperatures only heterogeneous reactions contribute to the overall mechanism. Heterogeneous reactions dominate over homogeneous reactions due to their smaller activation energy. While homogeneous reactions show the asymptotic behavior with higher ignition delay with lowering temperature following Arrhenius law, the catalytic cases do not run parallel to the inert wall,

but show ignition down to 350K. We did not extend our study below 350K since the Pt surface kinetics has not been verified for that temperature range.

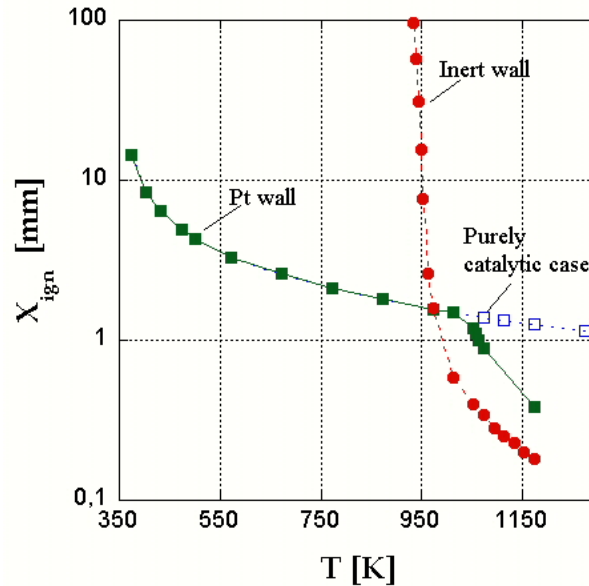


**Figure 5:** Ignition distance vs. reaction temperature for a reactor with 1mm diameter and inert wall (filled circles), Pt-coated catalytic wall (filled squares) and a catalytic wall without gas-phase reactions (open squares)

Above 1000K, the curves for the Pt wall and the purely catalytic case deviate from each other. The ignition distance for the purely catalytic wall continues with an unchanged slope towards higher temperatures, while the ignition distance for the Pt wall shows a sudden bend towards shorter ignition distances. This branch of the ignition curve runs parallel to the purely homogeneous case indicating that the deviation between the Pt wall and the purely catalytic case occurs due to the contributions of homogeneous reactions to the reaction behavior.

At temperatures above 960K, ignition occurs at considerably longer ignition distances for the Pt wall than the inert wall. Apparently, catalytic wall reactions lead to an additional ignition delay at these temperatures. That can be explained with the fact that partial conversion of some of the

reactants by the catalytic surface causes a depletion of reactants (gas phase radicals) in the gas-phase immediately above the surface. This leads to a concentration gradient between the bulk of the gas phase and the boundary layer above the catalyst, resulting in diffusive transport of radicals towards the surface. This boundary layer depletion leads to a delay in ignition of the homogeneous reaction.

Overall, the ignition behavior in the presence of a Pt wall can be understood as a cross-over from a homogeneously (gas-phase) dominated ignition behavior for higher temperatures to a catalytically (surface) dominated behavior for lower reaction temperatures. Thus, Pt wall shows a transition from ignition promoting behavior at low reaction temperatures to an ignition impeding behavior at sufficiently high reaction temperatures.

The contour plot in Figure 6 helps to illustrate the above explanation. Contour plot (similar to Figure 3) of O<sub>2</sub> concentration (mol fraction) along the radius of the reactor ( $r$ ) and the reactor length ( $z$ ) using inert wall (left) and Pt wall (right) are shown. The microreactor has been fed with a gas mixture of H<sub>2</sub> and air at a stoichiometric ratio. Reaction temperature is maintained at 1113K which lies above the critical ignition temperature for homogeneous reactions (see Figure 4).  $r = 0$  depicts the centerline of the reactor while  $r = 0.5$  denotes the wall.

The left contour plot, inert wall, shows a drop in O<sub>2</sub> concentration at about 0.3 mm of reactor length at the centerline of the reactor. No significant radial gradients are observed. On the contrary, in the right contour plot, a strong radial dependency is observed in O<sub>2</sub> concentration. At the catalyst surface ( $r = 0.5$  mm), the decrease in O<sub>2</sub> concentration starts at the reactor entrance ( $z \approx 0$  mm), while at the centerline of the reactor this concentration only starts decreasing after  $z \approx 0.6$  mm into the reactor.

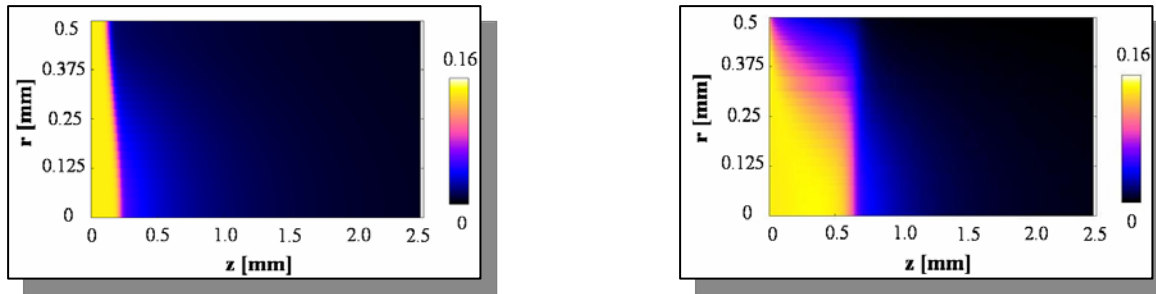


**Figure 6:** Contour plot of  $O_2$  concentration using an inert wall (left) and contour plot of  $O_2$  concentration with Pt wall (right) versus reactor length ( $z$ ) and radius of the reactor ( $r$ ). The reaction temperature is maintained at 1113K.

In the microreactor with the inert wall, the slight decrease in  $O_2$  concentration towards the wall occurs due to the laminar flow of the gases in the reactor as explained in section 4.1. For Pt wall, on the other hand, ignition occurs immediately adjacent to the surface at the beginning of the reactor. Furthermore, ignition is being delayed down at the centerline of the reactor.

The fast catalytic consumption of  $O_2$  in right plot is not surprising, considering that catalysts are being used in catalytic combustion precisely for the purpose for facilitating ignition and conversion. Nevertheless, the less obvious observation is delayed ignition at centerline plot. Looking at Figure 5, it is clear that at 1113K catalyst hinders the overall ignition at the centerline due to the influence of heterogeneous reactions on gas-phase reactions. Partial conversion of some of the reactants by Pt surface leads to a depletion of reactants in the gas-phase right above the surface and hence delays the ignition of the homogeneous reaction. Therefore, homogeneous ignition occurs at  $\sim 0.6$  mm along reactor length followed by fast catalytic reactions at the wall. The boundary layer depletion is clearly apparent in  $O_2$  concentration with Pt wall (right plot) in Figure 6.

#### 4.2.2 Size effect in a Pt-microchannel reactor

A main characteristic of micromachined reactors are the very small characteristic dimensions that can be realized in these systems, leading to exceptionally large surface-to-volume ratios in microreactors. It is expected that large surface area might lead to completely heterogeneously (i.e. surface reactions) dominated reaction systems effectively suppressing homogeneous reactions. Therefore, we studied the influence of the microchannel dimension on the overall ignition behavior for Pt wall in more detail. (Varying the reactor diameter for the inert wall is not a meaningful experiment, since by definition the wall has no influence on the reaction behavior.).

Lowering channel diameter causes larger surface to volume ratio which enhances the impact of catalytic reactions over homogeneous reactions and ensures stronger size effect using Pt wall. This effect is studied in detail in the following Figure 7 using seven different microreactor diameters (2 mm, 1mm, 500  $\mu\text{m}$ , 300  $\mu\text{m}$ , 250  $\mu\text{m}$ , 100  $\mu\text{m}$ , and 50  $\mu\text{m}$ ) with Pt wall.

The curves fall essentially into two groups: the four ignition curves for diameters of 2mm – 300  $\mu\text{m}$  and the three curves for diameters of 250  $\mu\text{m}$ , 100  $\mu\text{m}$ , and 50  $\mu\text{m}$ .

The four curves at larger channel diameters ( $d \geq 300 \mu\text{m}$ ) show qualitatively the same behavior as described in Figure 5, i.e. they show two distinct branches for higher and lower temperatures, respectively. High temperature regime show very little dependence on channel diameters where low temperature branch shows a strong decrease in ignition distances with decreasing channel diameter.

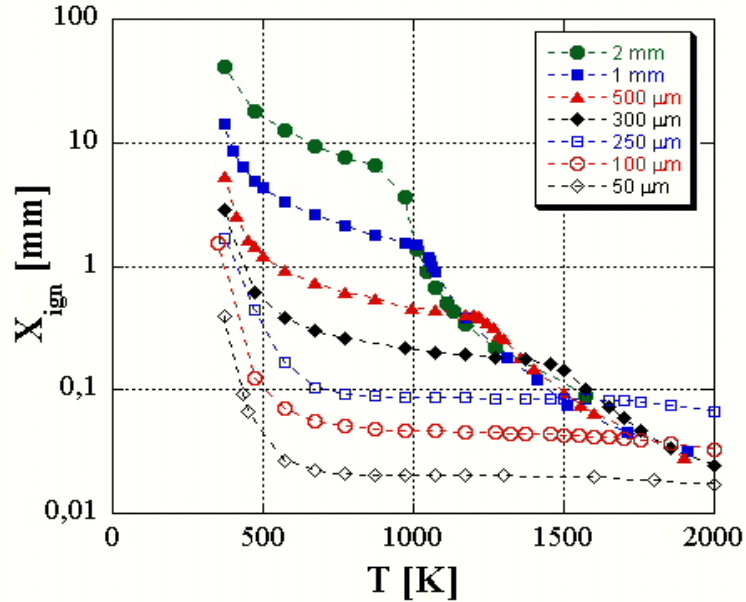


**Figure 7:** Ignition distance versus reaction temperature for a reactor with catalytic Pt-wall varying channel diameters.

In addition to the shift towards longer ignition distances with increasing channel diameter, we also observe a shift towards higher temperatures in the transition point from the catalytically dominated to the homogeneously dominated ignition branch (i.e. the sudden bend in the curve). This shift leads up to a strong qualitative change in behavior of the system as we go from a channel diameter of 300  $\mu\text{m}$  to 250  $\mu\text{m}$ : at smaller channel diameters ( $d < 300 \mu\text{m}$ ), we notice only one branch up to temperatures  $> 2000 \text{ K}$ . Even higher temperatures were not studied since the validity of the reaction kinetics as well as the practical relevance of simulations at such extreme temperature become questionable.

The observation that at high temperature, branches do not differ significantly for different reactor diameters can be traced back to the interplay between reaction and mass transport which underlies the overall ignition process. We know that high temperature branch is homogeneously dominated and homogeneous reactions occur in the bulk gas phase. Therefore, reduced diameters

do not have any impact on the transport path of the reactive molecules as for gas phase reactions molecules do not need to traverse from the bulk to the wall. Hence high temperature branches become negligibly influenced by reactor diameters.

On the contrary, decreasing reactor diameters from 2 mm to 300  $\mu\text{m}$ , low temperature branches strongly differ. At these low temperatures no homogeneous gas phase reaction can occur anymore and the reaction occurs exclusively due to catalytic reactions. As we define ignition in our simulations as the point of 50% hydrogen conversion *at the center line* of the flow channel, we are effectively not observing the ignition process directly, but rather observe the catalytic wall ignition delayed by the transport processes. Since the length of the diffusion path from the center line to the wall increases with increasing channel diameter, this transport process takes correspondingly longer which leads to an increasing (apparent) spatial ignition delay.

This delay is further increased by the additional effect that the changing surface-to-volume ratio has on gas phase concentrations versus catalytic surface reactions. We know that catalytic reactions scale with the surface area (i.e. with  $r$ ), but gas phase concentrations scale with the reactor volume (i.e. with  $r^2$ ). Therefore, as the reactor diameter increases, the surface reaction will take longer to deplete the gas phase sufficiently to observe a 50% drop in  $\text{H}_2$  concentration.

The same reasoning also explains why the transition point shifts towards higher temperatures with decreasing reactor diameter from the catalytically dominated to the homogeneously dominated ignition branch. The relative rate of the catalytic surface reaction increases with decreasing diameter as surface-to-volume ratio increases. Hence the catalytic reaction continues to dominate the overall ignition behavior towards increasingly high reaction temperatures. At channel diameters  $< 250 \mu\text{m}$ , the transition to a homogeneously dominated ignition behavior completely disappears over the whole temperature range studied here. Clearly, somewhere

between the 300  $\mu\text{m}$  and the 250  $\mu\text{m}$  diameter microchannels, the suppressing effect of the catalytic reaction on the homogeneous gas phase reaction becomes strong enough to lead to a complete quenching of homogeneous ignition.

This is exactly the effect that we had earlier [11] experimentally observed. In that case, a complete quenching of (explosive) homogeneous gas phase reactions was noticed decreasing the reactor diameter from about 1 mm to about 100  $\mu\text{m}$ .

A better way of explaining the previous observation is with concentration contour plots. In Figure 8 the top row shows the contour plots of  $\text{O}_2$  concentrations and in the bottom row concentration of H radical for 1 mm, 500  $\mu\text{m}$  and 300  $\mu\text{m}$  microreactor diameters are plotted along axial distance as a function of radial distance.

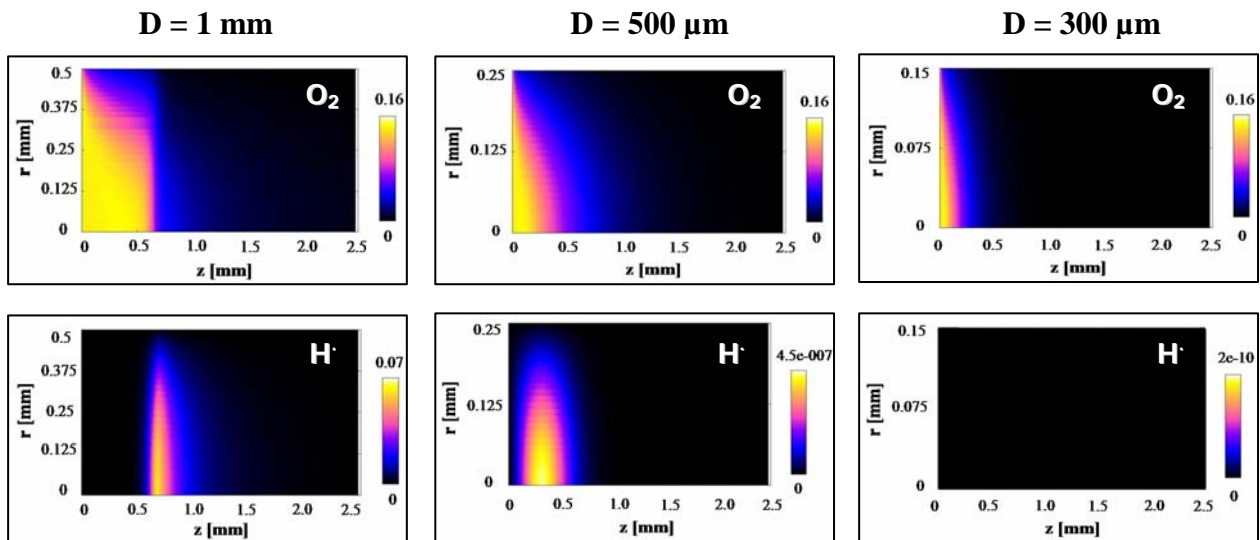


**Figure 8:** Contour plot of  $\text{O}_2$  concentration (top row) and H radical concentration (bottom row) using Pt wall with 1 mm (left), 500  $\mu\text{m}$  (middle) and 300  $\mu\text{m}$  (right) microreactor diameters as a function of axial ( $z$ ) and radial ( $r$ ) distances keeping temperature constant at 1113K.

For a reactor diameter of 1 mm, ignition starts at the surface at  $r = 0.5\text{ mm}$  and  $z = 0.0\text{ mm}$ , while it continues to  $z = 0.7\text{ mm}$  at the centerline of the reactor. A sudden change in the  $\text{O}_2$

concentration profile is noticed as mentioned earlier in section 4.2.1 in Figure 5. Reducing diameter to 500  $\mu\text{m}$ , the  $\text{O}_2$  concentration decreases slightly at the core of the reactor, while the reaction still starts at the beginning of the reactor at the wall and the plot gets smeared out. Most prominently no sudden change in  $\text{O}_2$  concentration plot is observed with 500  $\mu\text{m}$  unlike with 1 mm diameter. Reducing diameter further down to 300  $\mu\text{m}$ , it is seen that ignition occurs instantaneously at the wall and that the ignition delay is reduced to 0.3 mm at the centerline of the reactor.

In the bottom row of Figure 8, we observe a localized H radical concentration of 0.07 mol fraction with 1mm diameter while the concentration drastically drops to  $10^{-6}$  mol fraction in case of 500  $\mu\text{m}$  diameter and the profile moves towards the reactor entrance. Finally with 300  $\mu\text{m}$  reactor diameter there is no detectable H radical concentration any more.

H radicals are known to be a strong indicator of homogeneous reactions [1]. The sudden change in  $\text{O}_2$  concentration due to homogeneous reactions has been clearly reflected in H radical concentration contour plot. The formation of H radical concentration designates when homogeneous reactions start and consume remaining  $\text{O}_2$ . Reducing diameter to 500  $\mu\text{m}$ , the drastic drop in H concentration to  $4.5 \times 10^{-7}$  mol fraction from 0.07 mol fraction indicates that homogeneous reactions are strongly weakened. The shift in H concentration profile towards reactor entrance can be explained in a way that with 1 mm diameter the concentration of H radical is higher by six orders of magnitude compared to 500  $\mu\text{m}$  diameter, hence the development of small H concentration with larger diameter is not numerically visible in the left plot near the reactor entrance unlike with 500  $\mu\text{m}$  diameter. Finally for 300  $\mu\text{m}$  diameter,  $\text{O}_2$  concentration drops much faster due to the higher available surface area with smaller diameter.

Most importantly the complete absence of H radical for 300  $\mu\text{m}$  diameter indicates that the gas phase reactions are completely quenched.

At this point microreactor can be used as an “intrinsically safe reactor” for  $\text{H}_2$  oxidation explosive reaction system. An intrinsically safe system assumes the oxygen and corresponding fuel are present in the atmosphere, but the system is designed in a way so the radical formation due to chain branching reactions in gas phase or thermal energy (for non-isothermal case) can never be high enough to cause ignition at all and the system can be safely operated without explosions. That can be achieved by limiting the amount of radicals formed in the gas phase which can be possible by complete *radical quenching*. In microreactors, due to its higher available surface area catalytic surface with mentioned small diameters  $< 300 \mu\text{m}$  captures all gas phase radicals reaching equilibrium conversion and explosive homogeneous ignition is truly quenched. It refers to the system which behaves inherently safe.

Furthermore, the present simulations also agree well with the experimentally observed behavior indicating that the complete conversion is achieved over just a few millimeter distance in the temperature range between  $\approx 1000 - 1500 \text{ K}$  [3]. This is illustrated in Figure 9.

$\text{H}_2$  concentration at the reactor centerline is plotted as a function of reactor length for 1 mm (left) and 300  $\mu\text{m}$  (right) reactor diameters with Pt wall. Stoichiometric feed mixture is used at the inlet at ambient pressure.

For 1mm reactor diameter, one can again observe the onset of homogeneous ignition by the rapid drop in  $\text{H}_2$  concentrations for  $T \geq 1113\text{K}$ , while the slowly decaying curve for  $T = 1000\text{K}$  indicates only heterogeneous reactions.

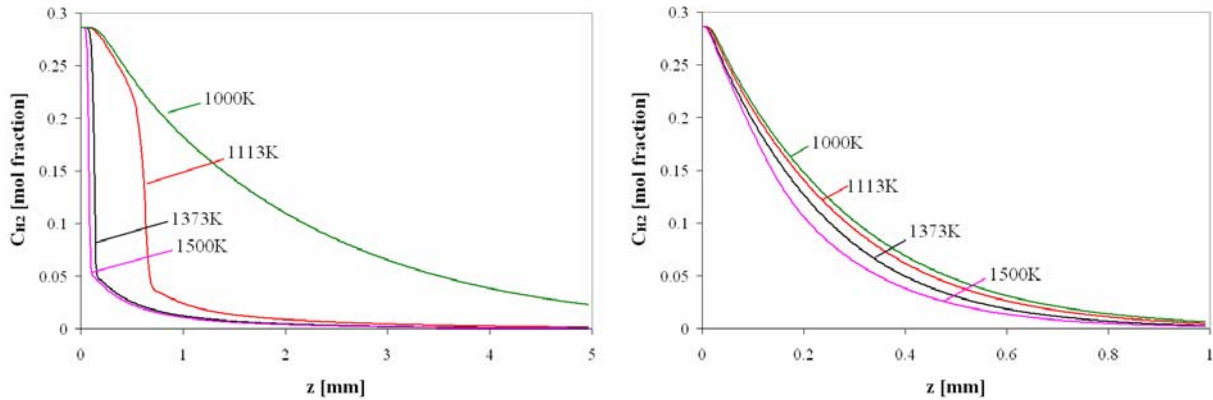


**Figure 9:** H<sub>2</sub> concentration (mol fraction) versus reactor length (cm) in a microreactor with 1mm diameter (left) and 300 μm diameter (right). At inlet stoichiometric feed mixture of H<sub>2</sub>-air is fed in the microchannel reactor with 9 m/s velocity at ambient pressure.

For 300 μm reactor, the concentration curves indicate heterogeneously dominated reaction behavior at all temperatures (Figure 7). Furthermore, H<sub>2</sub> concentration decreases slower in case of larger diameter (note the different scales of the x-axis). Except at the lowest temperature (T = 1000K), the H<sub>2</sub> concentrations drop to zero within about 2 mm for the 1mm reactor channel, while with 300 μm diameter H<sub>2</sub> has been completely consumed within 1 mm at all reaction temperatures.

In case of 1 mm diameter, ignition is entirely homogeneously dominated at these higher temperatures i.e. 1500K – 1000K studied here (see Figure 9). For homogeneous ignition, consumption of H<sub>2</sub> occurs fast following the Arrhenius temperature dependency of the reaction rate. Hence for 1 mm diameter H<sub>2</sub> consumption occurs faster at higher temperatures and gradually decreases conversion with lowering temperatures. Therefore, at 1000K temperature, 100% conversion is not observed for 1 mm reactor diameter within 5 mm reactor length.

Reducing diameter to 300 μm, the whole temperature range belongs to the heterogeneously dominated regime in Figure 9 and the dominant surface reactions enhances H<sub>2</sub> conversion by

consuming gas phase radicals faster due to the higher available surface area as previously explained. That reduces ignition distance at all temperatures for 300  $\mu\text{m}$  diameter which results in full conversion of  $\text{H}_2$  within 1 mm reactor length.

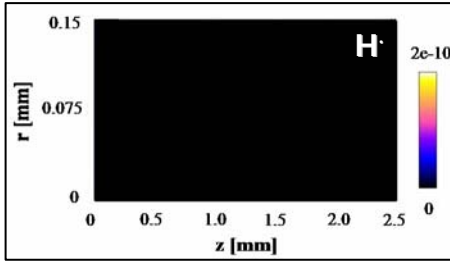
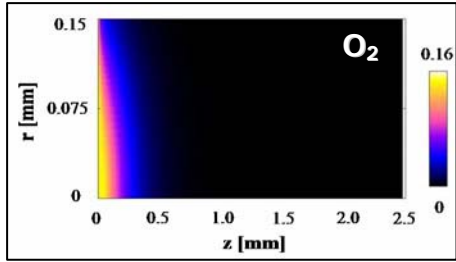
### 4.2.3 Variation of Catalyst Loading

As we have seen complete suppression of homogeneous reactions, at this point we need to answer the question whether this complete quenching occurs due to the fast consumption of reactants by catalytic reactions or whether a true quenching of gas phase radicals takes place.

Therefore, we investigated the influence of the catalyst loading on the heterogeneous-homogeneous interaction which is mimicked by the surface site density in our numerical model. Figure 10 displays a series of concentration contour plots with different catalyst loading. Left column in Figure 10 shows  $\text{O}_2$  concentration and right column are H radical concentration with varying surface site density.

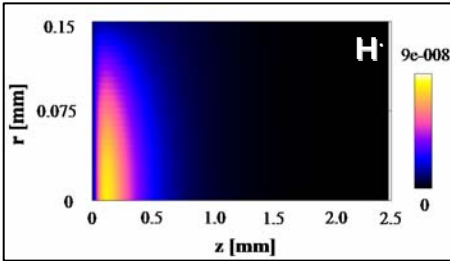
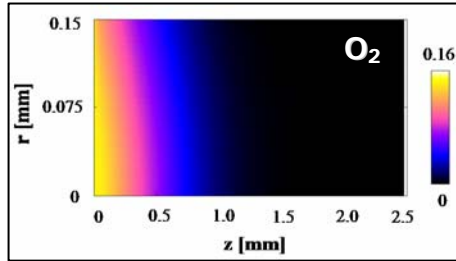
With 300  $\mu\text{m}$  channel diameter for a completely Pt coated surface in plot (I) where site density is  $1.63 \cdot 10^{15} / \text{cm}^2$  [62, 63], fast catalytic consumption of  $\text{O}_2$  is observed and absence of H radical designates complete quenching of homogeneous reactions.

Until plot (III) reducing site density by one order of magnitude, catalytic ignition occurs with higher amount of spatial delay and a corresponding lift in H radical concentration is resulted in. Decreasing vacant sites by 2 orders of magnitude (IV), the heterogeneous reactions are strongly slowed down and the ignition occurs at about 80 mm compared to 0.3 mm in (I). Reducing the catalyst loading by another 2 orders or magnitude (plot V) delays ignition more and it takes place at about 200 mm along the axial direction.



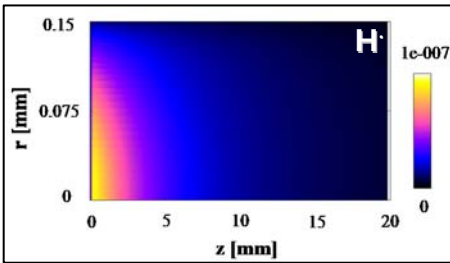
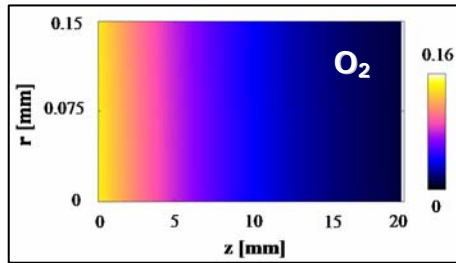
$$\sigma = 1.632E+15 / \text{cm}^2$$

(I)



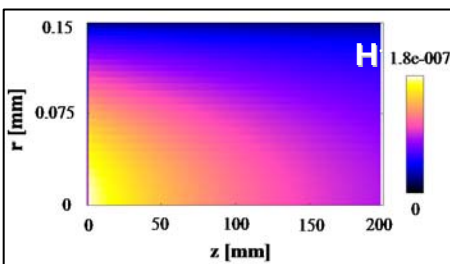
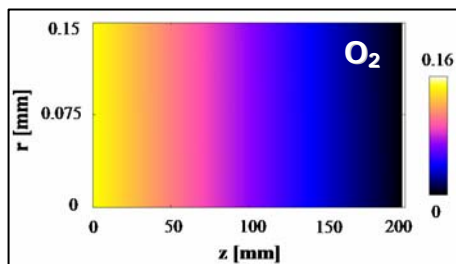
$$\sigma = 4.945E+14 / \text{cm}^2$$

(II)



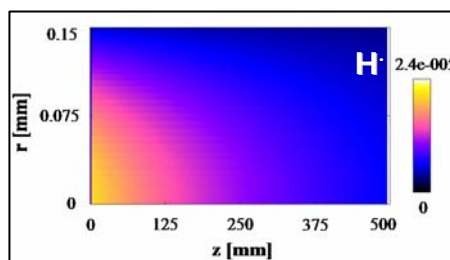
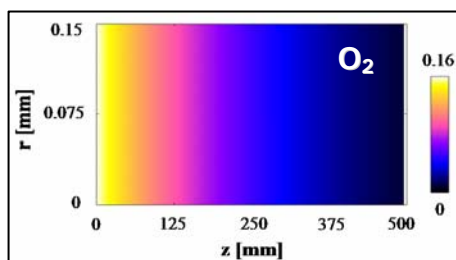
$$\sigma = 1.632E+14 / \text{cm}^2$$

(III)



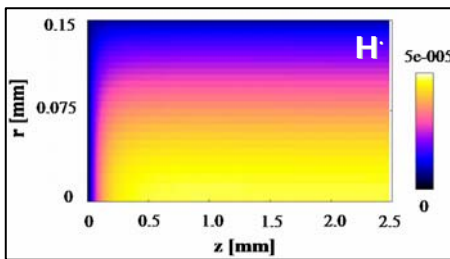
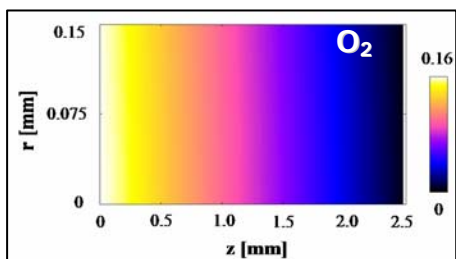
$$\sigma = 1.632E+13 / \text{cm}^2$$

(IV)



$$\sigma = 1.632E+11 / \text{cm}^2$$

(V)



$$\sigma = 3.44E+10 / \text{cm}^2$$

(VI)

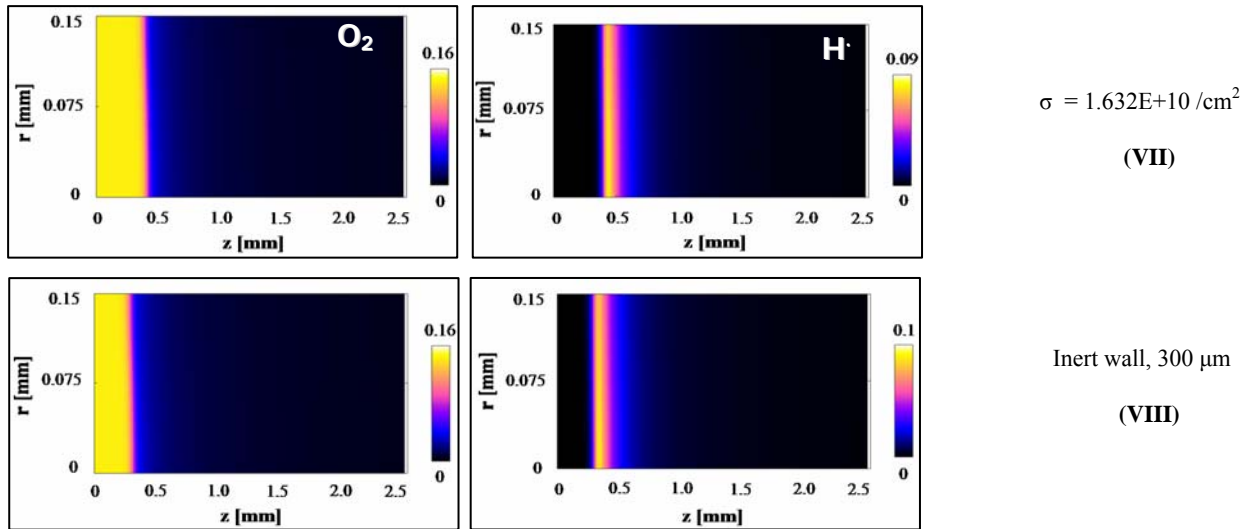


**Figure 10:** Concentration contour plots of  $O_2$  consumption (left column) and H radical formation (right column) for Pt wall with  $300\ \mu\text{m}$  diameter varying catalyst loading at  $1113\text{K}$ .

Slow  $O_2$  consumption indicates an extensive delay in catalytic conversion and simultaneously a small amount of H radical concentration ( $1.8 \cdot 10^{-7}$  mol fraction) is being developed. This indicates that reducing catalyst loading to as little as 1% homogeneous reaction is still very weak reaction pathway. Even further reducing loading to 0.1% in plot (V), H radical concentration increases another 2 orders of magnitude which is still three orders of magnitude below the level of the unhampered homogeneous reaction (see plot VIII). It confirms that homogeneous reaction does not behave as a major contributing pathway even with this reduced catalyst loading.

Only by lowering catalyst loading by another order of magnitude (VII) purely homogeneous case can be reproduced. This investigation confirms that the quenching of explosion occurs in a completely Pt coated channel with  $300\ \mu\text{m}$  diameter only due to the capturing of radicals by the catalyst surface but not due to the fast catalytic reactions.

#### 4.2.4 Limits of reactor safety

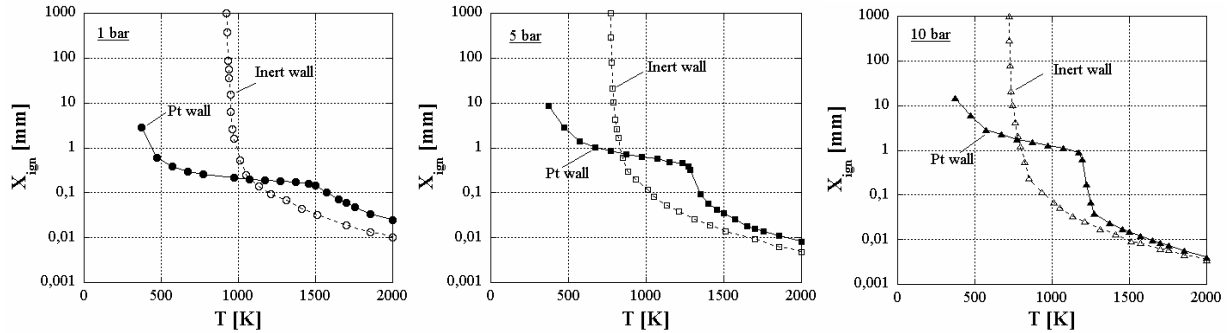
We have shown that microreactors can offer intrinsic reactor safety for explosive reactions. So far our simulation studies were limited to atmospheric pressure. The question concerning process safety, i.e. under which conditions (pressure, temperature and composition) a given reactant mixture tends to ignite, is crucially important when handling high temperature catalytic reactions. It is known that higher pressure highly accelerates the homogeneous reactions as at high pressure intermolecular collision becomes more and more probable due to reduced mean free path, hence it can be expected that the interplay between homogeneous and heterogeneous reactions is strongly affected by the reactor pressure. Therefore the observed kinetic quenching – and hence process safety – will also need to be re-evaluated for different pressure conditions. We therefore studied the influence of reaction pressure between 1 bar and 10 bar on the interplay between homogeneous and heterogeneous reactions in microchannels and in particular on the quenching of homogeneous reactions due to radical scavenging by the catalytic wall

Figure 11 shows the ignition distance for a stoichiometric H<sub>2</sub>-air mixture as a function of temperature for a reactor pressure of 1 bar (left), 5 bar (middle) and 10 bar (right).

Results for a Pt-coated microchannel (filled symbols and solid lines) are shown in comparison with a microchannel with inert walls (open symbols and dashed lines), i.e. purely homogeneous reference case. The simulations are performed for a microreactor with 300 μm diameter.

One can see that the ignition curves for both mechanisms show a qualitatively identical behavior at all three pressures. It is characterized by a continuous increase in ignition distance for the inert

wall, which shows an asymptotic approach to a limit temperature below which no ignition occurs any more (Figure 4).



**Figure 11:** Ignition distance versus reaction temperature at the centerline of a  $300\mu\text{m}$  reactor diameter at 1bar (left), 5bar (middle) and 10bar (right). Filled symbols represent both homogeneous and heterogeneous reactions while open symbols represent the purely homogeneous case.

For the Pt-coated wall, i.e. the fully coupled homogeneous-heterogeneous case, the curves show the general behavior showing two distinct branches, of which the steep, high-temperature branch is dominated by the ignition of the homogeneous gas phase reaction, and the flat, low-temperature branch is dominated by the ignition of the catalytic surface reaction, as described in detail for the ambient pressure case in the previous chapter (4.2.2).

With increasing pressure, both the homogeneous ignition curve and the high-temperature branch of the curve for the coupled heterogeneous-homogeneous (HH) curve shift towards shorter ignition distances. This is due to the increased density of the gas phase, which increases the frequency of intermolecular collisions and hence of reactive events. However, the decrease in ignition distance is more pronounced for the coupled HH curve, which results in a closing of the gap between the purely homogeneous ignition curve and the HH ignition curve. This gap is very pronounced at 1 bar and has almost completely disappeared at 10 bar. Since the delayed ignition

in the HH curve, which gives rise to the gap, is due to the influence of the catalytic surface reaction on the homogeneously dominated ignition behavior (section 4.2.1), this indicates that with increasing pressure the overall reaction is increasingly determined only by homogeneous gas phase reactions. As higher pressure increases the gas density and hence the reaction rate in gas phase that leads to an increasing dominance of homogeneous ignition with pressure.

For an easier comparison, the ignition curves only for fully coupled heterogeneous-homogeneous case for pressures between 0.5 bar and 20 bar are again shown together in Figure 12.

In this plot, it is obvious that the high-temperature ignition branch for the coupled case shifts towards shorter ignition distances with increasing pressure, while the low temperature branch shifts in the opposite direction, i.e. increasing pressure leads to an increased ignition delay. This somewhat surprising finding can be better understood based on an investigation of the concentration profiles inside the microchannel.

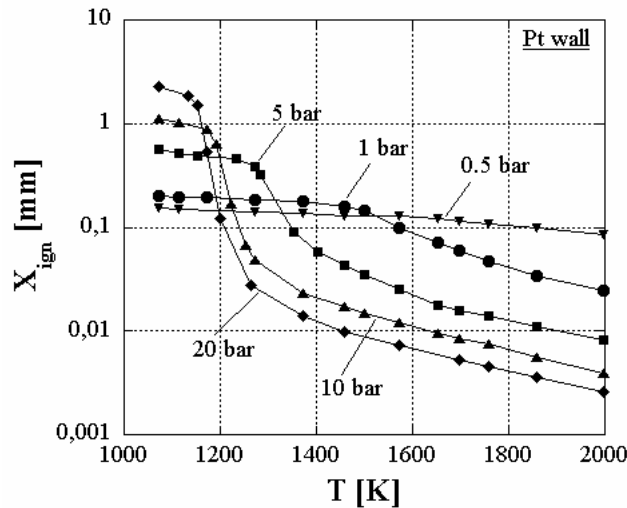


**Figure 12:** Ignition distance versus reaction temperature at the centerline of a 300  $\mu\text{m}$  reactor diameter at 0.5 bar (reversed triangles), 1 bar (circles) and 5 bar (squares), 10 bar (triangles) and 20 bar (diamonds) solely with Pt wall.

Figure 13 shows a contour plot of oxygen concentrations in the upper half of the symmetric, Pt-coated microchannel (the catalytic wall is at the upper end of the graph and the centerline of the microchannel at the bottom end) for three pressures at an intermediate temperature 1253K: 1 bar (left), 5 bar (middle) and 10 bar (right).

At this temperature, the reaction behavior is purely catalytic at 1 bar, strongly homogeneously dominated at 10 bar, and right in the transition region between these two cases for 5 bar (see Figure 12). In agreement with this, one observes a smooth, gradual consumption of oxygen across the microreactor cross section at 1 bar, while at 5 bar oxygen consumption near the catalytic wall still appears gradual but the remaining oxygen near the centerline of the reaction channel is consumed almost instantaneously at about  $z = 0.05$  cm, and the same behavior is observed at 10 bar, now compressed onto an axial scale of about  $z = 0.02$  cm.

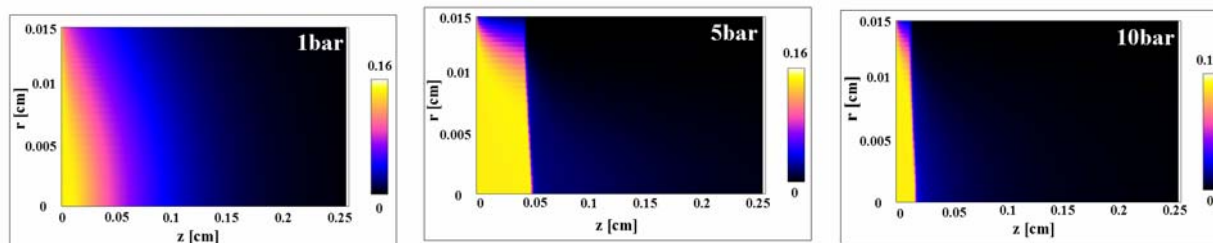


**Figure 13:** Contour plot of  $O_2$  concentration in a 300  $\mu\text{m}$  microreactor using Pt wall at 1 bar (left), 5 bar (middle) and 10 bar (right) reaction pressure. The reaction temperature is maintained at 1253 K. The Pt catalyst is deposited at the top wall ( $r = 0.015$  cm), while  $r = 0$  cm denotes the center line of the reactor. Feed gas mixture flows from left to right.

The concentration profile at 1 bar reflects the discussed effect of oxygen consumption due to catalytic reaction on the Pt-coated wall and subsequent consumption of oxygen in the bulk fluid phase by diffusion transport, leading to smooth concentration gradients in axial and radial

direction. (This effect leads to the previously mentioned boundary-layer depletion effect, i.e. the depletion of reactants in the fluid phase immediately above the catalyst surface).

By increasing the reaction pressure, diffusion is slowed down (since  $D \propto p^{-1}$ ) while at the same time heterogeneous and homogeneous reactions are accelerated due to the increased rate of reactant adsorption as well as the above mentioned increase in gas phase density. However, while the rate of adsorption increases linearly with pressure, the rates of homogeneous reactions are increasing with pressure to the power two or three (for bimolecular or trimolecular reaction steps, respectively). Therefore, at 5 bar and 10 bar, the catalytic reactions almost instantaneously start at the reactor entrance, but after the typical ignition delay of radical reactions, the homogeneous gas phase reactions ignite and consume the remaining oxygen giving rise to the steep oxygen gradient at this point.

Due to the fact that catalytic reactions do not display an ignition delay, there is still a significant amount of catalytic conversion at 5 bar, before homogeneous reactions consume the remaining oxygen. However, increasing the pressure to 10 bar and hence further increasing the rate of homogeneous reactions, the homogeneous ignition delay is significantly reduced and the reaction now occurs almost exclusively due to homogeneous reactions.

At lower temperatures, this picture changes significantly as displayed in Figure 14 for a temperature  $T = 1113$  K.

Shown are contour plots of oxygen concentrations in the upper half of the (symmetric) Pt-coated microchannel for 1 bar (left), 5 bar (middle) and 10 bar (right) reactor pressure at an (isothermal) reaction temperature of 1113 K, i.e. for the low temperature branch.

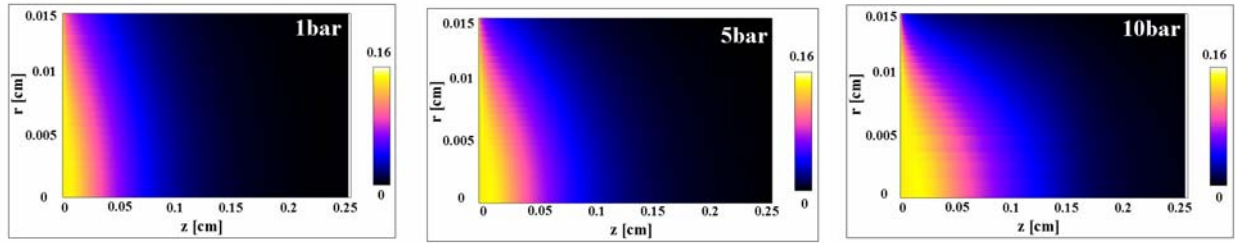


**Figure 14:** Contour plot of  $O_2$  concentration in a  $300\ \mu\text{m}$  microreactor using Pt wall at 1 bar (left), 5 bar (middle) and 10 bar (right) reaction pressure. The reaction temperature is maintained at 1113 K. The Pt catalyst is deposited at the top wall ( $r = 0.015\ \text{cm}$ ), while  $r = 0\ \text{cm}$  denotes the center line of the reactor. Feed gas mixture flows from left to right.

One observes a smooth, gradual consumption of oxygen across the microreactor cross section at all three pressures. However, while the consumption of oxygen near the catalytic wall occurs faster with increasing pressure, the consumption in the bulk fluid phase appears delayed, giving rise to an increasingly spread-out concentration profile.

This can be traced back to the fact that at these lower temperatures the reaction is purely catalytic. Increasing pressure enhances the rate of reactant adsorption and hence accelerates the rate of overall catalytic reaction, thus explaining the faster consumption of oxygen near the catalytic wall. However, due to the absence of homogeneous reactions in this temperature range, oxygen consumption in the gas phase occurs only due to diffusion, which is again slowed down by higher reactor pressures ( $D \propto p^{-1}$ ). Therefore, oxygen consumption at the centerline of the reactor appears slowed down with increasing pressure, as observed in Figure 12. Thus, the two opposing effects of increasing homogeneous reaction rate with increasing pressure and decreasing rate of diffusion with increasing pressure explain the contrasting behavior of the ignition curve for the coupled heterogeneous-homogeneous case at higher and lower temperatures, respectively.

These different dependencies of ignition distance on pressure also reflected in a curve fit [Appendix C] for ignition delay versus pressure at a fixed temperature (for an extended pressure range from 0.5 to 20 bar). The data for the high temperature (i.e. homogeneously dominated,  $T = 1758$  K) branch yields  $X_{\text{ign}} \sim p^{-1.13 \pm 0.09}$  confirming that homogeneous ignition accelerates roughly proportional to the pressure and hence the ignition delay decreases with an inverse proportionality. The data for the low temperature (heterogeneous,  $T = 973$  K) branch yields  $X_{\text{ign}} \sim p^{1.12 \pm 0.07}$ , thus showing that the heterogeneously dominated ignition depends inversely proportional on pressure, as expected for a diffusion-limited process.

Finally, it seems interesting to note that the above reasoning also explains the somewhat puzzling observation in Figure 12, that in an intermediate temperature range between about 1200 K and 1300 K the ignition distance does not appear to follow a ‘logical’ order, i.e. it neither increases nor solely decreases with pressure: As mentioned above, we defined ignition as the point of 50% oxygen conversion at the centerline of the reactor. Therefore, the diffusion-limited ignition distance at low temperatures is exclusively increasing, while the (homogeneous) reaction-limited ignition distance at high temperatures is solely decreasing. However, as apparent from Fig 4, in the transition range between the two regimes, the observed ignition delay depends on the point at which the (fast) homogeneous ignition intersects with the (slow) diffusion-dominated ignition process. Since this transition point shifts with increasing pressure towards lower temperature and hence longer ignition distance, it gives rise to an apparently irregular succession of ignition distances in this intermediate temperature range.

Therefore, in summarizing the dependence of ignition on pressure and diameter we aimed to develop a general expression of ignition behavior with varying pressure ( $P$ ) and diameter ( $D$ ) for  $\text{H}_2$  oxidation reaction system over a Pt catalyst. We therefore mathematically fitted ignition

distance ( $X_{\text{ign}}$ ) data versus temperature (T) separately for the two ignition branches varying reactor diameter (D) and reaction pressure (P). An Arrhenius-type expression was used:  $X_{\text{ign}} = a \cdot e^{[b/(T-c)]} + d$ , where all parameters are attributed significant physical meaning: (a + d) is critical ignition distance, c is critical ignition temperature below which no homogeneous ignition can occur and b is the apparent activation energy of the ignition process.

We can thus derive the activation energy for homogeneous and heterogeneous branches from this expression. The calculated apparent activation energy ( $b \cdot R$ , where R is the ideal gas constant) of the homogeneous branch is 201 kJ/mol. This value matches very well with the elementary reaction step of OH formation in gas phase [Table 3 in Appendix A]. Thus we conclude that the formation of OH species from  $\text{H}_2$  and  $\text{O}_2$  is the rate limiting step in homogeneous ignition. Our calculation is based on the activation energy derived from the calculation of explosion limits for an isothermal reaction system using elementary reaction kinetics from GRI mechanism [66]. It differs from the reported limiting reaction for chain branching in hydrogen oxidation calculated from the experimental observation with the global kinetics reported by Elbe et.al [1]. They reported OH formation from  $\text{O}_2$  and H instead of  $\text{H}_2$  molecule, but this reaction happens to be rate limiting only for  $0.5 < \alpha < 0.9$  shown by Försth [70].

One point has to be clear at this point regarding putting emphasis on H radical concentration in our work to discuss homogeneous ignition though OH adsorption/desorption is the limiting reaction for gas-phase ignition. OH radical also behaves as an indicator of homogeneous reactions which forms at the same axial position like H radical and traces out the occurrence of homogeneous ignition. Additionally, our investigation shows that concentration of H radical is always higher than OH radical for all surfaces we use in this study with 1 mm microreactor diameter. Most importantly, for H radical we can observe a sharply localized concentration with

a shorter axial gradient as this is a highly reactive intermediate species while a smeared out concentration profile with higher gradient is seen for OH radicals as OH is more stable intermediate on catalyst surface compared to H radical. As Pt-OH bond dissociation energy is  $\sim 40$  kcal/mol [71], much higher than that of Pt-H bond, it sticks on the surface and slowly diffuses through the bulk along the reactor length than H molecule that smears out its concentration profile. Due to the sharp localization and higher concentration of H radical and considering its participation as a main species in chain branching reactions [1] it has been referred as the stronger indicator of homogeneous ignition in our work.

The calculated apparent activation energy for heterogeneous branch is 53.4 kJ/ mol. In this case, the detailed mechanism of Pt wall demonstrates that activation energy of three elementary reaction steps, i.e. 7r, 8r, 9f (Table 6, Appendix A) corresponds well to the calculated value. However, to understand this surface ignition chemistry a ‘reaction path analysis’ is performed for  $T = 1113\text{K}$ . This is shown in Figure 15 where to identify the essential reaction steps in the reaction mechanism we performed a sensitivity analysis. The sensitivity of a variable  $y$  against a parameter  $p$  is defined as the relative change in the variable on the change in parameter [57] and can be expressed as:  $S = [(y^*-y)/y]/[(p^*-p)/p]$ . In this method, we slightly perturb a variable and calculated the corresponding change on the reaction rate. For adsorption step the variable is sticking coefficient while for desorption and reaction steps pre-exponential factors are varied in this analysis. The sensitiveness of net reaction rates for 9 reversible reactions at 1113K are shown in the bar graph in Figure 15 corresponding to the reactions at the left. The similar approach has been performed by Veser et.al [57] to study the chemistry and ignition of catalytic oxidation of methane in monolithic reactor.

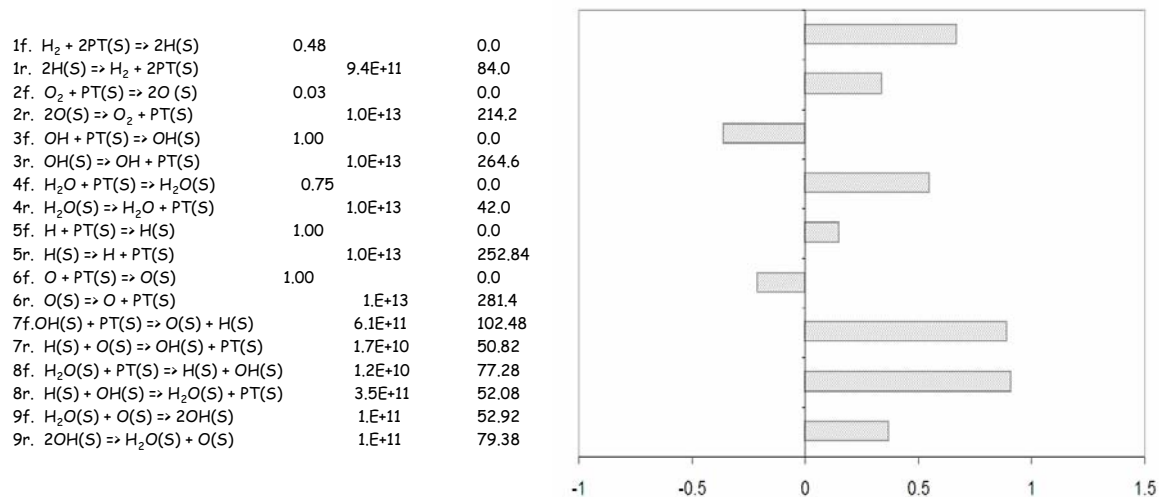


**Figure 15:** Reaction path analysis of Pt surface kinetics where the sensitivity of individual net reaction is shown in the bar graph at right corresponding to the reaction mentioned at the left.

Figure 15 is an illustration of the sensitivity analysis of surface reaction mechanism (Table 6 in Appendix A). This analysis exhibits that reaction 7 (R7) and reaction 8 (R8) are the most sensitive reactions in terms of influencing the net surface reactions. Therefore to further determine the slowest and hence rate-determining reaction among R7 and R8, net reaction rates of all nine surface reactions along the whole reactor length, i.e. without integrating on the surface, are calculated. Figure 16 shows the local rate of the individual surface reaction ( $\text{mol}/\text{cm}^2 \cdot \text{s}$ ) at 1113K (heterogeneously dominated branch) in the primary axis as a function of reactor length and the overall conversion is plotted as a function of reactor length in the secondary axis to give a comprehensible picture of the influential reaction steps on conversion. This plot shows a maximum in reaction rate only for R7 in close proximity to where ignition occurs, while other rates either are gradually decreasing or increasing. This confirms that net reaction rate of R7 i.e.  $OH(S) + PT(S) = O(S) + H(S)$ , is primarily responsible for ignition.

Additionally R7 is detected to exhibit much smaller net rate in comparison to that of R8, i.e.  $\text{H}_2\text{O}(\text{S}) + \text{PT}(\text{S}) = \text{H}(\text{S}) + \text{OH}(\text{S})$ . This reaction rate calculation screened R8 from competing with R7 in determining the rate limiting reaction step. In Figure 16, rate of R6, i.e. adsorption/desorption of O radical shows lower surface reaction rate than R7 which seems to consider in determining rate-limiting reaction steps of the surface kinetics compared to R7. Nevertheless, as we have seen from the reaction path analysis that R7 and R8 are the most two sensitive reactions which has closer energy value with our estimated apparent activation energy, hence R6 has not been taken into consideration for competing rate determining reaction step on surface.

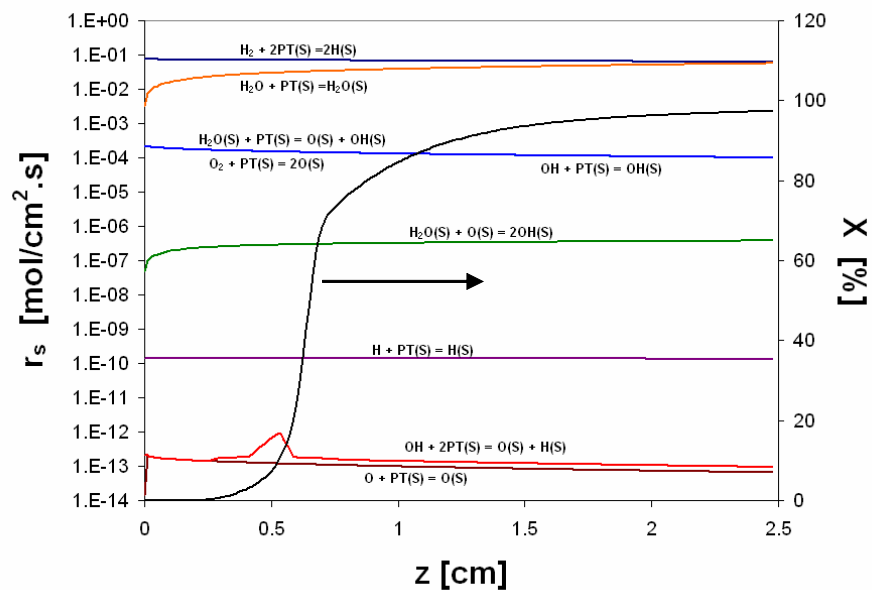


**Figure 16:** Net surface reaction rate ( $r_s$ ) of 9 reversible reactions on Pt surface at 1113K as a function of reactor length ( $z$ ) of 2.5 cm in primary axis and overall conversion across the length in secondary axis to identify the dominant influence of true surface reaction. Reactions corresponding to the surface rate consequently are written above each rate denoting line.

This shows that the adsorption and desorption of OH radicals on Pt surface is also the rate determining step of the heterogeneous branch. Therefore, OH radical is amenable to the measurement of key radicals in ignition (gas phase and surface as well) development for this reaction system which shows agreement with literature [29]. On the other hand, we found a discrepancy in this result with the available literature where the ignition process of Pt catalyst is addressed to be dominated by the adsorption and desorption of hydrogen on the Pt surface [72]. In that work, authors consider the surface kinetics where (1) H<sub>2</sub> desorption energy is highly surface coverage dependent, (2) sticking of O<sub>2</sub> and H<sub>2</sub> are coverage dependent and most importantly (3) activation energy for surface reactions are ~ 20 - 50 kJ/mol lower than the desorption energy of molecular H<sub>2</sub>. On the contrary, in our work, surface kinetics are considered on a clean Pt surface, no coverage dependency is taken into account neither for desorption energy nor for sticking coefficients and the activation energy for surface reactions are ~ 10 - 20 kJ/mol higher than desorption energy of molecular hydrogen. Additionally, in the surface kinetics by Rinnemo et.al [72], no atomic adsorption or desorption is considered unlike the used kinetics in this work. In this way mathematical fit allows identifying critical steps in a coupled reaction mechanism depending on the kinetics available in literature.

So far we have discussed the influence of major constraints in detail in achieving the micro-reactor safety for an explosive gas mixture. We now develop a general mathematical expression which describes the bounds of safe reactor operation for high temperature Pt-catalyzed H<sub>2</sub> oxidation reaction system. To precisely calculate the critical diameter at atmospheric pressure and the maximum pressure within which intrinsic safety in microreactor can be observed, we plotted critical ignition distance (a+d) from the previously described mathematically fitted expression, as a function of reactor diameter and reaction pressure. This is shown in Figure 17.

Dark (blue) surface represents homogeneous ignition while lighter surface (colored) refers to heterogeneous ignition.

The intersecting line of these two surfaces delimits the safe reactor operation, since a critical ignition distance  $X_c$  which is shorter for the catalytic reaction than the homogeneous reaction indicates that the homogeneous reaction has been successfully quenched. From this crossover line we can calculate the exact critical diameter at 1 bar below which no homogeneous reactions occur any more. This diameter is 285  $\mu\text{m}$ . With increase in pressure this critical diameter decreases due to the increased influence of homogeneous ignition, as seen in Figure 17.

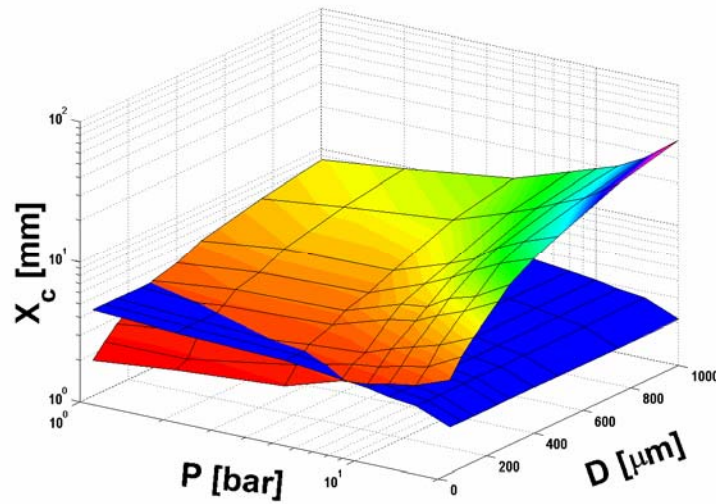


**Figure 17:** 3D plot of critical ignition distance ( $X_c$ ) versus reaction pressure ( $P$ ) ranging from 1 bar to 20 bar and reactor diameter ( $D$ ) varying from 50  $\mu\text{m}$  to 1000  $\mu\text{m}$  (y axis) for  $\text{H}_2$  oxidation in a Pt coated reaction channel.

Next we calculated critical ignition distance for different pressures and fitted the dependence of  $X_c$  on pressure for homogeneous and heterogeneous ignition. We obtained for homogeneous ignition:  $X_{c\_homo} = 1.71 * p^{-2.1 \pm 0.03}$  and  $X_{c\_hetero} = 2.E-3 * p^{-0.92 \pm 0.04}$  for heterogeneous ignition.

From this, the critical pressure is calculated at which critical ignition distance of homogeneous

and heterogeneous ignition become identical. This calculated critical pressure is 9.4 bar. It indicates that above 9.4 bar pressure there is no reactor diameter with which the “intrinsic reactor safety” can be observed for this reaction system.

Finally Figure 18 shows the dependence of the critical diameter on reaction pressure. A curve fit yields  $d_c = 4.61 \cdot 10^{13} \cdot \exp^{[-(P-99.97)/3.632]} - 0.0295$ , and from this expression we can precisely calculate the critical diameter for this system at any pressure. This critical diameter is the limit below which a Pt catalytic microreactor can completely quench homogeneous reactions.

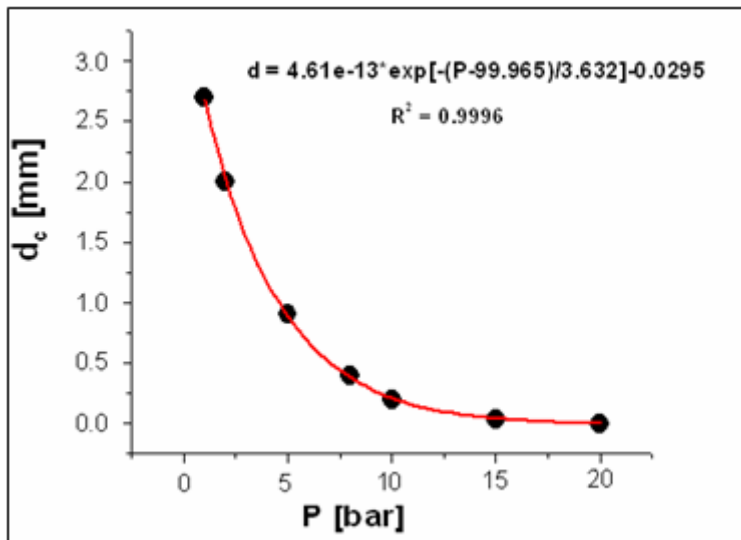


**Figure 18:** Critical diameter in mm (y axis) derived from the mathematical expression as a function of reaction pressure in bar (x axis) shows the exponential dependency.

On the other hand, our previously evaluated critical pressure of 9.4 bar shows from the above equation that the critical diameter would be 1.65 nm at that reaction pressure which is obviously negligible for microreactor operation in terms of reactor dimension.

Overall, these calculations clearly illustrate the bounds of safe microreactor operation for a stoichiometric H<sub>2</sub>-air system. It also indicates that for a specific reaction system, the influence of high pressure needs to be re-evaluated in detail.

#### 4.2.5 Influence of equivalence ratio on ignition

All our results at this point were obtained with stoichiometric conditions. However, it is known that the fuel-to-oxygen ratio in the reactor feed, usually denoted by the equivalence ratio  $\phi = (n_{\text{fuel}}/n_{\text{oxygen}})/(n_{\text{fuel}}/n_{\text{oxygen}})_{\text{stoich}}$ , has a strong impact on the ignition behavior [1], while  $n_i$  denotes the concentration of corresponding species  $i$  in number of moles. Hence,  $\phi$  is defined as the ratio of number of moles of fuel (H<sub>2</sub>) to oxygen divided by the fuel-to-oxygen ratio at the stoichiometric point for total oxidation. We therefore investigated the influence of the equivalence ratio on ignition in microreactor.

In Figure 19, left graph shows the ignition distance for a H<sub>2</sub>-air mixture with  $\phi = 2$  (squares), 1 (circles) and 0.5 (triangles) as a function of temperature for a reactor pressure of 1 bar with 300  $\mu\text{m}$  channel diameter and Pt-coated walls.

All three curves show the same qualitative behavior, with the previously discussed transition from a homogeneously dominated ignition at high temperatures to a heterogeneously dominated ignition at lower temperatures. However, ignition distances in both regimes increase significantly with increasing equivalence ratio, an effect which is particularly pronounced for the low temperature branch. At the same time, the transition point from homogeneously dominated to heterogeneously dominated ignition shifts to slightly lower temperatures with increasing equivalence ratios.

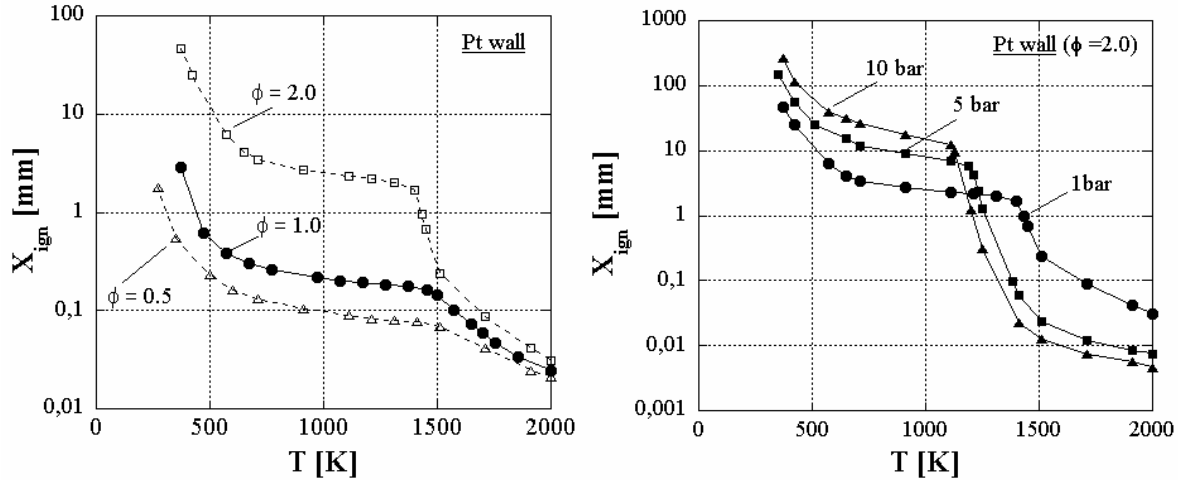


**Figure 19:** In left graph ignition distance versus reaction temperature at the centerline of a 300  $\mu\text{m}$  reactor diameter at 1 bar with  $\phi = 2.0$  (open squares),  $\phi = 1.0$  (filled circles) and  $\phi = 0.5$  (open triangles) with full homogeneous-heterogeneous kinetics. In right, ignition distance versus temperature with  $\phi = 2.0$  varying pressure from 1 bar to 10 bar.

The increase in ignition delay with increasing fuel-to-oxygen ratio for a purely homogeneous case in left plot of Figure 19 can be traced back to the central role of oxygen in the ignition process. We have seen from apparent activation energy calculation that OH formation from molecular  $\text{H}_2$  and  $\text{O}_2$  is the rate limiting step for homogeneous ignition of stoichiometric  $\text{H}_2$  oxidation (see Figure 16).

Since an increasing equivalence ratio leads to a reduced availability of oxygen, the ignition delay – and hence the ignition distance - of the homogeneous branch can be expected to increase with increasing  $\phi$ . Since the reduction in oxygen partial pressure is fairly small (dropping from 0.17 bar at  $\phi = 0.5$  to 0.11 bar at  $\phi = 2.0$ ) compared to the relative increase in hydrogen partial pressure, the effect on ignition distance is comparatively weak.

For the heterogeneous branch, on the other hand, the behavior can be explained by the strongly increasing hydrogen partial pressure with increasing  $\phi$  ( $P_{\text{H}_2}$  increases from 0.17 bar at  $\phi = 0.5$  to 0.44 bar at  $\phi = 2.0$ ). The Pt catalyst is known to be essentially hydrogen poisoned before ignition

of the reaction and the ignition process is thus dominated by the adsorption and desorption of hydrogen on the Pt surface [72]. With increasing hydrogen partial pressure we observe a shift in the adsorption/desorption equilibrium towards adsorption, exacerbating the blocking of the catalyst surface by H atoms which hence results in an enhanced ignition delay in the heterogeneously dominated low-temperature regime. The dominating role of the hydrogen coverage on ignition is emphasized by the pronounced increase in ignition distance with  $\phi$  in left graph of Figure 19.

To understand whether the influence of pressure changes the ignition behavior significantly in case of higher equivalent ratio, we studied ignition for  $\phi = 2.0$  while ranging pressure from atmospheric pressure to 10 bar. This is shown in the right plot of Figure 19 for a 300  $\mu\text{m}$  microreactor diameter with Pt wall. Similar to Figure 12 (see subsection 4.2.4) high temperature branch for coupled case moves towards shorter ignition distances with higher reaction pressures while low temperature branch shows higher ignition delay. This observation has been explained in detail in subsection 4.2.4. Clearly increasing pressure does not change the influence on ignition for a fuel-rich mixture [73].

#### **4.2.6 Influence of oxidant**

It is well known that the explosion limits for  $\text{H}_2$  in oxygen (3.9% - 95.8%) are far wider than for  $\text{H}_2$  in air (4% – 75.6%), since the presence of diluent  $\text{N}_2$ , in large quantity ( $\text{O}_2:\text{N}_2 \approx 1:4$ ), reduces the concentrations of the reactants. Therefore, to understand the impact of  $\text{N}_2$ -dilution on  $\text{H}_2$ -oxidation in a microchannel we compared the ignition behavior for  $\text{H}_2$ -air with that of  $\text{H}_2$ - $\text{O}_2$ .

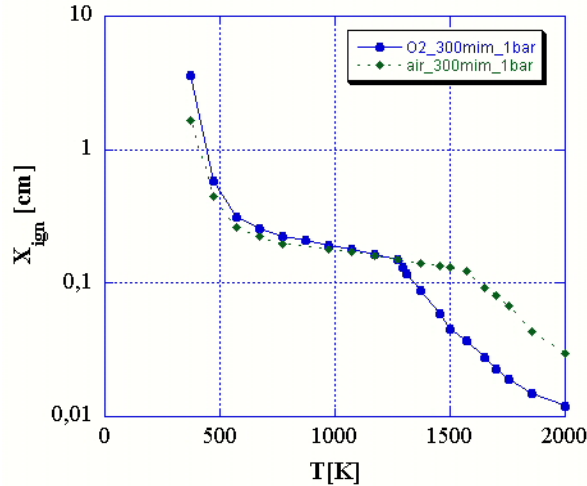


**Figure 20:** Ignition distance versus temperature using H<sub>2</sub>-air and H<sub>2</sub>-pure O<sub>2</sub> stoichiometric feed mixture in a 300 μm microreactor at 1 bar. Filled squares with dotted line represent ignition distance using H<sub>2</sub>-air mixture and filled circles with solid line shows ignition distance using H<sub>2</sub>-pure O<sub>2</sub> mixture.

Figure 20 displays the ignition distance versus reaction temperature plot for a 300 μm Pt-coated microchannel. One can see that the ignition distance for the H<sub>2</sub>-O<sub>2</sub> mixture is strongly decreased at high temperature branches, but the heterogeneously dominated low temperature branch shows slight increase in ignition delay for pure O<sub>2</sub> feed. For H<sub>2</sub>-O<sub>2</sub> mixtures, there is no dilution in the feed gas mixture. Therefore, the concentrations of the reactants H<sub>2</sub> and O<sub>2</sub> in comparison to H<sub>2</sub>-air mixtures and hence the rate of gas phase reaction is increased causing lower ignition delay at higher temperatures.

Due to the higher oxygen partial pressure and as a consequence higher amount of O surface coverage for a H<sub>2</sub>-O<sub>2</sub> mixture, the availability of free sites on the catalyst surface for further heterogeneous reactions is limited. This explains why catalytic ignition delay more in case of H<sub>2</sub>-O<sub>2</sub> feed mixture than that using H<sub>2</sub>-air mixture as reactants.

This is demonstrated in a plot of free surface coverage as a function of reactor length within 5 mm, at 1113K for a stoichiometric H<sub>2</sub>-O<sub>2</sub> mixture and H<sub>2</sub>-air mixture (Figure 21).

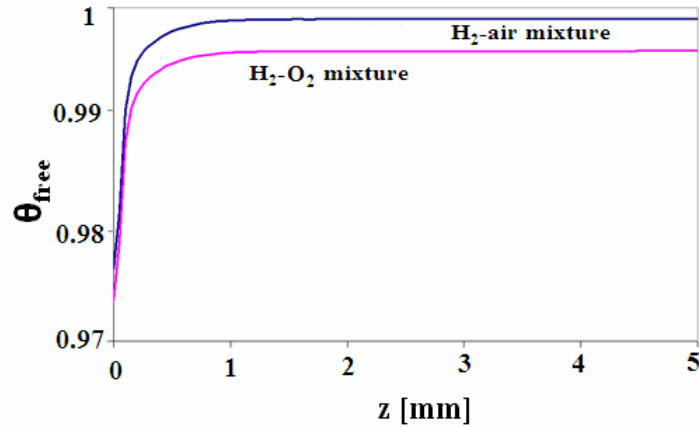


**Figure 21:** O coverage (left) and free surface coverage (right) on Pt surface versus reactor length ( $z$ ) using H<sub>2</sub>-O<sub>2</sub> and H<sub>2</sub>- air as feed mixture in a reactor with 300 micrometer diameter at 1113K.

One can see that, free surface coverage for H<sub>2</sub>-air mixture reaches almost unity and it is higher (0.999) within 5 mm axial distance than for H<sub>2</sub>-O<sub>2</sub> (0.992) feed mixture due to higher O coverage.

At 1113K, catalytic reactions are dominant over homogeneous reactions. Due to the higher surface coverage for a H<sub>2</sub>-O<sub>2</sub> mixture, the availability of free sites is reduced which reduces the rate of catalytic reactions. As a result, this less available free surface slows down the rate of catalytic reactions using O<sub>2</sub> as oxidant in feed mixture than with H<sub>2</sub>-air mixture.

This explains the delayed catalytic ignition in Figure 20 using H<sub>2</sub>-O<sub>2</sub> feed mixture at lower reaction temperatures. This result infers that stoichiometric H<sub>2</sub>-air is better reactant than H<sub>2</sub>-O<sub>2</sub> feed mixture to handle explosive reactions in a microchannel reactor in regards to reactor safety.

#### 4.2.7 Influence of reactor geometry

We have shown in sub-section 4.2.2 that isothermal tubular microreactors behave as an intrinsically safe reactor for H<sub>2</sub> oxidation system diameter < 300 μm. To study the influence of the microchannel geometry, a parallel plate configuration is modeled and compared to the previous results with a tubular geometry. In this configuration, flow is assumed between two infinitely parallel plates, both of which are coated with Pt. Larger 1 mm reactor diameter is investigated compared to 300 μm in evaluating the general ignition trend. The concentration profile of reactant O<sub>2</sub> and intermediate H radical are shown as contour plots in Figure 22 for a stoichiometric H<sub>2</sub>/air mixture at 1113K.

Concentration contour plots are shown as a function of height between two plates (h) and reactor length (z) at 1113K with 1 mm (left column) and 300 μm (right column) diameters. The height of planar reactor is twice of the tubular reactor radius. Inlet conditions are maintained identical as with tubular reactor for stoichiometric H<sub>2</sub>-air mixture. The geometry is axisymmetric around the centerline of the reactor.

For 1 mm diameter ignition starts at the wall while it is delayed by about 0.6 mm at the centerline. Ignition at the surface occurs faster with 300 μm and no steep gradient is observed any more. As discussed earlier, H radical indicating homogeneous reactions develops at the same axial distance where the steep drop in O<sub>2</sub> concentration profile is observed. H concentration with 1 mm diameter is 0.09 mol fraction which drops by six orders of magnitude with 300 μm diameter indicating a strongly weakened homogeneous reaction.

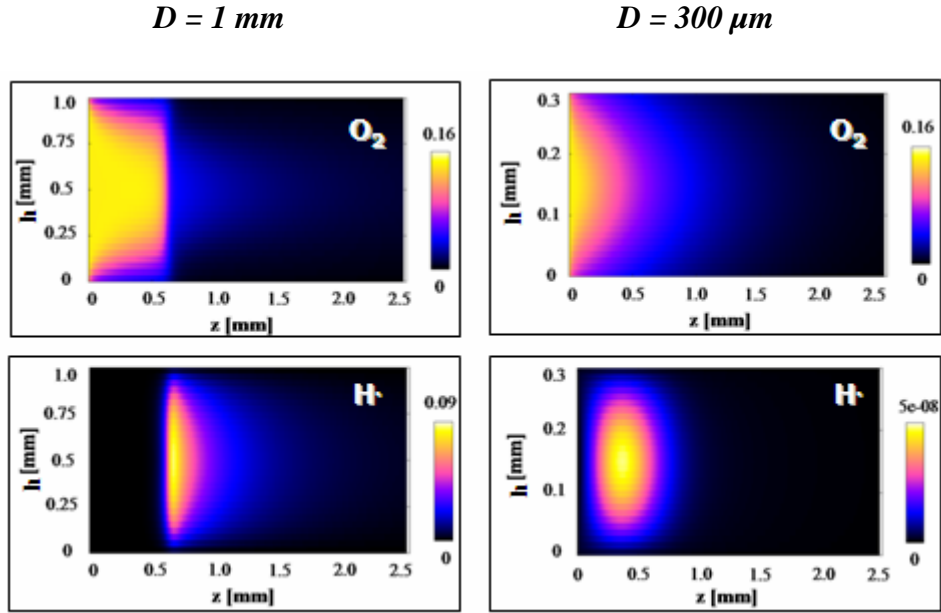


**Figure 22:** Concentration contour plots of  $O_2$  (top row) and H radical (bottom row) versus height (h) and reactor length (z) for 1 mm and 300  $\mu\text{m}$  reactor diameters with planar geometry. Stoichiometric  $H_2$ -air mixture is fed at inlet with 9 m/s velocity at 1 bar for isothermal operation. Temperature is set to 1113K.

The similar  $O_2$  concentration profile in planar geometry to the tubular geometry (see Figure 8) ensures the general ignition trend for coupled  $H_2$  oxidation reaction in microreactor. On other hand, formation of intermediate H species is higher in planar geometry for both diameters than tubular reactor indicating an extended influence of homogeneous ignition on the overall ignition behavior. However, while a small amount H radicals is observed in Figure 22 for 300  $\mu\text{m}$  width is observed unlike in tubular reactor, the magnitude is negligible. In terms of gas-phase reactions quenching, this observation infers that quenching will occur at slightly smaller reactor dimensions in a parallel plate reactor in comparison to a tubular reactor, but the differences were sufficiently small that further investigation seemed irrelevant.

Overall, the detailed numerical simulation of hydrogen oxidation in a microreactor with Pt-coated surface revealed a transition from ignition inhibiting behavior at high temperatures to ignition promoting behavior at low reaction temperatures. Reaction path analysis of surface reaction rates and apparent activation energy from a derived mathematical expression shows that formation of OH from H<sub>2</sub> and O<sub>2</sub> molecules in gas phase is the rate determining step in the gas phase. On the other hand, dissociative adsorption of OH to O and H on Pt surface is the rate limiting reaction for the surface reaction. Most importantly, this study showed that catalytic microreactor with 285 μm diameter can exhibit “intrinsic reactor safety” by completely suppressing homogeneous explosive ignition at ambient pressure. This explains the experimental observation of the absence of explosion by Veser et.al [11]. We also found that 9.4 bar pressure is the limit within which reactor safety can be obtained in Pt-coated microchannel reactor.

### **4.3 ISOTHERMAL CALCULATION: CATALYTIC MATERIALS – PALLADIUM**

Pd surface is also widely used catalytic surface for combustion studies and especially used as oxidation catalyst. Pd shows a high oxidation activity even under fuel lean conditions unlike other noble metal catalysts [74]. Hydrogen has a high diffusivity in Pd and hence it can penetrate into the bulk of the Pd catalyst and is stored in the bulk during reactions. Recently, Lunsford et.al reported direct hydrogen-per-oxide formation from H<sub>2</sub> and O<sub>2</sub> over colloidal Pd [75]. These days the demand for H<sub>2</sub>O<sub>2</sub> production is increasing due to the increased use of hydrogen peroxide as a

bleaching agent in paper industry [76]. It is reported in [77] that Pd will be the metal of choice in catalytic oxidation reactions due to its high oxidation activity along with PdO which also act as an active oxidation catalyst. Prioritizing those important applications of Pd, it is being numerically studied here as an interesting alternative catalytic material for high temperature catalysis in a microchannel reactor.

#### **4.3.1 Effect of wall material on ignition behavior**

Ignition behavior of a particular reaction system is strongly dependent on the properties of wall material used in the reactor. Therefore, it is of interest to investigate how differently ignition of H<sub>2</sub> oxidation varies in a Pd-coated microchannel reactor compared to Pt surface. The results of the simulations on H<sub>2</sub>-oxidation are shown in Figure 23 (diamonds) in comparison to the previously discussed cases of the purely homogeneous reactions (circles) and the Pt wall (squares). Inlet conditions were set to 9 m/s for linear velocity at atmospheric pressure using H<sub>2</sub>-air stoichiometric mixture.

Pd wall shows transition from homogeneously dominated to heterogeneously dominated branch similar to Pt wall. The high temperature branch shows shorter ignition distances than Pt wall, while low temperature branch exhibits higher ignition delay. The ignition delay for the low-temperature heterogeneous branch can be traced back to higher sticking coefficient of oxygen (0.45 on Pd vs. 0.023 on Pt, see Table 6 and Table 7 in Appendix A). In agreement with this, Spicer et.al [78] reported that at atmospheric pressure Pd sites are essentially covered with oxygen leaving very few sites for H<sub>2</sub> adsorption. This higher O coverage on Pd surface retards the ignition in heterogeneously dominated branch resulting in a longer ignition delay.

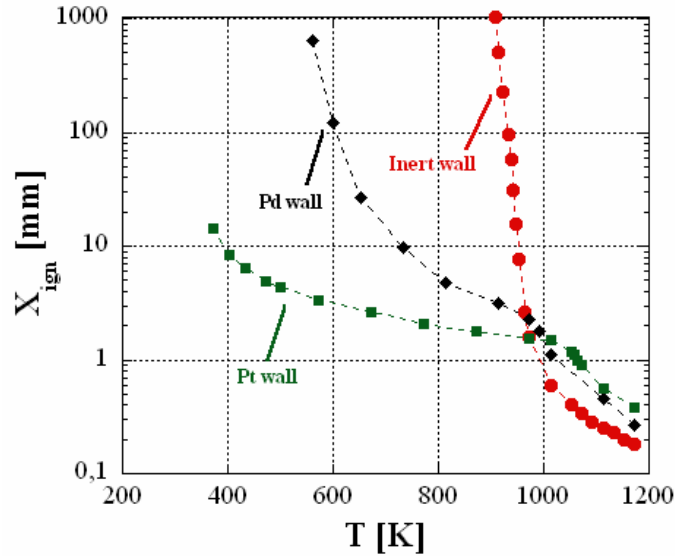


**Figure 23:** Ignition distance vs. reaction temperature for a microreactor with 1 mm diameter and inert wall (circles), Pd coated (diamond) and Pt coated catalytic wall (squares).

The reduced ignition delay at high temperature branch is also caused by the higher O coverage on the surface which increases the partial pressure in gas phase. Increase in pressure accelerates intermolecular collisions resulting in higher homogeneous reactions and that reduces the ignition distance at homogeneously dominated high temperature branch.

The above explained different features become more apparent in another set of concentration contour plots comparing the behavior of  $H_2$ /air concentrations in a Pd microchannel with a Pt and inert microchannel (Figure 24).

In the left column of Figure 24,  $O_2$  concentrations are plotted versus the radius and length of the microreactor and in the right column H radical concentration is shown. Reaction temperature is kept constant at 1113K.

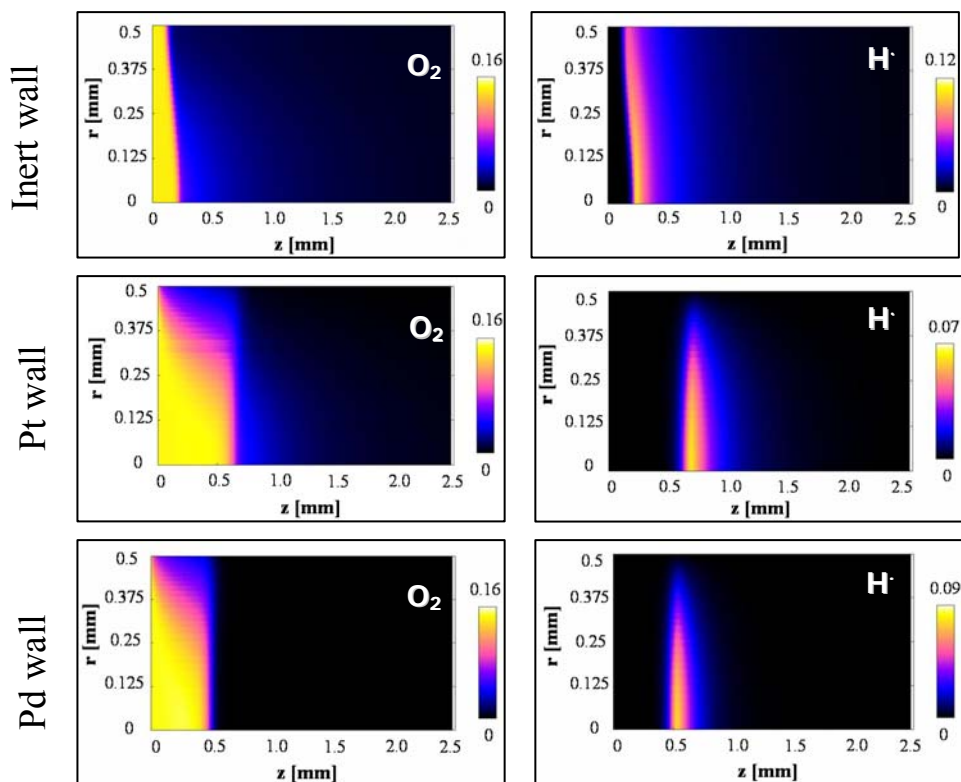


**Figure 24:** Contour plots of  $O_2$  concentration (left column) and  $H$  concentration (right column) with 1mm diameter at 1113K using inert (top), Pt wall (middle) and Pd wall (bottom).

For Pd wall,  $O_2$  concentration starts decreasing right at the surface at the reactor entrance and propagate to the core while we see a sudden change at about 0.4 mm along  $z$  axis. This is the BL depletion effect due to the presence of catalytic wall which we have previously discussed (see section 4.2). Consequently the  $H$  radical concentration also develops at about 0.4 mm in axial direction with a maximum concentration of 0.09 mol fraction. This onset of homogeneous reaction is delayed in comparison to the purely homogeneous reaction (inert wall, top row), but faster than for a Pt wall (middle row) as reflected both in the  $O_2$  and  $H$  concentration profiles. This indicates that Pd – like Pt – inhibits homogeneous ignition, but is less efficient in performing this due to a lower catalytic activity.

### 4.3.2 Size effects in a Pd-microchannel reactor

Complete suppression of homogeneous reactions with Pd surface in microchannel reactor can possibly increase its use as a combustion catalyst. Therefore, as a next step we studied the influence of reactor dimension on overall ignition with Pd surface. Figure 25 shows the ignition distance vs. reaction temperature plot where diameters are varied from 1 mm to 100  $\mu\text{m}$ .

Similar trend is noticed like in Pt wall. With larger diameter from 1mm to 225  $\mu\text{m}$ , transition from homogeneous (high T) to heterogeneous branches (low T) is seen.

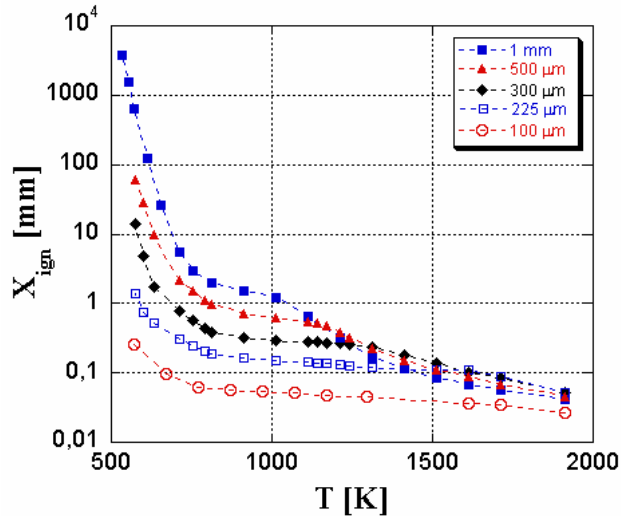


**Figure 25:** Ignition distance versus reaction temperature for a reactor with Pd coated wall and varying channel diameter from 1 mm to 100  $\mu\text{m}$ .

However, one distinctive difference is noticed compared to Pt surface. In Pt wall (Figure 8) homogeneous branch totally disappeared with diameters below 300  $\mu\text{m}$  while interestingly high T - homogeneous branch is still apparent with 225  $\mu\text{m}$  in case of Pd surface. 100  $\mu\text{m}$  diameter exhibits the only heterogeneously dominated branch where we can expect complete quenching of homogeneous reactions. Furthermore, heterogeneous branch continues up to 500K instead of

room temperature discussed as seen for Pt before. The heterogeneous reactions happen to be very slow < 500K temperature on Pd surface and at those temperatures the overall process becomes kinetically controlled [77] which is not observed in the ignition profile in Figure 25.

Comparing to the Pt surface, higher ignition delay is evident for all diameters across the whole temperature range from 500K to 2000K.

In Figure 26, O<sub>2</sub> concentration profiles (top row) along the reactor length are shown for a Pd coated microchannel. The profiles are qualitatively similar to those in Figure 8 for Pt wall. As before a sudden change in concentration is seen with 1mm diameter while the consumption of O<sub>2</sub> occurs sooner within 0.5 mm axial distance than with Pt surface.

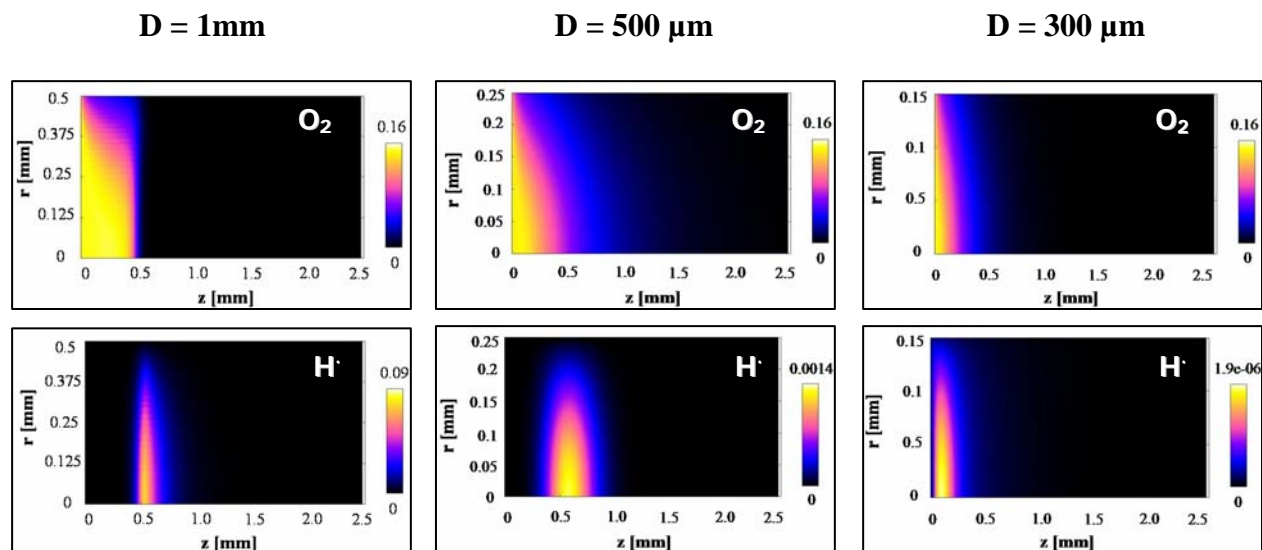


**Figure 26:** Contour plot of O<sub>2</sub> concentration (top row) and H radical concentration (bottom row) using Pd wall with 1 mm (left), 500 μm (middle) and 300 μm (right) microreactor diameters keeping temperature constant at 1113K.

A maximum in H radical concentration reflects the homogeneous ignition in the bottom graphs where a maximum of 0.09 mol fraction is observed. As H radical is a strong indicator homogeneous reactions, comparing with 0.07 mol fraction maximum H concentration for Pt

surface in Figure 25, this illustrates the previously mentioned (4.3.1) higher influence of homogeneous reactions than with Pt wall. Reducing diameter to 500  $\mu\text{m}$ ,  $\text{O}_2$  consumption near the surface occurs even faster and plot gets smeared out. Correspondingly a drop from 0.09 to 0.0014 mol fraction is observed in H radical concentration which denotes that homogeneous reaction gets strongly weakened. Finally, with 300  $\mu\text{m}$  diameter,  $\text{O}_2$  is consumed much faster signifying that reactions are being highly accelerated. Although H radical concentration drops from 0.0014 mol fraction 1.9E-06 mol fraction denoting three orders of magnitude reduction in homogeneous reactions. There is still numerically detectable H radical concentration with 300  $\mu\text{m}$  diameter. Here is the prime discrepancy observed in comparison to the Pt wall where a “complete quenching” of homogeneous reactions was observed with this diameter at the same temperature. Nonetheless, Figure 25 establishes that Pd surface with diameters < 225  $\mu\text{m}$  entirely can quench explosive homogeneous reactions.

### **4.3.3 Limits of reactor safety: Pt vs. Pd**

To judge the range of safe reactor operation against the Pt wall, similarly we evaluated the critical diameter and pressure for Pd catalytic wall (see section 4.2.4). Figure 27 shows a 3D plot of critical ignition distance as a function of reactor diameter and reaction pressure.

In this plot, dark surface denotes homogeneous ignition while lighter surface is the representative of the heterogeneous ignition. As Pd surface favors homogeneous reaction for  $\text{H}_2$  oxidation reaction system due to high O surface coverage, reactor safety is observed within a smaller parameter region. As a consequence, following the analogous procedure of determining critical

diameter for Pt wall (see explanation for Figure 17), we calculated the critical diameter ( $D_c$ ) for Pd wall at ambient pressure to be 125  $\mu\text{m}$ .

Furthermore, beyond 3.8 bar critical reaction pressure ( $P_c$ ) intrinsic reactor safety in a Pd-coated microchannel reactor can not be observed. Both parameters ( $D_c$  and  $P_c$ ) are much smaller than those with Pt surface.

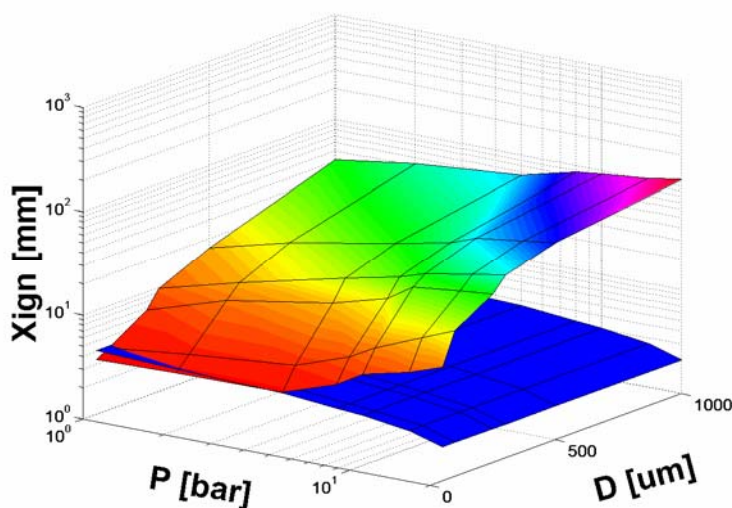


**Figure 27:** 3D plot of critical ignition distance (z axis) versus reaction pressure (x axis) ranging from 1 bar to 20 bar and reactor diameter varying from 1000  $\mu\text{m}$  to 50  $\mu\text{m}$  (y axis).

Overall, we see that a Pd-coated microchannel shows a qualitatively the same ignition behavior in  $\text{H}_2$  oxidation as Pt: the influence of homogeneous reactions is reduced and at sufficiently small diameters homogeneous reactions can be completely quenched. However, due to lower catalytic activity of Pd, critical quenching diameters and critical pressures are significantly lower than for Pt surface.

Furthermore, Pd is being considered as a plausible catalyst for hydrogen per-oxide production in industry since last decade [79]. A mechanistic study has been generated in terms of improvement

of H<sub>2</sub>O<sub>2</sub> production using Pd as catalyst material and how other catalysts influence H<sub>2</sub>O<sub>2</sub> production is been discussed in Appendix G.

## **4.4 ISOTHERMAL CALCULATION: NON-CATALYTIC MATERIAL - ‘RADICAL RECOMBINATION’**

To further comprehend the influence of different wall materials on H<sub>2</sub>-oxidation ignition, we additionally investigated quartz glass as a non-catalytic wall material in our ignition study. All real surfaces are known to behave as sink or source of radicals. Quartz glass is shown to act as a sink of radicals i.e., it does not behave as a typical catalytic surface but is capable of adsorbing radicals from the gas phase and recombine them into reactants. It implies that instead of promoting a reaction, this surface rather hinders the overall reaction progress. We model this type of surface therefore as a generic “radical recombination” (RR) surface, the kinetics of which are described in detail in Table 6 [Appendix A].

### **4.4.1 Ignition in H<sub>2</sub>-oxidation over a ‘Radical-Recombination Wall’**

We studied the impact of non-catalytic RR wall on overall ignition in comparison to the catalytic materials, i.e. Pt. The results of the simulations are shown in Figure 28 (triangles) in comparison to the previously discussed cases of the purely homogeneous reactions (circles) and the Pt wall (squares). The same initial conditions were used with 9 m/s linear velocity and atmospheric pressure using H<sub>2</sub>-air stoichiometric mixture.

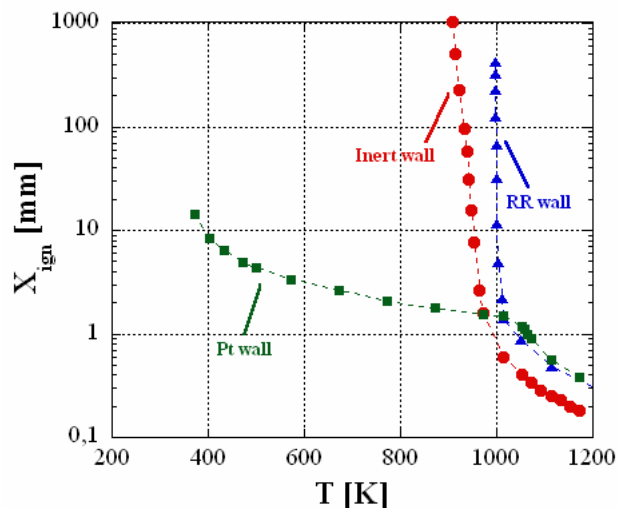


**Figure 28:** Ignition distance vs. reaction temperature for a microreactor with 1 mm diameter and a radical recombination wall (triangles), inert wall (circles) and Pt coated catalytic wall (squares).

Two main points can be seen from the ignition behavior of RR wall in Figure 28. One is that RR curve closely follows the curve for the purely homogeneous case but is shifted to higher ignition distances. Furthermore the overall ignition stops at a reaction temperature of 997K.

Regarding the first observation in case of RR wall, the parallel shift to slightly higher ignition distances in comparison to the inert wall can be expected from the chemical nature of the RR wall. Compared to the corresponding shift in the high-temperature regime in case of platinum, this shift is less for the RR wall as the quenching effect of the radical recombination reactions is weaker than the quenching effect of the catalytic surface. This can be explained by the fact that the catalyst surface permanently removes intermediate radical species from the gas phase by converting them into reaction products, while the radical recombination wall mainly converts these reaction intermediates back into initial reactants and therefore keep them available for further reaction events.

The second observation - the complete quenching at  $T=997\text{K}$ - can be explained by the fact that at lower temperatures for a RR wall, the rate of radical scavenging effect predominates over the rate of product formation (forward reaction rate). Therefore, while the ignition curve for purely homogeneous case continues to infinitely long ignition distances, the dominating radical scavenging effect of RR wall completely quenches all the reaction progress.

The above explained different features between the three different wall materials are reflected in another set of concentration contour plots is shown in Figure 29. In the top row of Figure 29,  $\text{O}_2$  concentrations are plotted versus the radius and length of the microreactor and in the bottom row H radical concentrations are shown. Reaction temperature is kept constant at  $1113\text{K}$ .

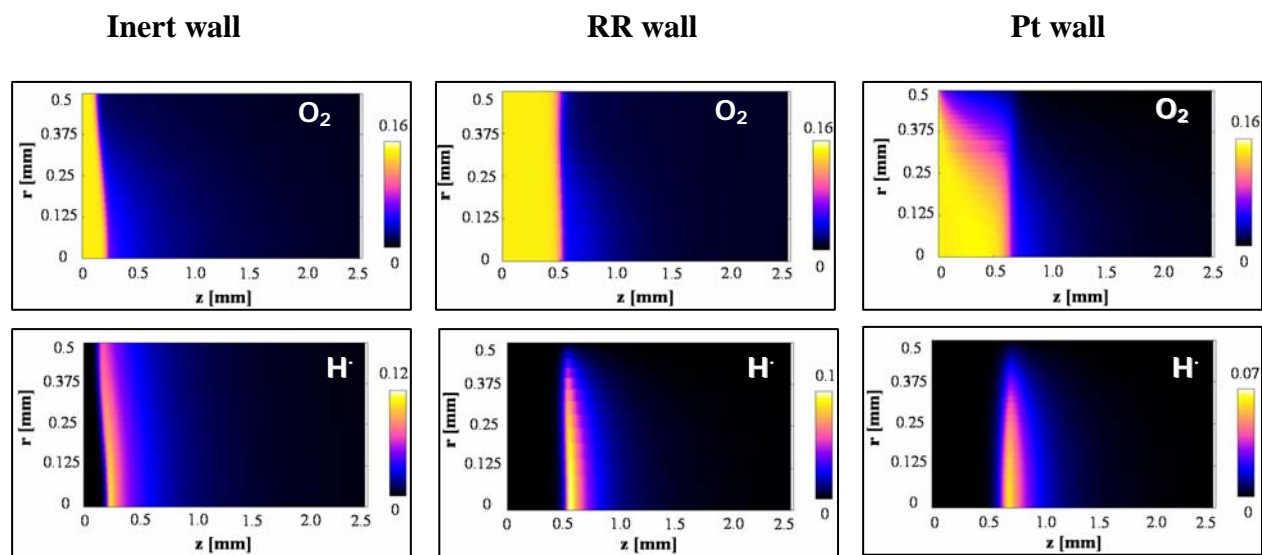


**Figure 29:** Contour plots of  $\text{O}_2$  concentration (top row) and H concentration (bottom row) with 1mm diameter at  $1113\text{K}$  using inert (left), RR wall (middle) and Pt wall (right).

As seen in Figure 29,  $\text{O}_2$  concentrations do not show a radial dependency except for the catalytic wall (Pt). Consumption of  $\text{O}_2$  is very fast with Inert wall. In case of RR wall,  $\text{O}_2$  concentration gets smeared out at the core and ignition occurs later than the inert wall. Furthermore, H radical

concentration decreases to 0.1 mol fraction and we don't observe any H radical near the wall. For Pt wall shows the transition from heterogeneous to homogeneous ignition.

RR wall resembles ignition behavior of Inert wall with an additional ignition delay due to its radical recombination effect which supplies reactants back in the reaction mixture instead of forming products. Additionally, the lack of H radical near the surface demonstrates the radical scavenging effect of RR wall. However, as Pt catalytic wall shows the least H radical concentration among these three surfaces, this signifies Pt wall is the strongest radical scavenger among these three different wall materials.

#### **4.4.2 Size effects in a RR-microchannel reactor**

RR wall doesn't behave as a purely catalytic wall but it shows complete quenching of ignition at 997K for 1mm diameter. Therefore to understand the reason of quenching we first studied the effect of reactor dimension with RR wall, the generic surface.

To understand the difference in radical quenching between the catalytic (Pt and Pd) and RR wall, we investigated the size effect (varying channel diameters) for the RR wall in a microreactor. Results varying reactor dimension are shown in Figure 30, where ignition distance is plotted versus reaction temperature for reactor diameters between 1mm and 100  $\mu\text{m}$ .

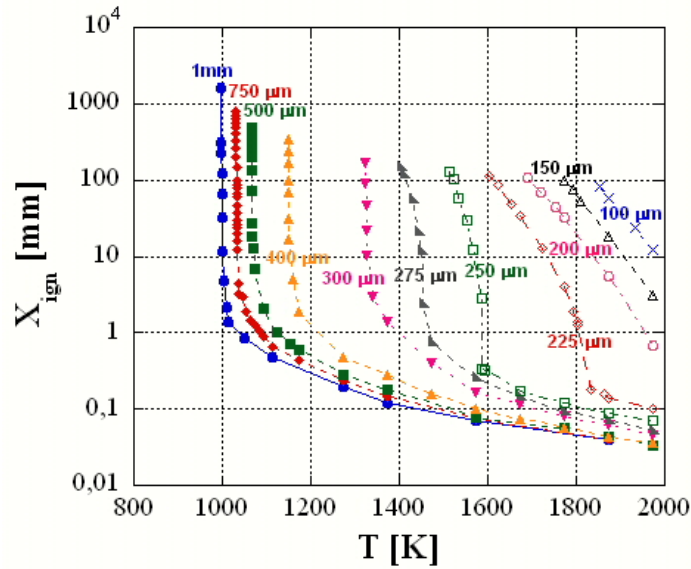


**Figure 30:** Ignition distance versus reaction temperature for a reactor with a "radical recombination" wall varying channel diameters from 1 mm to 100  $\mu\text{m}$ . Stoichiometric  $\text{H}_2$ -air mixture is fed in the microreactor with 9 m/s velocity and at 1 bar pressure.

For all diameters between 1mm to 100  $\mu\text{m}$ , two general effects can be seen. First, with decreasing diameters, the ignition curves shift towards slightly higher temperatures as can be expected from the ignition suppressing effect of the RR wall as discussed before (Figure 28). Interestingly, we also observe a strong shift in the quenching point not only towards higher temperatures, but also towards substantially shorter ignition distances. Quenching distances at quenching points with reduced diameters seem to follow an exponential dependence with diameters.

Since the available surface area of catalytic or non-catalytic materials is a good indicator in assessing the relative significance of surface reactions on overall ignition, it is expected that the general shift in the ignition curves with reduced diameters towards higher ignition delay can be understood by investigating the availability of free surface sites. Figure 31 shows the available free surface sites using 1mm and 250  $\mu\text{m}$  diameters at 1513K with RR wall. The temperature is

chosen as it is in proximity to the quenching point for the 250  $\mu\text{m}$  diameter microchannel so that the expected difference in ignition behavior between larger and smaller diameters should be prominent.

Plot for 1mm diameter shows a distinct minimum within 0.1 mm reactor length and the free surface coverage reaches unity thereafter, while with 250  $\mu\text{m}$  diameter the minimum lies at about 0.3 mm reactor length. The smaller microreactor diameter provides larger surface to volume ratio, hence a larger amount of free surface sites.

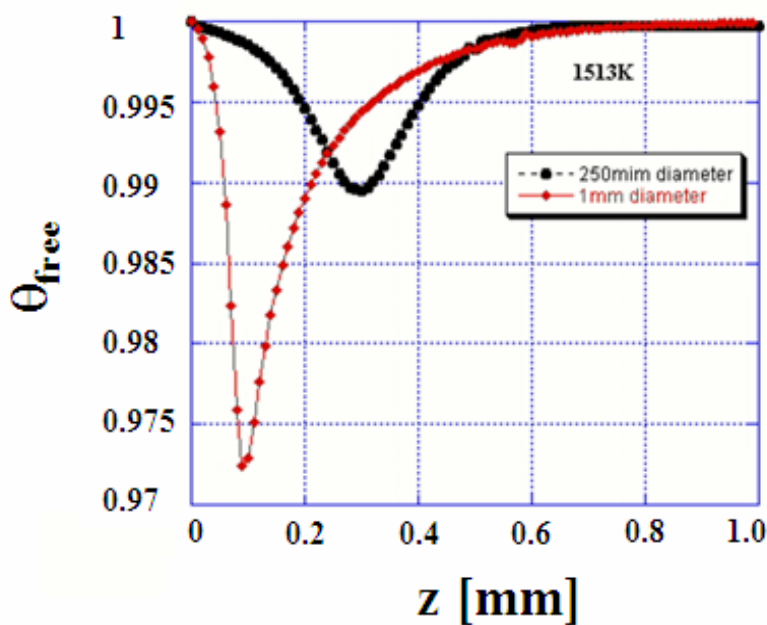


**Figure 31:** Free surface coverage ( $\Theta_{\text{free}}$ ) versus reactor length ( $z$ ) with 1mm and 250 $\mu\text{m}$  reactor diameters at 1513K using RR wall.

The position of the inverted “bell curve” for 250  $\mu\text{m}$  diameter moves further down the axial direction as the large surface area at smaller diameters leads to more recombination reactions which recombines gas phase radicals and keep them available for further gas phase reactions, hence longer ignition delays occur. That effectively accelerates homogeneous reactions and as

homogeneous reaction, having larger activation energy in comparison to surface reaction, preferably occurs at higher temperatures due to Arrhenius-temperature dependency, it pushes the ignition front at higher temperatures. Therefore, with reducing diameters ignition delay increases and curves move toward the higher temperatures.

Regarding the second observation in Figure 30, i.e. the shift in quenching point can be traced back into the kinetics of the “radical recombination surface” and the interplay with homogeneous gas phase kinetics. The shift in quenching point is not a direct effect of the increasing quenching influence of the radical recombination wall with smaller diameters, rather is a superposition effect of the homogeneous reaction rate over heterogeneous reaction rate with increasing reaction temperatures. The dependence of ignition distance and temperature at quenching point as a function of reactor diameter is shown in Figure 32.

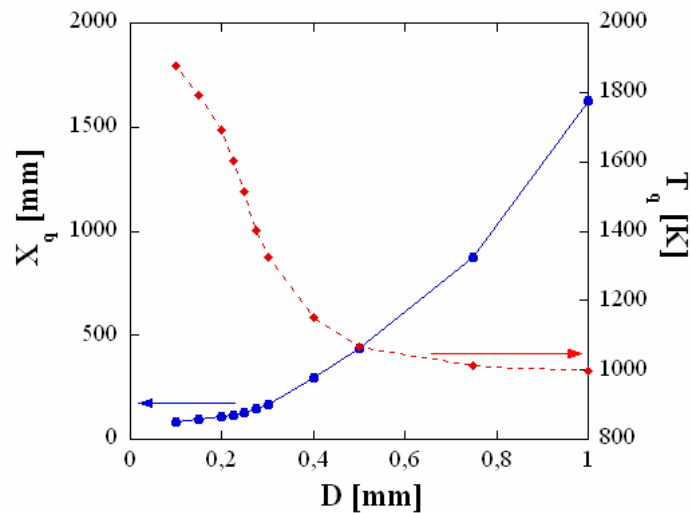


**Figure 32:** Ignition distance (circles, solid line) on the left axis and temperature (diamonds, dashed line) on the right axis at quenching point are plotted vs. reactor diameter in case of RR wall.

Figure 32 confirms that the smaller diameters not only shift the “quenching point” to higher temperatures, but also shifts them to lower ignition delay. As smaller diameters offer higher surface area which results in higher surface recombination reactions, takes over homogeneous reactions faster. On the contrary, adsorption reaction has an inverse dependency with temperature (Langmuir Hinshelwood mechanism) which pushes the ignition to lower temperatures. Here the interplay between homogeneous and surface recombination reactions takes place and the relative dominant effect of faster heterogeneous reactions cancels homogeneous reactions at higher temperatures. This clarifies the fact that RR wall quenches radicals sooner with lowering diameter.

To understand this quicker quenching we investigated the individual gas phase and surface reaction rates for smaller and larger diameters. For this purpose, we calculated the rate of O<sub>2</sub> consumption by gas phase and the formation of O<sub>2</sub> by surface recombination reactions at a fixed temperature with two diameters. Figure 33 plots the total rate of reaction of O<sub>2</sub> in gas phase and on surface along the reactor length for a microreactor of diameter 1mm (in primary axis) and 250 μm (in secondary axis). The temperature is maintained at 1513K as in Figure 31.

Rate of O<sub>2</sub> consumption in gas phase has the opposite sign than the rate of formation of O<sub>2</sub> on surface. Therefore, the absolute value of reaction rate is plotted. Both rates are plotted in terms mol/s to maintain the consistency in the units for gas phase and surface reactions as well.

For 1mm, the rate of O<sub>2</sub> formation by surface reaction is almost negligible (1.93E-9 mol/s), compared to the rate of O<sub>2</sub> consumption in gas phase (2.2E-6 mol/s). Lowering reactor diameter to 250 μm, the rate of surface reaction (7.3E-7 mol/s), becomes comparable to the rate of gas phase reactions (8.5E-7 mol/s). This enhanced surface effect leads to ultimate quenching by

counteracting homogeneous reactions and explains why quenching appears sooner with reduced reactor diameters.

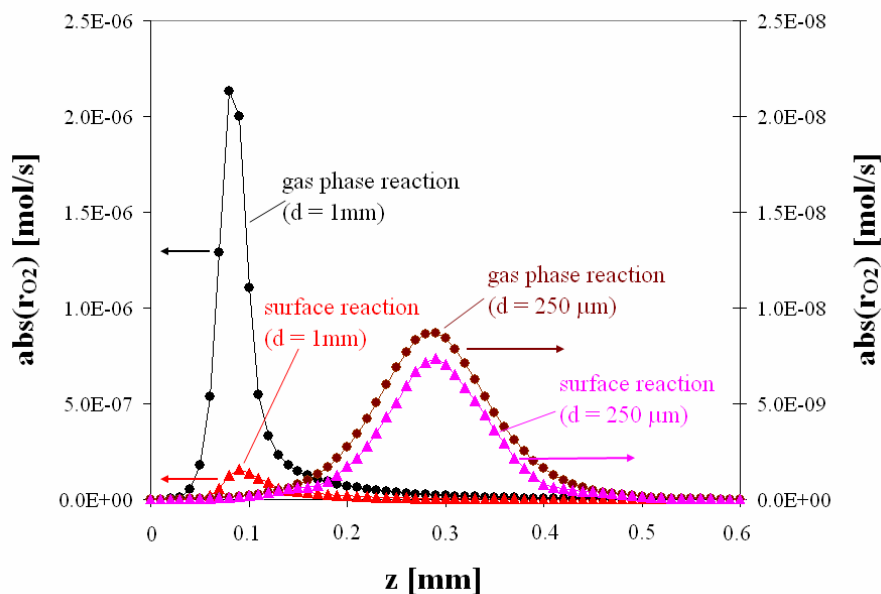


**Figure 33:** Rate of O<sub>2</sub> consumption (circles) and formation (triangles) with 1mm (solid line) and 250 μm (dashed line) diameters at 1513 K versus reactor length (z).

We have so far explained why quenching occurs in microreactor with RR wall and how it behaves with reducing diameters. In addition, we can categorize the plots in Figure 30 into two distinct groups according to diameters. For smaller diameters, i.e. < 300 μm, a significantly different ignition behavior is observed than with larger diameters in Figure 30. Two distinct branches are seen for these lower diameters. For 275, 250 and 225 μm diameters higher and lower reaction temperature branches are observed similar to the case with a catalytic Pt wall. For 200, 150 & 100 μm diameters only the upper branch of the curves is observed in the temperature range below 2000K as the lower temperature branch seem to exceed the range of investigated temperatures. The high temperature branch qualitatively shows the same ignition behavior as that

of diameters larger than 275  $\mu\text{m}$ . A ‘sudden jump’ in ignition distance is noticed in case of 250 and 225  $\mu\text{m}$  diameters with decreasing reaction temperatures. Additionally, while the ignition profiles at higher temperatures run parallel to those with diameters  $> 275 \mu\text{m}$ , ignition profiles at lower temperatures exhibit different slopes with different diameters. The steepness of the low temperature branch decreases with decreasing reactor diameters from 275  $\mu\text{m}$  to 100  $\mu\text{m}$ .

The ‘sudden jump’ in ignition distance in Figure 30 is a result of our definition of ignition (50%  $\text{H}_2$  conversion at the centerline of the reactor) as explained in detail in the following. Figure 34 displays  $\text{H}_2$  concentration (mol fraction) profiles along the reactor length within 3 mm for a microreactor with 1mm diameter at different temperatures.

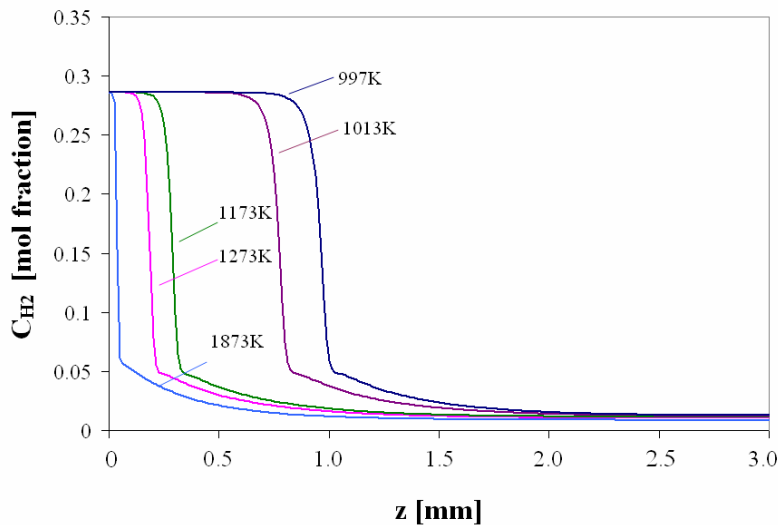


**Figure 34:**  $\text{H}_2$  concentration ( $C_{\text{H}_2}$ ) versus reactor length ( $z$ ) is plotted with 1mm diameter using RR wall.

The curves qualitatively show a similar behavior at all temperatures.  $\text{H}_2$  concentration drops from the initial value to a value close to zero at all temperatures within a short reactor length. The curves show a steep drop which shifts to longer axial distance with decreasing temperatures. This is a result of increased homogeneous ignition delay at lower temperatures. For temperatures

lower than 997K we did not observe any ignition at all. Clearly, at these lower temperatures, the RR wall with 1mm diameter quenches all of the reaction progress.

On the other hand, corresponding progression of H<sub>2</sub> consumption (mol fraction) across the reactor length is shown in Figure 35 for a microreactor with 250 μm diameter at different temperatures. In the left plot the full reactor length of 250 mm is shown. In the right plot, the initial 3 mm of the left plot is shown in detail.

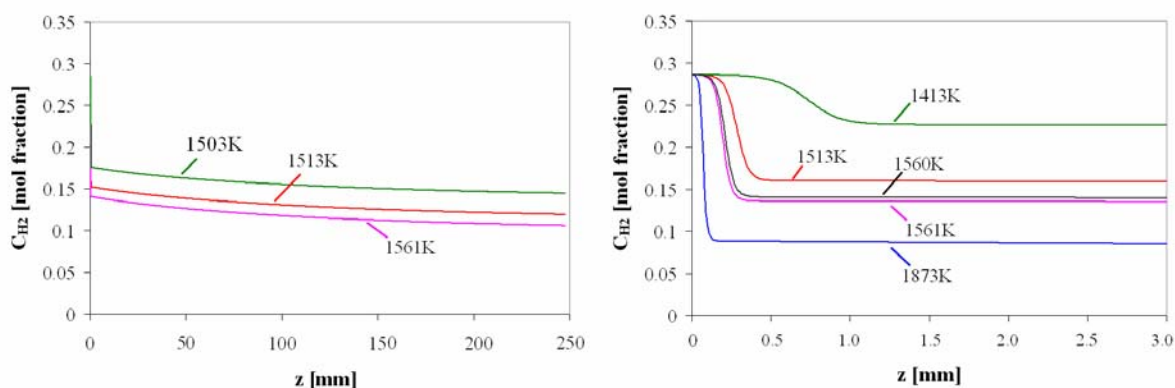


**Figure 35:** H<sub>2</sub> concentration (C<sub>H2</sub>) versus reactor length (z) is plotted using 250 μm diameter with 250 mm (left) and 3 mm axial distances (right) using RR wall.

The curves qualitatively show a different behavior than for a 1mm microreactor (see Figure 34). A steep ignition front is observed within a very short reactor length which is followed by a slow decrease in concentration as shown in the left plot. At high reaction temperatures, the steep front is observed closer to the reactor entrance and with a higher slope. Furthermore, higher conversions are reached at higher reaction temperatures than that at lower temperatures. Complete H<sub>2</sub> conversion is never reached. This can be explained by the fact that after some initial homogeneous conversion –the radical recombination rate on the surface balances any further

conversion and hence leads to a kinetically frozen state of the system far from equilibrium conditions.

In our simulation, ignition distance is defined as the axial point within the reactor where 50% of the inlet  $H_2$  concentration is reached. Since the steep front at higher reaction temperatures is shifted towards the reactor entrance, ignition occurs sooner, as observed in Figure 35. At temperatures above 1561K, ignition (50%  $H_2$  conversion) occurs within the steep front. However, at temperatures below 1561K, 50%  $H_2$  concentration is only crossed in the flat section thereafter. Since the decrease in  $H_2$  concentration in this section is much shallower than in the front section, a slight shift of the curve (i.e. due to a decrease in temperature) results in a strong shift in ignition distance. As a consequence, the low temperature branches of the ignition curve (Figure 30) are much steeper than the high temperature branch.

Thus, while the quenching effect becomes increasingly pronounced with larger surface-to-volume ratios and the ignition curve is therefore shifted towards higher temperatures, these higher temperatures lead to strongly increasing gas phase reaction rates due to the Arrhenius-dependence of the reaction kinetics on temperature. Therefore, when homogeneous reaction events are still possible, this shift in  $X_{ign}$  towards higher temperatures minimizes the strong influence of surface reactions. Hence, the ignition curves from diameter 100  $\mu m$  to 250  $\mu m$  shift to lower temperatures with an increase in slope with increasing diameters. Eventually this trend leads to a vertical line and the low temperature branch finally disappears for large enough diameters, i.e.  $> 300 \mu m$ . Figure 36 confirms this by displaying the transition temperature, i.e. temperatures at the transition point where ignition distance shows a sudden change in slope and the temperatures at quenching point, as a function of diameters.

One can see the transitioning behavior only with diameters  $< 275 \mu\text{m}$  while quenching of ignition is observed over the whole range of diameters studied. Plot shows that transition temperatures for  $100 \mu\text{m}$  diameter is much higher than the quenching temperature and subsequently the difference in those two temperatures gets reduced with increasing diameter and ultimately transition-temperature curve merge with the quenching-temperature curve for diameters  $> 275 \mu\text{m}$ .

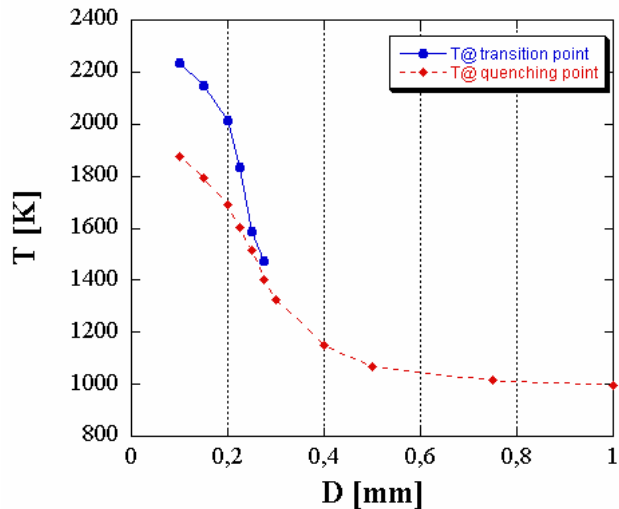


**Figure 36:** Temperatures at transition point (seen with lower diameters) and at quenching point with different reactor diameters with RR wall for a stoichiometric  $\text{H}_2$ -air mixture at 1 bar.

Since lower diameters with larger surface area increases rate of surface reactions dominating gas phase reactions, as a result surface ignition extends the influence on ignition to higher temperatures with  $D < 275 \mu\text{m}$ . Transition point denotes the cross-over from gas phase radical formation to surface recombination reactions. At this point influence of recombination reactions become apparent over gas phase reactions. Extended influence of surface reactions is increased with reducing diameters which moves the transition point towards higher temperature retarding

homogeneous reactions. Therefore, above 300  $\mu\text{m}$  diameter no transition point is observed when the ignition is homogeneously dominated. The temperature at transition point increases with smaller diameters and the maximum transition temperature is resulted in for the smallest diameter studied, i.e. 100  $\mu\text{m}$ . As the occurrence of surface reactions is favorable at lower temperatures, the surface ignition branch traverses to lower temperatures after transition point and at a certain temperature its rate equalizes with gas phase reaction rate where quenching occurs. Hence, temperature at quenching point is always smaller than that at the transition point with all diameters. As diameter increases, surface area decreases and reactor volume increases, gas phase radical formation influences the overall ignition and hence for  $> 300 \mu\text{m}$  diameter, ignition distances with RR wall do not show the lower temperature branch resulting in transition point.

We could explain this ignition behavior with a mathematical expression, fitting the two separate temperature branches for lower diameters. Both branches also fitted with an Arrhenius-type expression, i.e.  $X_{\text{ign}} = A \cdot \exp^{[B/(T-C)]} + D$  like with catalytic wall, where high temperature branches of ignition curves with diameters  $< 275 \mu\text{m}$  show identical dependency with the single branched ignition curves with diameters  $> 275 \mu\text{m}$ . As before (see 4.2.4) A, B, C and D have significant physical meaning where A+D is the critical ignition distance, C is the critical ignition temperature below which ignition does not occur and B/R is the apparent activation energy, where R is the universal gas constant in respective units. The activation energy for the high temperature branch is 201 kJ/mol. It perfectly matches with the activation energy of OH formation in homogeneous kinetics [Appendix A] which is in agreement with the results from the previous calculation in a Pt-microchannel chapter 4.2.4.

On the contrary, for low temperature branch, B value decreases with reducing diameters which designates a declining trend in apparent activation energy. Table 1 shows the calculated activation energy with reduced diameters. This decrease in apparent activation energy with lowering diameters increases the rate of surface reactions.

**Table 1:** Calculated apparent activation energy from the mathematical expression mentioned above for diameters from 250 to 100  $\mu\text{m}$  in case of RR wall.

<b>D [<math>\mu\text{m}</math>]</b>	<b>E<sub>act</sub> [kJ/mol]</b>
250	197.22
225	183.1
200	172.3
150	164.5
100	158.2

In surface reaction rate expression ( $r_s \propto k_{0,s} e^{\frac{-E_a}{RT}} p_s$ ;  $k_{0,s}$  = frequency factor,  $E_a$  = activation energy,  $r_s$  = surface reaction rate)  $-E_a/R$  determines the slope of the reaction rate. As surface reaction rate has an inverse exponential dependence with activation energy, the slope of the surface reaction dominated branch in the ignition curve decreases while activation energy decreases with lowering diameters at isothermal condition. This clarifies the reduction in the steepness of the slope for diameters  $< 275 \mu\text{m}$  in Figure 30. Therefore, we can infer that  $dX_{\text{ign}}/dT$  in Figure 30 is truly determined by the interplay between homogeneous and heterogeneous reaction kinetics.

To understand the governing influence in determining this slope of surface (recombination) reaction dominated branch with decreasing diameters, we studied the individual influence of surface species on the overall ignition. It is clear from the above discussion and observation that

ignition profile for larger diameters is more gas-phase reaction dominated and shows only one branch while with smaller diameters that is influenced by surface recombination reactions which shows two branches. For smaller diameters change in slope in the low temperature branch has been already explained, but the reason behind the drop in activation energy which changes the slope is not yet apparent. Surface diffusion brings radicals together assisting surface recombination. Individual species has different diffusing rates which can influence the overall ignition in an unusual way, it is expected that the study of individual *radical ignition* might take any decisive role in our study to investigate the different behavior in ignition profile with decreasing diameters. It is reported that individual species differently influence the flame stability for a coupled thermal and kinetic quenching [59]. This radical influence [kinetics in Table 10] on overall ignition for 250  $\mu\text{m}$  reactor diameter with RR wall is displayed in Figure 37. The temperature is chosen near the quenching point as the maximum surface reaction rate is observed at that temperature.

A slow consumption of  $\text{H}_2$  is seen in Figure 37 with full RR kinetics. As ignition occurs at 129 mm at axial distance at 1513K (Figure 30) with 250  $\mu\text{m}$  diameter, it is obvious that within 2.5 mm reactor length ignition does not occur with full RR kinetics according to our definition of ignition. Furthermore, ignition occurs faster with adsorption/desorption kinetics of individual H and OH radicals than with  $\text{H}_2\text{O}_2$  and O radicals.  $\text{HO}_2$  radical exhibits negligible influence on  $\text{H}_2$  consumption, so it is not displayed in the above figure. H and OH individual radical kinetics show very similar results to the full kinetics ('full case'). It illustrates that only H or OH radical are largely responsible for the behavior of the RR wall.

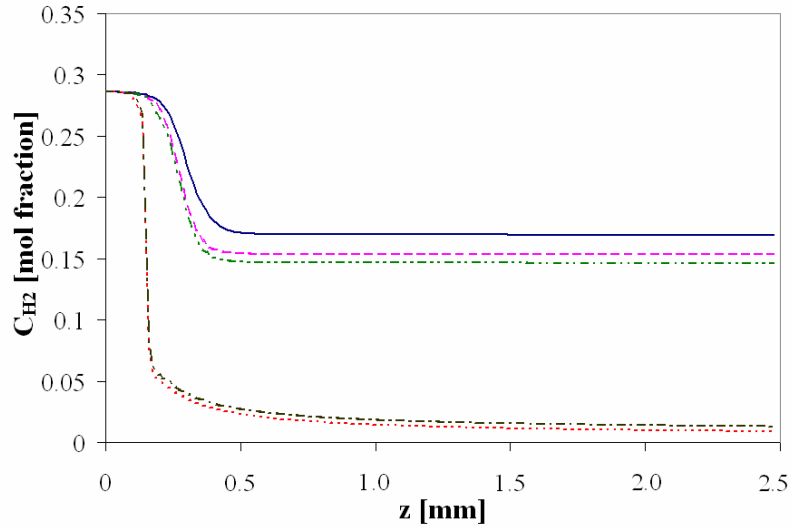


**Figure 37:**  $\text{H}_2$  concentration profile along reactor length for 250  $\mu\text{m}$  diameter with full RR wall kinetics (solid line), kinetics only with H radical containing steps (dashed), kinetics only with OH radical containing steps (dot dot dashed), kinetics only with  $\text{H}_2\text{O}_2$  radical containing steps (dot dashed) and kinetics only with O radical involving steps (dotted). Temperature is kept constant at 1513K.

In contrast, the individual influence of O and  $\text{H}_2\text{O}_2$  radicals on overall ignition is negligible for RR wall. However, among five radicals, H has the most retarding effect for gas phase ignition for the highest availability near surface which is in agreement with results for thermal and kinetic quenching [59]. Slower diffusion of other heavier radicals to the wall reduces the probability in taking part in surface reaction. Though OH and O molecules have similar mass density, the OH retards ignition more than O radical as in our simulation RR surface is seen to be oxygen poisoned. Therefore, radical recombination effect of the surface is more prominent for OH radicals than that of O radicals and OH radical shows higher influence like H radical. Overall this investigation demonstrates the sensitivity of  $\text{H}_2$  oxidation to H and OH radical concentrations.

Further investigation of formation and consumption rate of primary surface species i.e. H, OH and O, are shown with 300 and 250  $\mu\text{m}$  diameters at 1513K in Figure 38, as the change in ignition profile occurred between 300 to 250  $\mu\text{m}$ . With larger diameters rate of consumption and rate of formation of these three surface species are identical. In case of 300  $\mu\text{m}$ , both plots show highest reaction rate for H(S) and rate diminishes subsequently for OH(S) and O(S). The trend is similar for rate of consumption and formation. On the other hand, for 250  $\mu\text{m}$  diameter the rate of consumption of all surface species is much higher while the rate of formation of surface species is a little lower than that of 300  $\mu\text{m}$ . This observation is consistent with our previous explanation (Figure 33) that with reduced diameter, rate of overall surface reactions significantly increase which is reflected in this 3 orders of magnitude increase in consumption rate and 3.5 times decrease in the rate of formation lowering diameter by 50  $\mu\text{m}$ .

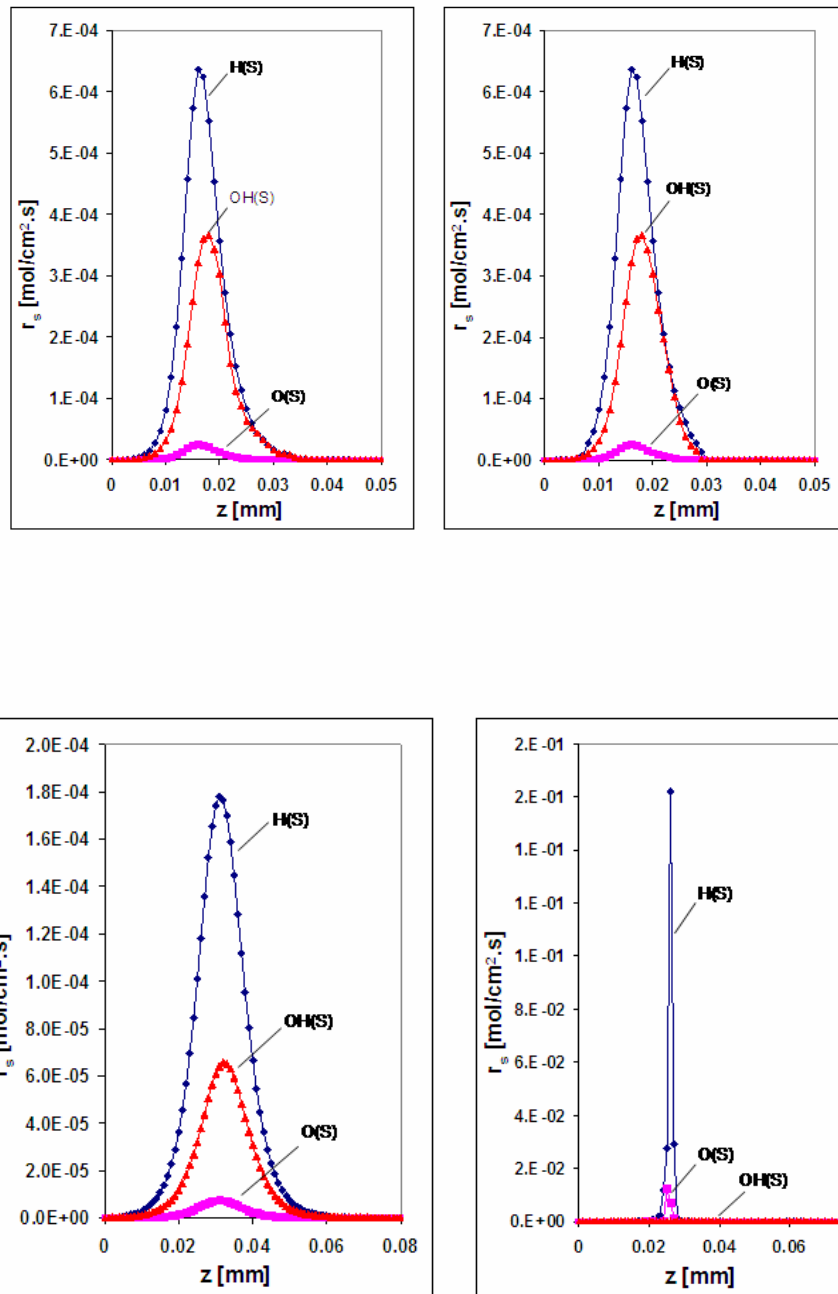


**Figure 38:** Rate of formation (left) and consumption (right) of surface species H, OH, and O at 1513K with 300 μm (top row) and 250 μm diameters in case of RR wall.

In addition to the difference in surface reaction rates between 250  $\mu\text{m}$  and 300  $\mu\text{m}$  diameters, there are two other relevant observations in Figure 38. One is that the magnitude of these two reaction rates (left and right plots in the bottom row) are not identical for 250  $\mu\text{m}$  which illustrates that there are other contributing pathways except H, OH and O formation on the surface which become dominant with 250  $\mu\text{m}$ . Secondly, the rate of OH(S) consumption (in the right plot in the bottom row) is lower than that of O(S) while OH(S) always showed higher reaction rate than O(S) for other three plots in Figure 38. This is due to the switching behavior in consumption rate of OH(S) from 300  $\mu\text{m}$  to 250  $\mu\text{m}$  diameter. That occurs as in RR wall kinetics, activation barrier of OH(S) desorption involving the production of  $\text{H}_2\text{O}_2$  in gas phase [Appendix A] is relatively smaller than all other elementary steps. As a consequence, calculated concentration of  $\text{H}_2\text{O}_2$  is considerably higher with 250  $\mu\text{m}$ , i.e.  $5.6 \times 10^{-7}$  mol fraction than that with 300  $\mu\text{m}$  i.e.  $6.2 \times 10^{-9}$  mol fraction (though this is insignificant in terms of  $\text{H}_2\text{O}_2$  production on catalytic surface). This diverse behavior of OH radical on overall ignition with 300  $\mu\text{m}$  and 250  $\mu\text{m}$  diameters illustrates the reason concerning the difference in ignition behavior for lowering diameters which causes the prominent shift in ignition profile with 250  $\mu\text{m}$ .

It has already been discussed that microreactor with RR wall for reduced diameters shows increasing rate of recombination (surface) reactions and a relative decrease in homogeneous reaction rate cancels those opposing reaction rates at the quenching point. Consequently quenching of  $\text{H}_2$ -air ignition occurs sooner with reduced diameters. The faster quenching with smaller reactor diameters hampers the overall equilibrium conversion which is summarized in Figure 39. This plot shows the overall conversion at 1513K (left axis) and the variation of quenching temperature (right axis) as a function of reactor diameter. From this data one can

calculate the corresponding conversion for any reactor diameter with RR wall which directly evaluates the quenching temperature. The plot shows that a macroscopic reactor with 1mm diameter reaches equilibrium conversion, but the conversion sharply decreases for a microreactor with diameters  $< 0.3\text{mm}$ .

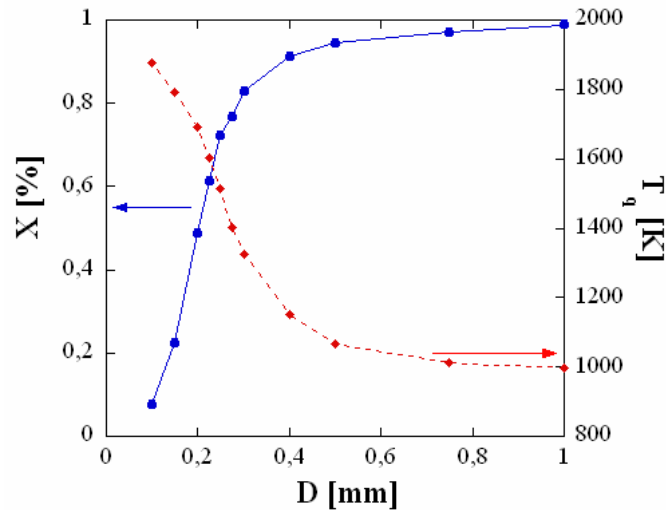


**Figure 39:** Reduction in overall conversion (%) and increase in quenching temperature versus reactor diameter (mm) using RR wall at 1513K.

Therefore, the RR wall which follows a non-equilibrium kinetics pulls the overall reaction away from equilibrium conversion for sufficiently small microchannel diameters and ultimately quenches overall ignition at high enough reaction temperatures. This non-equilibrium kinetics has already been explained in the context of Table 1 and that is a characteristic phenomenon regarding kinetic quenching of ignition in microreactor with RR wall in absence of a thermal feedback of the wall.

## 4.5 ADIABATIC CALCULATION: INERT & Pt WALLS

To decouple the kinetic effect from the thermal effect, we performed isothermal calculation for H<sub>2</sub> oxidation, but in practice all these reactions occur at non-isothermal condition. Though the trend in results is not expected to vary in non-isothermal calculation, but it is likely that high exothermicity of these high temperature catalytic reactions will definitely drag down the ignition influencing parameters to a smaller value. Therefore, to study the influence of temperature gradients on our previous results, we studied ignition properties in case of non-isothermal condition. Initially, the 2D boundary layer model which been used in isothermal calculation is used at adiabatic calculation. However, this boundary layer model poses a major constraint in performing adiabatic calculation. As the linear velocity is high enough for our study, the flow is convection dominant and for isothermal case the boundary layer model is hence justified. On the contrary, for adiabatic case the wall temperature is not constant any more and a high temperature gradient is developed between catalytic wall and the reactor material due to different temperature expansion coefficient. This temperature flux is conducted through the wall to the outer boundary, i.e. reactor materials, which adds up a constant temperature gradient to the inlet flow and results a shift in the ignition profile towards shorter axial length of the reactor. Therefore, a detailed numerical investigation with full Navier Stokes equation coded in commercial CFD (Computational Fluid Dynamics) software Fluent is needed to understand the behavior in detail.

As a first case, Pt coated non-isothermal microreactor with 1 mm diameter is investigated in the following and compared with isothermal operation of same reaction conditions. In isothermal study we studied ignition, as a basic model, in a tubular reactor of 1 mm diameter with purely

homogeneous case (chapter 4.1) where velocity and pressure at inlet subsequently were set to 9 m/s and 1 bar and compared with catalytic materials. Pt wall in that microreactor set-up showed a distinct interaction between homogeneous and heterogeneous reactions (see Figure 6) at 1113K with a fast equilibrium conversion within 5 mm reactor length (see Figure 9). In section 4.2.2 it is seen that for isothermal operation with 1 mm diameter at this temperature equilibrium conversion is reached while strong coupling between two reaction pathways becomes apparent where temperature belongs near to the transition point as shown in Figure 5. Therefore, for a direct comparison with isothermal calculation, this temperature is chosen to study general ignition behavior for adiabatic operation with same diameter. In Figure 40, left plot shows the concentration of major species as reactants, intermediates and products, i.e.  $H_2$ ,  $O_2$ ,  $H$ ,  $O$ ,  $H_2O$ , in primary axis as a function of reactor length, where reaction temperature is plotted in the secondary axis for adiabatic operation in microreactor with Pt wall.

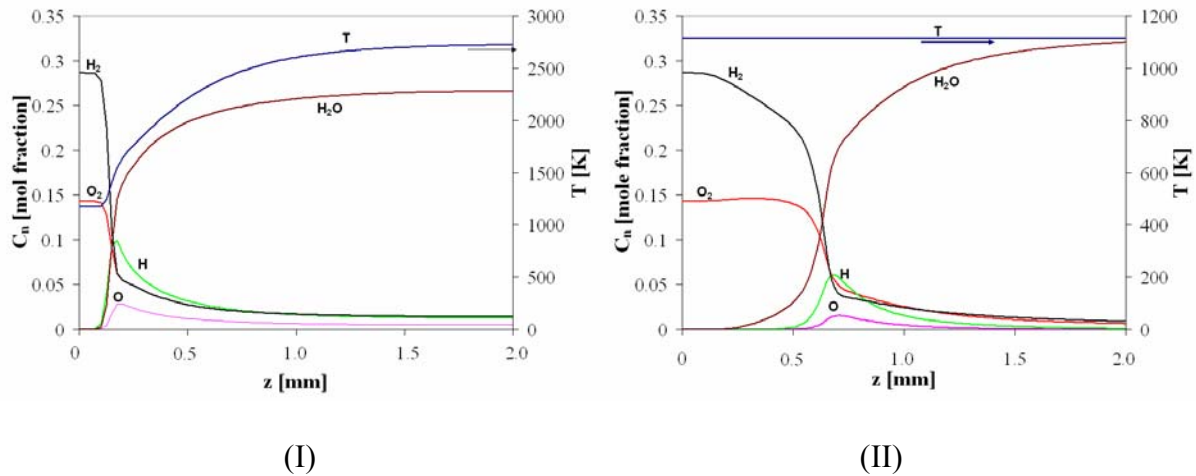


**Figure 40:** Concentration (in mol fraction) of major reactant, intermediate and product species for  $H_2$  oxidation versus axial reactor length (cm) for adiabatic case (left graph) and for isothermal operation (right graph) where temperature profile is plotted in secondary axis.

Right plot exhibits the concentration and temperature profiles at the same conditions for isothermal operation.

In left plot consumption of reactants rapidly takes place within 0.25 mm axial distance while temperature rises up to 2663K within 2 mm due to the high heat of reaction. On the other hand, in the right plot, slower consumption of reactants and higher ignition delay are observed for isothermal ignition with same operating conditions keeping the temperature constant at inlet temperature, i.e. 1113K. This shows that - as expected - due to high temperature rise  $H_2$  oxidation occurs much faster than isothermal ignition. Furthermore, it is seen from the plot that in isothermal condition more water is being produced than that with adiabatic operation. High heat of reaction in adiabatic case increases the activation energy ( $\Delta H = E_f - E_r$ ) which ultimately reduces the surface reaction rate. On the contrary, at 1113K overall ignition is homogeneously dominated indicating larger supply of radicals in gas phase but at this point Pt surface hinders the ignition due to the previously mentioned boundary layer depletion effect which declines the consumption of gas phase radicals leading to a reduction in the product ( $H_2O$ ) formation.

This additional thermal feedback in adiabatic operation is expected to change the ignition behavior in a microchannel reactor for a purely homogeneous case as it supplies more radicals in gas phase than in case of isothermal operation. Investigation of non-isothermal ignition in microreactor as a function of temperature compares the pure homogeneous ignition with a homogeneously dominated branch in a coupled ignition with Pt surface. Figure 41 shows the adiabatic ignition with 1mm reactor diameter for the interaction of purely homogeneous case and the homogeneous-heterogeneous coupled (Pt) case. Inert case shows the asymptotic behavior whereas coupled case shows the similar two branches alike isothermal condition. High temperature branch of coupled case shows higher ignition distance than the inert wall until

1500K until the homogeneous asymptote crosses the coupled ignition profile. Most importantly the transition point for coupled case moves to lower reaction temperature at  $\sim 530\text{K}$  than the isothermal condition. The adiabatic temperature rise for this system calculated from an enthalpy balance is  $\Delta T_{\text{ad}} = 250\text{K}$  for the lower flammability limit (3 vol% of  $\text{H}_2$ ) and  $2336\text{K}$  for stoichiometric  $\text{H}_2$ -air mixture. This temperature hike of  $1600\text{K}$  strongly enhances the homogeneous reactions following Arrhenius expression and which hence becomes faster than heterogeneous reactions.

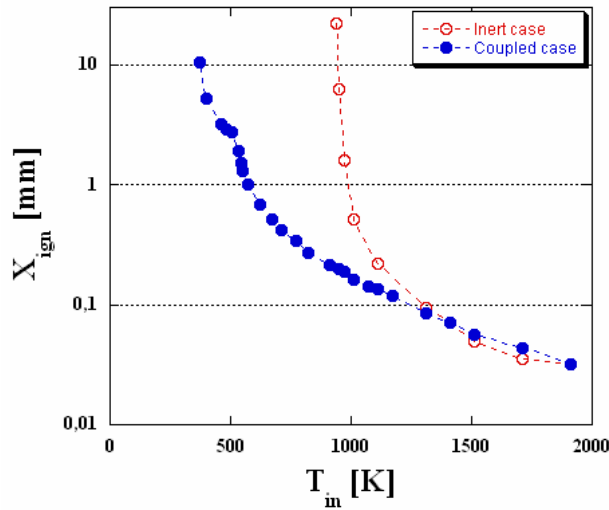


**Figure 41:** Ignition distance versus inlet reaction temperature ( $T_{\text{in}}$ ) for an adiabatic microreactor with 1 mm diameter and inert wall (open circles) and Pt-coated catalytic wall (filled circles).

This brings down the ignition delay for the overall ignition process and ultimately shifts the transition point for adiabatic case to lower temperature than for isothermal operation.

#### 4.5.1 Influence of reactor dimension on quenching – Pt

As in adiabatic calculation with 1mm microreactor diameter the homogeneous reactions controls over heterogeneous ignition until 530K, a question arises regarding the effect of microreactor dimension to suppress this leading homogeneous ignition. From the analogous trend seen in ignition profile [Figure 41], i.e. two branches, complete quenching of homogeneous reactions can be expected with a very small reactor diameter. Therefore we studied the size effect on adiabatic ignition varying diameters from 1 mm to 5  $\mu\text{m}$ . Results are shown in Figure 42.

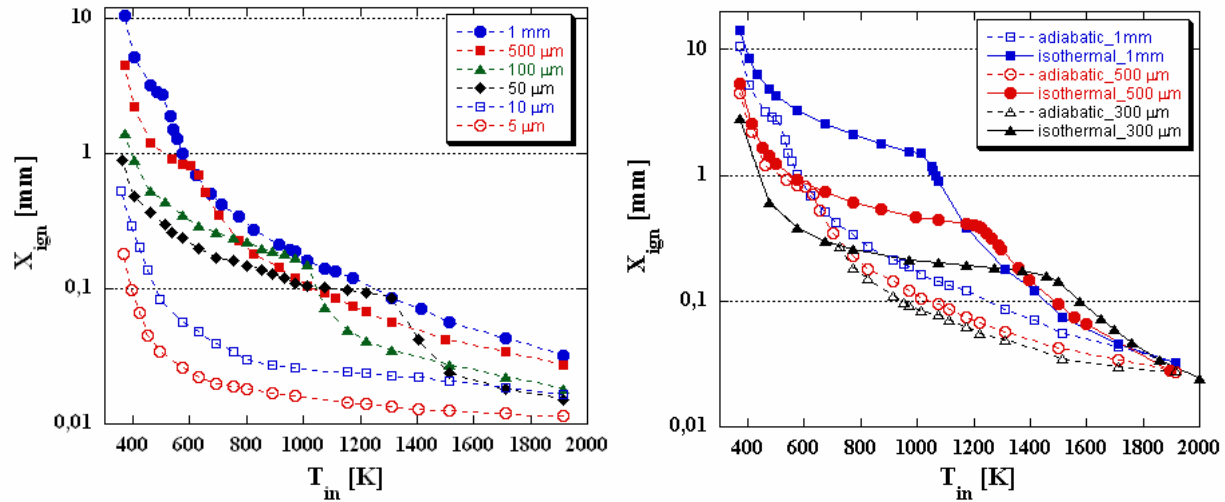


**Figure 42:** Ignition distance versus reaction temperature for an adiabatic reactor with catalytic Pt-wall varying channel diameter from 1 mm to 5  $\mu\text{m}$  (left) and comparing adiabatic (open symbols) and isothermal (filled symbols) operation (right) for 1mm (squares), 500  $\mu\text{m}$  (circles) and 300  $\mu\text{m}$  (triangles).

In the left plot, ignition distance is plotted as a function of inlet reaction temperature for adiabatic condition. A shift to shorter ignition distances is observed with reducing diameters from 1 mm. Additionally, the transition point from catalytic to homogeneous ignition moves to higher reaction temperature. This can be explained by the fact that decreasing diameters shorten

the transport path from the bulk to surface and significantly increase surface area to reactor volume. Both effects lead to an enhancement of the influence of heterogeneous reactions. As a result, catalytic ignition continues for higher temperatures (see also section 4.2.2). This clarifies the shift of transition point to higher temperatures with smaller diameters. How strongly the homogeneous ignition dominates at adiabatic conditions becomes apparent in a comparison with isothermal calculations as shown in the right plot of Figure 42. Isothermal and adiabatic ignition curves are shown for a fixed diameter of 1 mm, 500  $\mu\text{m}$  and 300  $\mu\text{m}$ . For larger diameters ignition distances are smaller for both branches in case of adiabatic calculation than isothermal. This gap reduces with smaller diameters while it diminishes faster in case of heterogeneously dominated branch than for homogeneously dominated branch. Ultimately, with 300  $\mu\text{m}$  diameter the heterogeneous branch exhibits the identical ignition distance for both cases while, homogeneous branch still maintains a distinct gap with isothermal calculation.

The difference in ignition behavior for adiabatic operation than isothermal case occurs mainly due to the temperature increase by the high heat of reaction considered in non-isothermal case when on the contrary high amount heat loss takes place in isothermal condition keeping the temperature constant throughout the entire reaction system. Nonetheless, the qualitatively similar trend, i.e., transition from ignition promoting at low temperature to ignition impeding at high temperature, is observed for adiabatic catalytic microreactor with 1 mm diameter like in isothermal case. To investigate whether high heat of reactions of adiabatic operation directly influences the reaction rate proportionally changing the ignition distance, we calculated the adiabatic ignition distance varying inlet temperature ( $T_{\text{in}}$ ) in comparison to a hypothetical isothermal case, i.e. isothermal ignition distance at temperature of  $T_{\text{in}} + \Delta T_{\text{ad}}$ . If the hypothetical isothermal case shows the parallel dependency with non-isothermal operation, it could be

straight forward to quantitatively calculate the ignition delay for adiabatic operation simply from the isothermal ignition profile only taking temperature rise into account. Therefore, simulations of adiabatic case need not be performed at all.

Results are shown in Figure 43 with 1mm diameter. The transitioning behavior is observed for the true adiabatic ignition but for isothermal ignition only homogeneously dominated branch is seen.

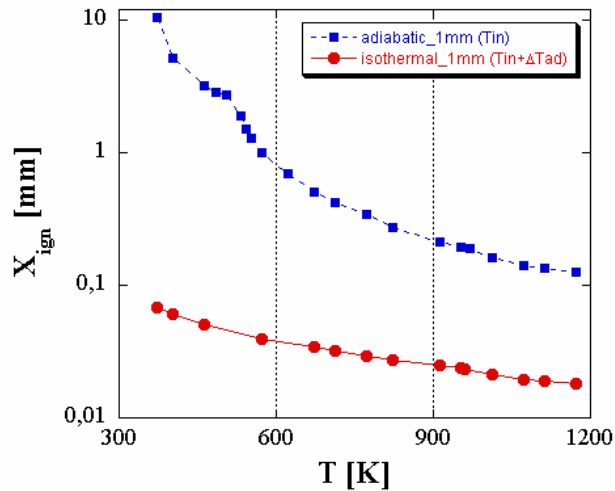


**Figure 43:** Ignition distance versus temperature of a microreactor with 1mm diameter for adiabatic operation varying inlet temperature from 300 to 1200K (squares) and for isothermal operation with inlet temperature added with adiabatic temperature rise for H<sub>2</sub> oxidation system.

Adiabatic temperature rise for H<sub>2</sub> oxidation is 2336K for a stoichiometric mixture of H<sub>2</sub> in air, therefore  $T_{in} + \Delta T_{ad}$  is much higher than  $T_{in}$ . That is why only homogeneous reactions can take place for isothermal ignition at that high temperature and ignition profile is developed with a constant slope. The true adiabatic case leads to a slower release of heat of reaction ( $\Delta H_r$ ) than the hypothetical isothermal case which results in much shorter ignition delay for the hypothetical isothermal case. Therefore, the ignition profile of hypothetical isothermal case can not reproduce the true adiabatic case indicating that ignition behavior counting adiabatic temperature rise in

hypothetical isothermal case does not show a parallel contribution to adiabatic case and at different temperatures adiabatic ignition distance can not be directly predicted from isothermal ignition profile.

We have already seen the size effect on adiabatic ignition in Figure 42 varying reactor dimensions from 1 mm to 5  $\mu\text{m}$  where below 10  $\mu\text{m}$  diameter complete suppression of homogeneously dominated branch is observed. The following concentration contour plots of  $\text{O}_2$ , H radical (Figure 44) and temperature profile of adiabatic ignition for reactor diameters of 1 mm, 300  $\mu\text{m}$  and 5  $\mu\text{m}$  explain the true quenching conditions for adiabatic  $\text{H}_2$  oxidation.

Left graph of first row in Figure 44 shows  $\text{O}_2$  concentration versus axial and radial length with 1mm diameter. Consumption of  $\text{O}_2$  displays a fast ignition within 0.2 mm which mainly occurs due to homogeneous ignition (see ignition curve at 1000K in Figure 43). This dominance of homogeneous reaction on overall ignition is reflected in H radical concentration (0.12 mol fraction) in the middle graph of the same column. As homogeneous reactions follow Arrhenius expression, temperature rise from 1000K to 3000K in bottom graph in left column evidently clarifies the phenomenon where homogeneous reaction takes over catalytic reactions as high temperatures favor homogeneous reactions by enhancing radical chain branching reactions.

The middle column of top row shows the same concentration profiles for a 300  $\mu\text{m}$  channel. One can see faster  $\text{O}_2$  consumption than that with 1mm diameter. A reduced H radical concentration with 300  $\mu\text{m}$  diameter indicates a weakened but still existing homogeneous reaction.

Looking back to Figure 42 it is apparent that at 1000K the ignition curve still lies in the homogeneously dominated branch although closer to the transition point to heterogeneous ignition behavior. Similarly the results also been reflected in temperature profile in the bottom row of the middle column. Temperature increases up to 2800K from 1000K and that temperature

hike is 200K smaller than that with 1mm diameter due to lesser influence of homogeneous reactions than with larger diameter. That also demonstrates the effect of larger surface to volume ratio with smaller diameters which inhibits the dominance of homogeneous reactions.

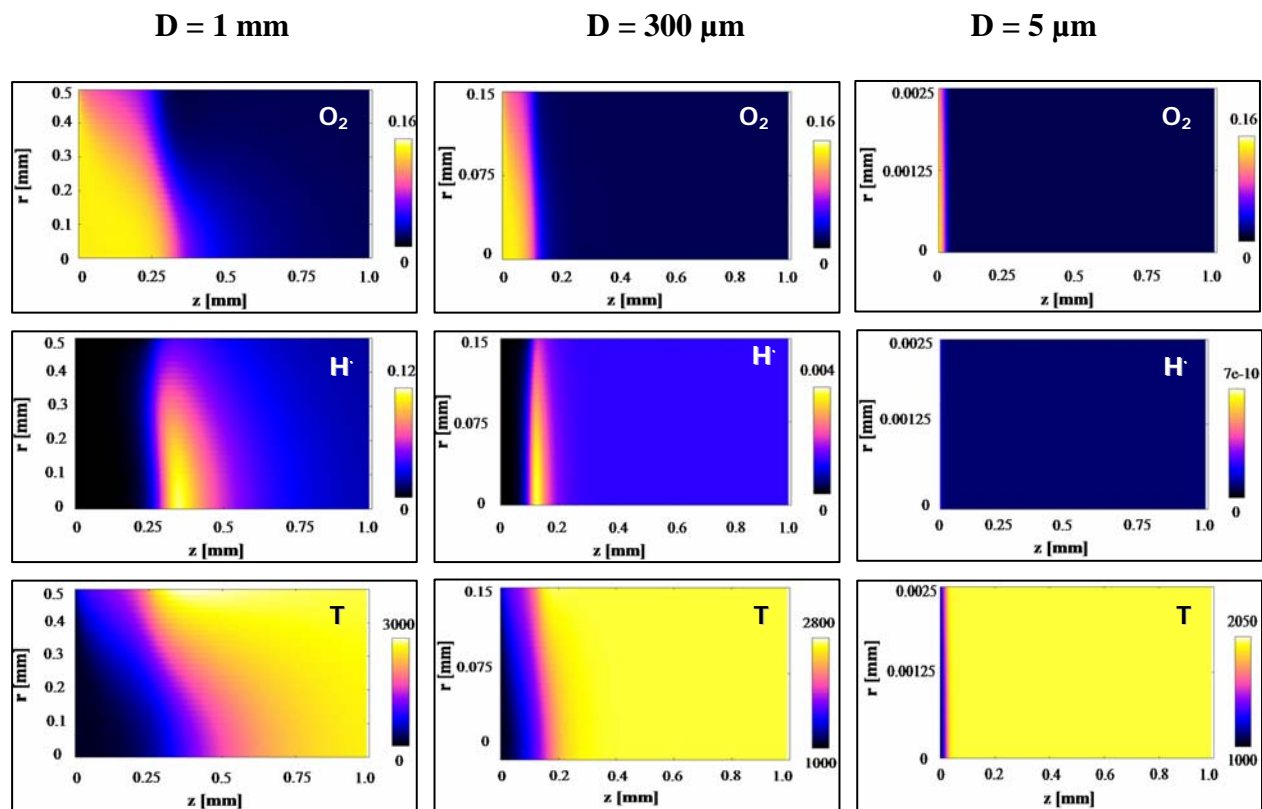


**Figure 44:** Concentration contour plots of  $\text{O}_2$  (top row), H radical (middle row) and temperature profile (bottom row) along axial and radial direction at 993K with 1mm (left column), 300  $\mu\text{m}$  (middle column) and 5  $\mu\text{m}$  (right column) diameters.

Reducing diameter to 5  $\mu\text{m}$ , a very rapid  $\text{O}_2$  consumption is observed within 0.1 mm axial distance in top graph of right column. That total  $\text{O}_2$  conversion is caused only due to the catalytic reactions as reflected in the absence H radical concentration (middle graph of last column). Temperature increases only to 2050K which is much lower than that with larger diameters. Temperature gradient decreases with reduced diameters. The small adiabatic temperature rise

indicates lowering the flammability limits of the explosive gas mixture. This smaller thermal feedback enhances the suppression of homogeneous reactions in addition to the large available surface area for dominant heterogeneous reactions. Finally this result illustrates adiabatic operation in microreactor with 5  $\mu\text{m}$  diameter can extensively quench the extended influence of explosive homogeneous reactions on overall ignition and again the intrinsic reactor safety is clearly observed. The safe reaction zone in catalytic microreactor is much smaller in case of adiabatic operation than that with isothermal case which chooses isothermal operation more favorable for an extended safe reactor operation in handling explosive reaction systems in microchannel reactor.

## **4.6 RELEVANT REACTION SYSTEMS**

### **4.6.1 CO Oxidation: Isothermal Calculations**

Highly efficient conversion of chemical energy to electrical energy can be obtained by Fuel cell technology without emission of environmental pollutants. In fuel cell, the main routes of hydrogen generation i.e. steam reforming, partial oxidation, auto-thermal reforming of hydrocarbon [80-84]. All these routes produce significant amounts of CO as a byproduct with hydrogen and this CO deteriorates the energy efficiency of PEM (polymer electrolyte membrane) fuel cell via CO-induced poisoning of the anode catalyst with a tolerance of  $< 100$  ppm for Pt-Ru electrodes [85]. High temperature required for fuel cells is favorable for producing surface

carbon and high surface coverage which becomes increasingly impossible to remove from the catalyst surface. Therefore it imposes several difficulties in their maintenance and operation making them unsuitable for vehicular and small-scale applications. Therefore, low temperature fuel cells are often studied for commercialization and that is highly sensitive towards impurities like  $\text{CO}_x$ . Hydrogen generated by these conventional methods can be vastly used in low temperature fuel cell only if CO is eliminated prior to its introduction to the cell. Several studies are being performed to reduce CO concentration  $< 10$  ppm in increasing the duration of fuel cells. Choudhury et.al [86] reported CO concentration of  $< 20$  ppm where stepwise steam reforming of methane was used for the production of CO free hydrogen within 648-673K. However, they have noticed a rapid deactivation of the catalyst using this method. Besides that feedstock without carbon [87] has been studied for the elimination of CO in PEM fuel cell and recently preferential oxidation of CO, as an alternative route of reducing CO concentration from  $\text{H}_2$  rich fuels, are studied by various researchers [85, 88, 89]. The competition between CO and  $\text{H}_2$  oxidation was reported in [85] to explain the CO conversion falloff at high temperature. That was contradicted by Choi et.al [89] in their 1D reactor model who showed that net CO conversion drops significantly as the reactor operation changes from isothermal to adiabatic condition with inlet temperature of  $200^\circ\text{C}$  when they ignored the radial heat transfer resistance in their model. Moreover in a recent work by Ouyang et.al [88] has studied the effect of heat transfer limitations on CO preferential oxidation in mini packed bed reactors. They have shown that reverse water gas shift reaction (rWGS) is mainly responsible for thermal gradient causing the drop in CO conversion at high temperatures. They have shown in a theoretical approach that microchannel reactor with catalyst deposited as thin film on the wall can reduce temperature gradient which eliminates rWGS reaction and can reduce the poisoning effect of CO.

In our study, we have already seen catalytic microchannel reactors to behave as an “intrinsically safe” reactor with smaller diameters (see section 4.2.4). If this size effect in catalytic microreactor can suppress undesirable CO oxidation from H<sub>2</sub> oxidation and hence fuel cell can be expected to run without CO poisoning and it can reach 100% energy efficiency by this alternative method. This concept motivated us to study the ignition of CO oxidation in microchannel reactors.

#### **4.6.2 Interaction between homogeneous and heterogeneous reactions**

As we have seen that Pt surface can quench homogeneous reaction in microreactor with 285 μm diameter, it can be expected that larger surface to volume ratio might also quench all homogeneous CO oxidation in catalytic microreactor with a certain diameter. That is why we studied the interplay of homogeneous and heterogeneous reactions of CO oxidation using available kinetics in literature.

Figure 45 shows the purely homogeneous CO ignition with air in the catalytic microreactor of 1 mm diameter. Left plot shows the ignition distance as a function of temperature with the kinetics by Yetter et.al [42] which is shown in Table 11 in Appendix A and the right plot is with GRI mechanism [66] to verify against a widely used reaction mechanism.

Both show the asymptotic behavior at 1250K. Purely homogeneous CO-air stoichiometric mixture shows much longer ignition delays than H<sub>2</sub> oxidation (see section 4.1). The heats of combustion of CO and H<sub>2</sub>, 67.6 and 57.8 kcal/mole respectively [1], but there is almost no reaction path perceptible in the gas phase containing only CO and O<sub>2</sub> that leads to branched chain reactions and explosion as occurs with H<sub>2</sub>-O<sub>2</sub> mixture. Therefore, dry CO-air mixture takes

much longer distances to ignite than H<sub>2</sub>-O<sub>2</sub> mixture. The ignition delay with GRI mechanism is a magnitude higher than with Yetter mechanism.

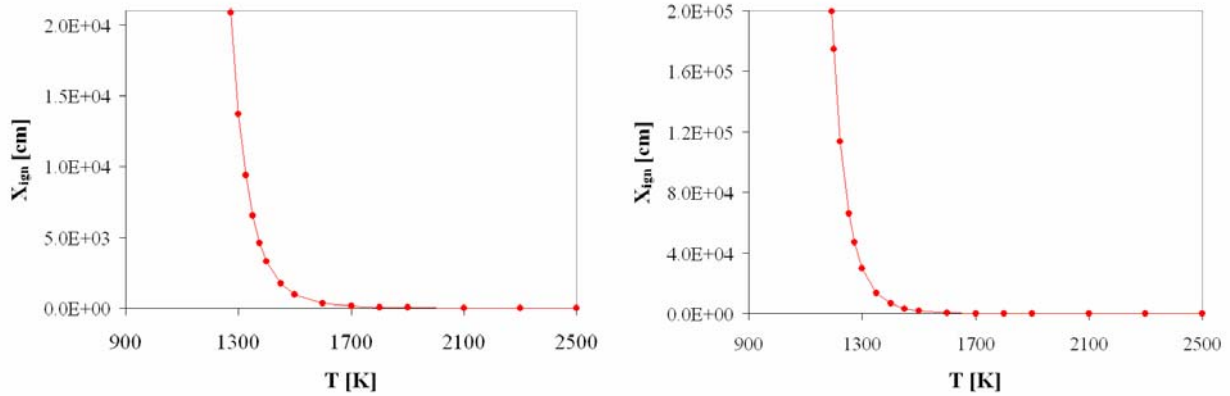


**Figure 45:** Ignition distance vs. reaction temperature in a microreactor for CO oxidation with 1mm diameter and inert wall where left plot is with Yetter et.al kinetics and right plot is with GRI mechanism (Appendix A).

In Yetter mechanism, oxidation of dry CO consists of three elementary reaction steps (reactions 25, 26 and 27 in Table 11) while GRI mechanism contains only one elementary step for CO oxidation with a third body collision, i.e.  $\text{CO} + \text{O} + \text{M} \Rightarrow \text{CO}_2 + \text{M}$ . The calculated reaction rate constant of this CO<sub>2</sub> formation is about three orders of magnitude smaller in case of GRI mechanism, i.e.  $1.7 \cdot 10^{10}$  than that with Yetter mechanism, i.e.  $1.53 \cdot 10^{13}$ . Therefore, GRI mechanism shows much higher ignition delay than the Yetter kinetics. Most importantly, the chain-initiating reaction for CO oxidation, i.e.  $\text{CO} + \text{O}_2 \Rightarrow \text{CO}_2 + \text{O}$  is also absent in GRI mechanism. Henceforth, for the rest of the calculations, Yetter mechanism is chosen to be used as the elementary reactions steps for homogeneous reactions.

As without dilution, CO is expected to ignite faster with pure O<sub>2</sub> than with air and hence it is of interest to look into how ignition behavior varies for CO-O<sub>2</sub> mixture. In Figure 46 left plot shows

the ignition profile of CO and pure O<sub>2</sub> as a range of reaction temperature. It is apparent that ignition continues until 420 K when the feed mixture is composed only with CO and pure O<sub>2</sub> without any diluent, but still with a high enough ignition distances.

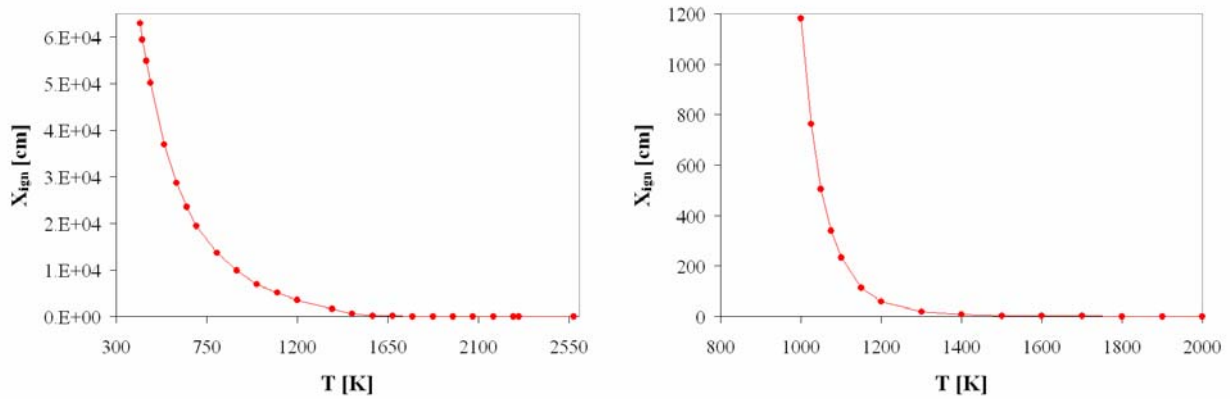


**Figure 46:** Ignition distance vs. reaction temperature in a microreactor for CO oxidation with 1mm diameter and inert wall in case of CO with pure O<sub>2</sub> (left graph) and CO – air mixture with 1.5% OH addition (right plot).

The chain-initiating reaction for CO oxidation is  $\text{CO} + \text{O}_2 \Rightarrow \text{CO}_2 + \text{O}$ . This initiating reaction is hard to achieve without the formation of free radicals and CO - O<sub>2</sub> can only form a small amount of gas phase radicals which leads to branched chain reaction. Therefore, Lewis and von Elbe [1] suggested that the behavior of CO-O<sub>2</sub> system is radically changed by the admixture of small amount of hydrogenous impurities. Therefore, we added 1.5% OH in the CO-air mixture in the feed to accelerate the ignition via the reaction  $\text{OH} + \text{CO} \Rightarrow \text{CO}_2 + \text{H}$  [90]. Right plot in Figure 46 shows the ignition distance as a function of temperature for CO oxidation with OH addition. The previous equation illustrates that CO with OH radical reacts and forms high amount of H radical which is mainly responsible for gas phase chain branching reactions and expedites the

homogeneous reactions. This faster occurrence of homogeneous ignition shortens the ignition delay observed in the right plot in Figure 46.

We have seen that without moisture CO oxidation ignites with a high ignition delay for purely homogeneous case. Therefore, one can expect that the interaction between homogeneous and heterogeneous reactions will not be noticeable in this system. The individual contributions by gas phase and surface reactions on ignition in CO oxidation (CO/air) are shown in Figure 47.

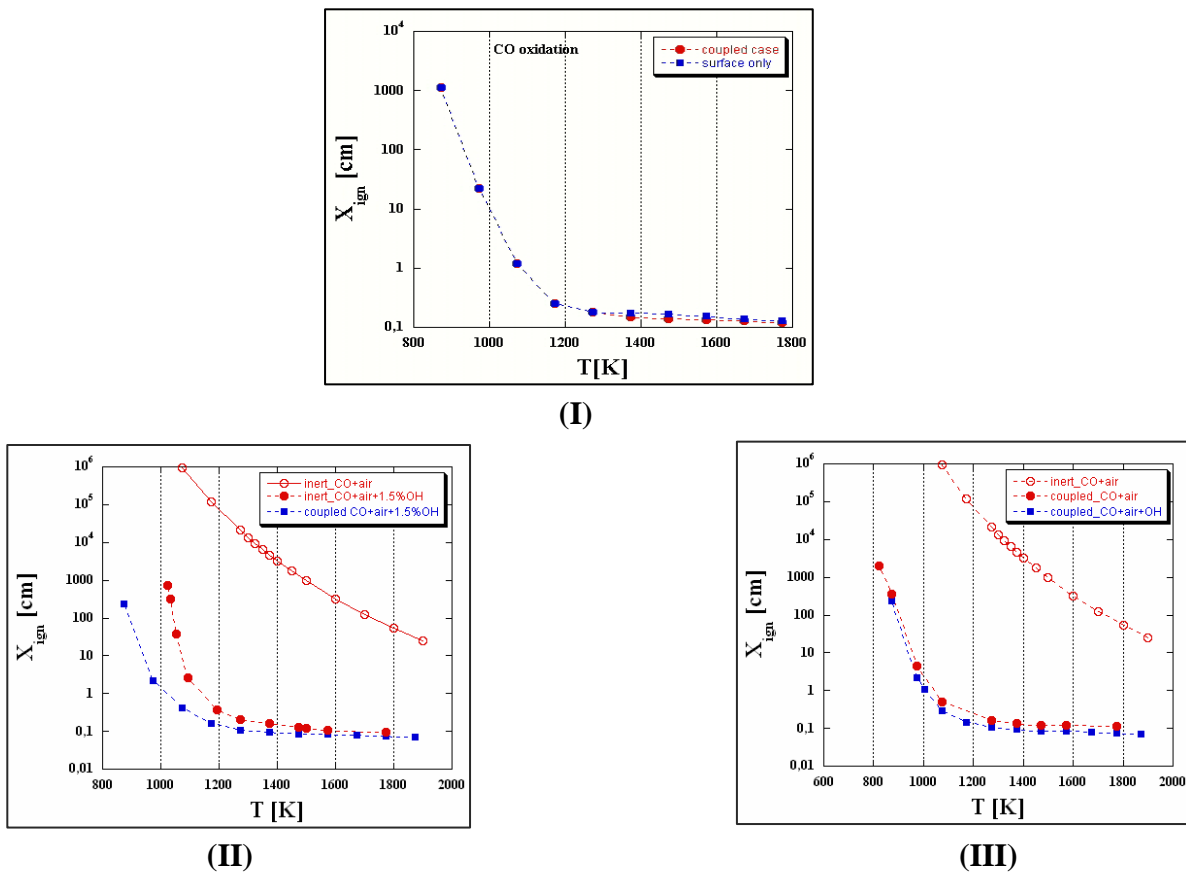


**Figure 47:** Homogeneous – heterogeneous interaction of CO oxidation in terms of ignition distance versus reaction temperature, (I) coupled case (circles) and only heterogeneous ignition (squares); (II) inert wall (open circles), inert wall with OH addition (filled circles), coupled case (squares); (III) inert wall (open circles), coupled case (filled circles), coupled case with OH addition (squares).

The detailed surface kinetics [91] used is tabulated in Table 12. Plot (I) shows that the ignition distance is indistinguishable between coupled case and the purely heterogeneous case. From this plot it is obvious that dry CO-air stoichiometric mixture ignites within 1800K only due to catalytic reactions. Plot (II) demonstrates that the addition of 1.5% OH (concentration in mol fraction) in the feed mixture reduces ignition delay by 3 orders of magnitude for purely homogeneous case. A direct comparison between the ignition profiles of dry CO-air mixture and moist CO-air mixture in plot (II) confirms the fast development of chain-initiation reaction for inert case which explains the faster homogeneous ignition. Finally, plot (III) shows that OH addition leads only to a negligible enhancement of catalytic reactions. It illustrates that CO oxidation in presence of a small amount of hydrogenous impurities only enhances the homogeneous ignition which results in an occurrence of interplay of homogeneous and heterogeneous reactions.

Therefore to test the homogeneous influence on moist CO oxidation, we studied the effect of dimension of microreactor.

#### **4.6.3 Microchannel size effects: CO oxidation**

We have seen that the heterogeneous reactions are not influential at all on homogeneous reactions with 1mm reactor diameter due to the delayed homogeneous ignition. Smaller microreactor dimension at lower temperatures might alter the homogeneous contribution on the overall ignition resulting in the enhancement of the homogeneous-heterogeneous interactions. Hence we have studied the size effect for moist CO oxidation. Results are presented in Figure 48.

Ignition distance of the coupled case is plotted as a function of temperature for 1mm, 500  $\mu\text{m}$  and 300  $\mu\text{m}$  diameters.

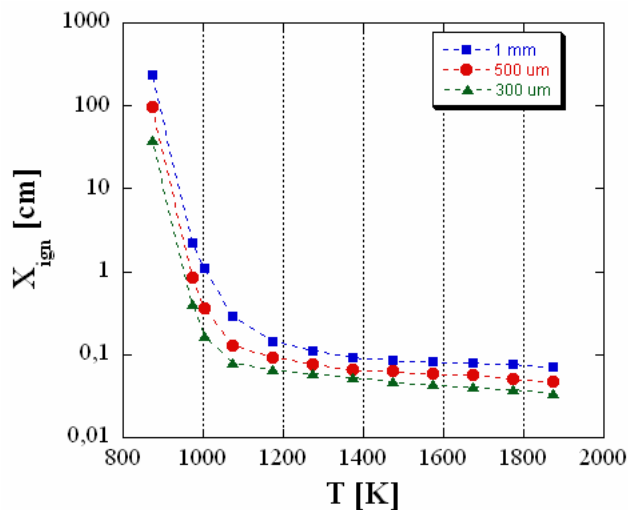


**Figure 48:** Ignition distance versus reaction temperature for 1.5% OH added CO-air reaction mixture with diameters 1mm (filled squares), 500  $\mu\text{m}$  (filled circles) and 300  $\mu\text{m}$  (filled triangles).

Only the single low temperature branch is seen for all diameters. Reducing diameters the ignition distance decreases in parallel with larger diameters. The results indicate that with smaller diameters the interaction between homogeneous-heterogeneous reactions is not increased at all.

This study concludes that CO oxidation, another fundamental subset of hydrocarbon oxidation like hydrogen oxidation, displays minor homogeneous influence on overall ignition behavior unlike  $\text{H}_2$  oxidation does. As a result, no interplay between gas-phase and surface reactions weakens the great potential of catalytic microreactors in terms of its applicability for CO oxidation reaction system. This high homogeneous ignition delay makes the reaction very straightforward where without addition of any hydrogenous impurities, only the surface ignition

plays significant role in catalytic microreactors. Consequently the characteristic dimension of microreactors would not be a plus for dry CO oxidation system unlike hydrogen oxidation to suppress the explosive regime.

As we have seen in section 4.4 that non-catalytic materials show radical quenching of H<sub>2</sub> oxidation for all reactor diameters and also exhibit the interplay between gas-phase and surface recombination reactions (see subsection 4.4.2), this size effect (i.e. faster quenching with reduced diameters) is expected to selectively oxidize CO/air mixture in RR wall even before the explosive H<sub>2</sub>/air mixture ignites. Thus, in another perspective microreactor could behave as a cost-effective system excluding the use of an expensive catalytic material while handling an explosive hydrocarbon oxidation. If smaller diameter with RR wall can ultimately ignites CO/air mixture without hampering H<sub>2</sub> oxidation, microreactors with RR wall can be effectively used for CO - H<sub>2</sub> oxidation. Hence, the ignition of CO oxidation is studied in RR wall.

#### **4.6.4 Microchannel size effects in RR wall: CO-H<sub>2</sub> oxidation**

CO oxidation in inert wall shows much larger ignition delay than that for H<sub>2</sub> oxidation which has been discussed in subsection 4.6.2. CO-H<sub>2</sub> mixture is a well-known constituent in hydrocarbon oxidation. In PEM fuel cell where in-situ H<sub>2</sub> is being converted into electrical energy, presence of CO is undesirable for pursuing the reactions as it is highly poisonous for the anode in the cell. The idea of oxidizing CO before even H<sub>2</sub> oxidation starts in a CO-H<sub>2</sub> gas mixture would be an energy efficient and beneficial approach in terms of the durability of fuel cell application. Non-catalytic material such as quartz glass, represented here by RR wall, shows strong homogeneous ignition with larger diameters most likely the inert wall. For H<sub>2</sub> oxidation, it is observed in

microreactor with RR wall that at a certain temperature the competing gas phase and surface reaction pathways cancels each other that extinguishes overall ignition. In that regard, it would be realistic to look into detail the size effect of RR wall on combined CO – H<sub>2</sub> oxidation reaction system.

In general, the coupling between homogeneous and heterogeneous reactions is absent in RR wall with larger diameter (1 mm) while with reducing diameters mass transport-limit by surface ignition becomes prominent in case of explosive H<sub>2</sub> oxidation reactions. In case of H<sub>2</sub> oxidation, faster quenching of overall ignition is seen in RR wall with 300 μm (see Figure 30) while ignition distance with same diameter in RR wall is plotted for CO – H<sub>2</sub> oxidation in Figure 49. In this plot, large-dashed line with open circles represents the ignition distance of CO oxidation only with air and small-dashed line with open squares corresponds to moist CO oxidation with 1.5% OH added in the feed mixture in microreactor for 300 μm diameter. On other hand H<sub>2</sub> oxidation with 300 μm diameter is represented with small-dashed lines and filled triangles.

In case of H<sub>2</sub> oxidation, ignition occurs with 300 μm diameter inevitably much faster than that with dry CO oxidation with the same diameter as a function of temperature within 1200-2000K. On the other hand, moist CO oxidation shows overall lower ignition distance than dry CO/air mixture but higher ignition delay compared to H<sub>2</sub> oxidation while  $T < 1375\text{K}$  the ignition delay crosses the asymptotic nature of H<sub>2</sub> oxidation ignition profile with 300 μm diameter.

The result indicates H<sub>2</sub> oxidation always occurs before CO oxidation without OH addition. However, the interaction of CO and H<sub>2</sub> oxidation becomes apparent for moist CO oxidation in microchannel reactor with 300 μm diameter for RR wall. At this point, interaction between H<sub>2</sub> oxidation and CO oxidation becomes apparent and CO can be totally oxidized due to the larger

rate of surface recombination reactions with reducing diameters with RR wall even before  $H_2$  oxidation ignites in the reactor.

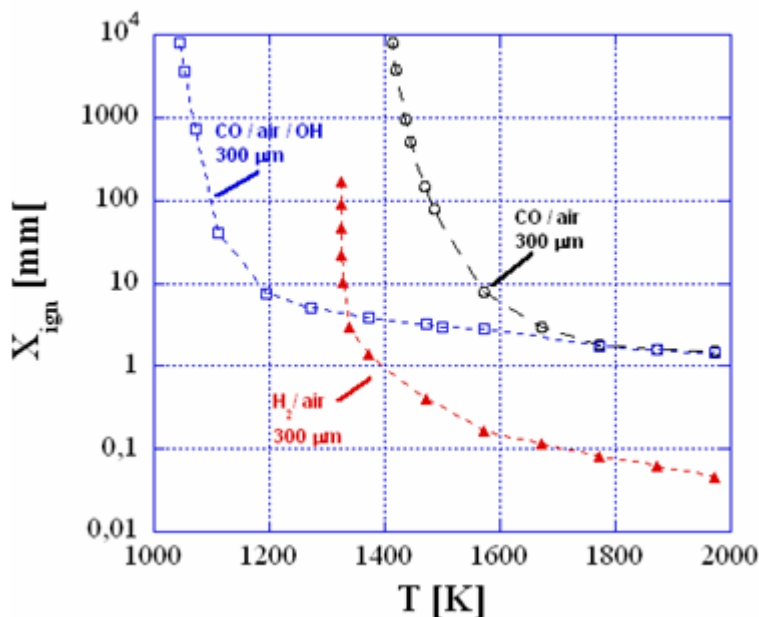


**Figure 49:** Ignition distance versus reaction temperature in case of CO-air oxidation with 300 μm diameter (dashed line, open squares), CO-air oxidation with 1.5% OH addition (solid line, open circles) and in case of  $H_2$  oxidation with 300 μm (dotted line, reverse triangle).

Therefore microreactors can be used to selectively oxidize poisonous CO from the mixture of  $H_2$  and CO which would be beneficial for hydrocarbon oxidation systems by completely converting CO to environmentally benign  $CO_2$  in the mixture. Furthermore, in this microreactor no catalytic materials are needed which improves the applicability of the reaction system and especially develops a cost-effective microreactor. Interestingly, catalytic microreactors here instead of promoting the surface-localized ignition act as an inhibitor of a selective pathway in an explosive reaction mixture and that can be termed as “anti-catalysis”.

#### 4.6.5 NO<sub>x</sub> formation

NO<sub>x</sub>, oxides of nitrogen, i.e. NO, NO<sub>2</sub>, N<sub>2</sub>O, are formed during combustion by several mechanisms e.g. thermal NO<sub>x</sub>, fuel NO<sub>x</sub>, and prompt NO<sub>x</sub>. Thermal NO<sub>x</sub> results from the reaction of nitrogen in air with excess oxygen at elevated temperatures. Fuel NO<sub>x</sub> results in when nitrogen is oxidized by combustion air. Prompt NO<sub>x</sub> is caused by the intermediate formation of hydrogen cyanide (HCN) via chain branching of CH radicals and reacting with N<sub>2</sub> available in the air followed by the oxidation of HCN to nitric oxide. In general, the firing temperature and fuel determines the amount of NO<sub>x</sub> formed.

Nitric oxide (NO) and nitrogen dioxide are present in many high temperature systems in significant quantities. At high temperature, both nitrogen (N<sub>2</sub>) and oxygen (O<sub>2</sub>) are dissociated into atoms that react to form thermal NO<sub>x</sub> by the Zeldovich mechanism [92]



According to Mueller et.al [10, 92] NO is the principal reaction product and reaction (1) is the rate limiting step which has a very high activation energy. The major factors that affect thermal NO<sub>x</sub> production are flame temperature, residence time, the degree of fuel/air mixing, and the concentrations of oxygen and nitrogen in the flame. Higher temperature, longer residence time, and higher oxygen concentration all favor thermal NO<sub>x</sub> formation. Exhaust gases containing > 1000 ppm NO<sub>x</sub> is totally undesirable in terms of a sustainable environment. A significant amount of work has been done over the years in understanding NO<sub>x</sub> formation mechanism in order to reduce emissions [1, 42, 73, 93-95] suggested in their work that a small amount of

nitrogen oxides can significantly influence the fuel oxidation characteristics. While literature says formation of NO generally is favored by higher temperature, i.e. 1803K-2573K, Glarborg et.al [95] says that even at 600K, NO may act to promote fuel oxidation, though they mentioned that low temperature mechanism is not well understood yet.

To justify whether our previous ignition studies are influenced with the nitrogen oxide concentration while nitrogen containing species considered in the kinetics, we verified the validity of “intrinsic reactor safety” in microreactor for H<sub>2</sub> oxidation system in the context of NO<sub>x</sub> formation. Purely homogeneous case produces larger amount of thermal NO<sub>x</sub> than that with coupled case (with Pt surface) at the high temperature, ranging from 1803K-2273K [92]. In this work, we studied NO<sub>x</sub> formation in case of H<sub>2</sub> oxidation in air in microreactor for a purely homogeneous case and the gas-phase kinetics is used from detailed GRI mechanism [66]. This detailed kinetics consists of 53 species and 328 reactions including elementary reactions of NO<sub>x</sub> formation. Furthermore, NH<sub>3</sub> oxidized on Pt is taken into account according to Andrae et.al [73] and we add an NH<sub>3</sub> subset in the Pt surface kinetics (Table 13 in Appendix A). Only thermal NO<sub>x</sub> is considered for our study. Gases are fed with 9 m/s velocity at atmospheric pressure in microreactor for isothermal operation.

Figure 50 elucidates the comparison of formation of nitric oxide in microreactor with 1 mm diameter between the purely homogeneous case and the coupled case. Left plot exhibits the concentration of NO by homogeneous ignition along the reactor length as a function of temperature. For all temperatures ranging from 1803K to 2273K, concentration increases and almost reaches a constant value thereafter within this reactor length. It is apparent from the plot that the NO formation within 3 mm axial distance steeply increases with the increase in temperatures. The maximum concentration lies within  $9 \times 10^{-4}$  mol fraction with the highest

temperature studied (2273K) for the purely homogeneous case. The NO formation increases with temperature in case of a purely homogeneous wall as stated in [95].

On the contrary, for the coupled case in the right plot, a steep increase followed by an immediate drop in NO concentration is observed within 1.8 mm for the entire temperature range. Furthermore, after the reduction in concentration these plots also reach a constant value almost at the same axial distance. The maximum concentration of NO is one order of magnitude smaller than that with purely homogeneous case. In left plot, the overall increase in NO formation from 1803K to 2273K is relatively higher than that in coupled case which designates the absolute increase in NO<sub>x</sub> formation is more with purely homogeneous case than with coupled case.

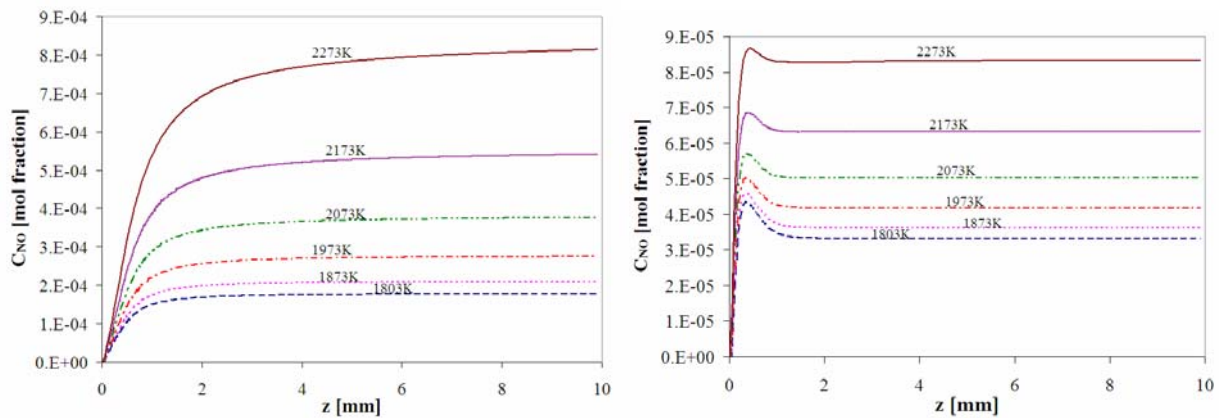


**Figure 50:** Concentration of nitric oxide ( $C_{NO}$ ) versus reactor length ( $z$ ) varying with reaction temperature from 1803K to 2273K in case of purely homogeneous case (left plot) and for the coupled case (right plot).  $H_2$ -air mixture with nitrogenous species is fed in microreactor with 1 mm diameter and at 1 bar pressure while inlet velocity is set to 9 m/s.

The consequent increase and decrease of NO concentration in coupled case can be explained in a way that at these higher temperatures the probable homogeneous reactions occur before the onset of heterogeneous reactions where surface reactions are unfavorable for NO<sub>x</sub> formation. This homogeneous reaction causes the peak in NO concentration and the subsequent dominance of

surface reactions reduces the formation of NO resulting in the drop in the plots. Nevertheless, the overall concentration of produced NO for both the cases is negligible in terms of emission abatement issues in preserving the environment clean and the previously calculated intrinsic reactor safety will not be hampered with such an insignificant amount of thermal NO<sub>x</sub> formation. Low temperatures also might influence gas phase radicals in forming nitric oxide as discussed by Glarborg et.al [95]. This instigates to test NO<sub>x</sub> formation at lower temperatures at 600K for both the cases. In addition to that, it is obvious investigating the influence of reactor dimensions in microreactor on the NO<sub>x</sub> formation as at lower temperatures role of surface ignition becomes significant and smaller dimension of reactor accelerates the surface ignition (see subsection 4.2.2). Therefore, to see whether smaller diameters ultimately terminate the production of nitrogen oxide at lower temperature, the size effect is studied in microreactor with Pt surface in terms of NO<sub>x</sub> formation. Figure 51 shows the development of NO concentration as a function of axial distance varying reactor diameters from 1mm to 300 μm at 600K.

For all of these three diameters used in this study, we clearly can observe an increase and then a subsequent decrease what we have previously explained in the right plot of Figure 50. With 1 mm diameter, the hump in the concentration profile is much distinct while with lowering diameters to 300 μm that sharpness almost disappears. The decrease in NO concentration decreases after ~ 1 mm with all three diameters studied and reaches a steady value thereafter.

Larger diameter with higher reactor volume more influences homogeneous reactions and as a result NO formation increases which ultimately reaches a maximum of 4.3E-7 mol fraction. Reducing diameters, surface area increases and dominance of heterogeneous reactions takes lead over gas-phase reactions

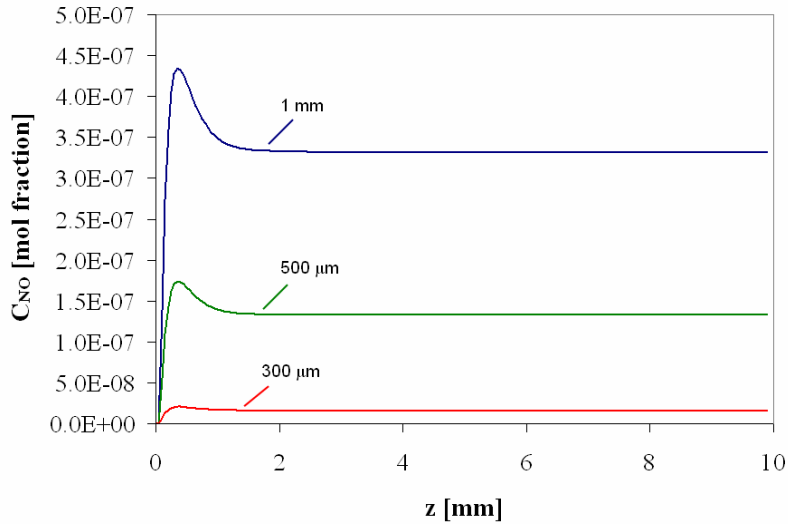


**Figure 51:** Concentration of NO versus reactor length ( $z$ ) with 1 mm, 500  $\mu\text{m}$  and 300  $\mu\text{m}$  reactor diameters at 600K temperature.  $\text{H}_2$ -air is fed in a Pt-coated microreactor at the same inlet conditions.

Dominant surface reactions consume gas phase radicals faster and hinder the gas-phase reactions (see subsection 4.2.1), that results a reduction in the NO concentration with 500  $\mu\text{m}$  diameter and correspondingly a decrease by two orders of magnitude is observed with 300  $\mu\text{m}$  diameter. This higher influence of surface reaction also shortens the drop-off length with lowering diameters after the maximum concentration in Figure 51. All these results demonstrate that  $\text{NO}_x$  formation is virtually negligible with smaller diameters in microreactor especially at low temperatures in the heterogeneously dominated regime.

Some of the implications of mass transport control become very much apparent in  $\text{H}_2$  oxidation with NO formation in gas phase. For all lean mixtures the composition near the wall is lean while for rich mixtures is rich. The ignition by wall during the mass transport control is sensitive to the bulk fuel/air ratio [10]. It is known from the literature that lean fuel-oxygen mixture is favorable for reducing  $\text{NO}_x$  formation [95]. Therefore, we briefly studied the influence of equivalence

ratio ( $\phi$ ) on NO<sub>x</sub> formation in the microreactor for a purely homogeneous case with 1 mm reactor diameter compared to 500  $\mu\text{m}$  at 1803K, i.e. the lowest temperature for NO formation in gas phase and the results are shown in Figure 52. We have already seen (Figure 50) that NO forms more in gas-phase compared to the coupled case and hence effect of equivalence ratio is studied for an inert wall.

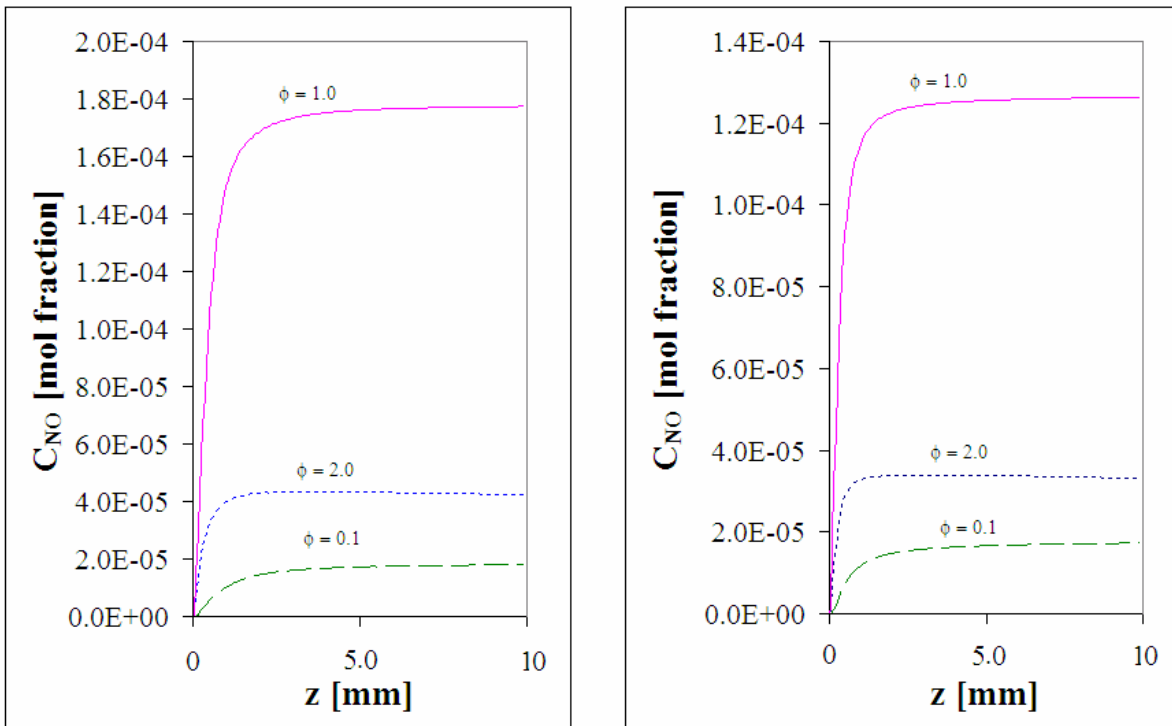


**Figure 52:** Concentration of NO ( $C_{NO}$ ) along the reactor length ( $z$ ) at 1803K with H<sub>2</sub>/air equivalence ratio of 0.1 (dashed line), 1.0 (solid line) and 2.0 (dotted line) with 1 mm (left graph) and 500  $\mu\text{m}$  (right graph) diameters. This is for purely homogeneous ignition.

In this plot it is evident that for both diameters concentration of NO shows the maximum with stoichiometric mixture. At 1803K, NO<sub>x</sub> formation is higher for both diameters what we have seen in the left plot of Figure 50. Interestingly for the fuel lean mixture ( $\phi = 0.1$ ) NO<sub>x</sub> formation

shows the minimum which is obvious due to the depletion of fuel, there is less amount of gas phase radicals for the chain branching reactions which accelerate the NO<sub>x</sub> formation. On the contrary, NO formation for  $\phi = 2.0$  belongs in between lean and stoichiometric mixture for both diameters and this needs to be looked into detail.

In this chapter, NO<sub>x</sub> formation is investigated while oxidizing H<sub>2</sub> – air mixture in microchannel reactor keeping same inlet conditions as with H<sub>2</sub> oxidation reactions. NO<sub>x</sub> emission is a major issue for high temperature catalysis with regards to a sustainable environment. The concentration of NO<sub>x</sub> developed in Pt coated microreactor is negligible with all diameters studied while stoichiometric H<sub>2</sub>-air mixture in purely homogeneous case shows higher concentration than that with catalytic reactions. Overall small amount of NO<sub>x</sub> formed does not alter the ‘intrinsic reactor safety’ in carrying out explosive H<sub>2</sub> oxidation in catalytic microchannel reactors.

## 5.0 SUMMARY

The ignition behavior of H<sub>2</sub> oxidation with air was studied in a microchannel reactor via numerical simulations with a two-dimensional boundary-layer model coupled with detailed reaction kinetics. Detailed elementary-step kinetics both for surface reactions as well as homogeneous gas phase reactions were used in the simulations and other parameters were chosen in agreement with previous experimental studies of this system. Influence of catalytic and non-catalytic materials on the overall ignition were investigated. Platinum was selected as a well-studied, typical noble-metal oxidation catalyst. In addition to that, another industrially significant catalyst for oxidative high temperature reactions, palladium was also investigated. Additionally a (hypothetical) ‘radical recombination wall’ was taken to represent a group of wall materials such as quartz-glass or silicon, which are known to be catalytically virtually inactive, but still can act as rather efficient radical scavengers. An inert wall case served as the reference case of an “un-hampered” homogeneous gas phase reaction.

Strong wall effects were found for both types of chemically active wall materials. However, while the radical recombination wall only showed an ignition-hampering effect, the catalytic walls showed a transition from an ignition-delaying effect at high reaction temperatures to an ignition-promoting influence at lower reaction temperatures. Most significantly, all wall materials could completely suppress homogeneous ignition for a range of reaction parameters. This is due to the competing rates between radical recombination by surface and radical formation by gas phase in case of the radical recombination wall where ultimately the dominance of radical recombination (surface) reactions completely suppresses any reaction in the system.

The surface recombines gas phase radicals and gradually retards forward radical forming reactions, ultimately quenches homogeneous ignition. In contrast, for the catalytic surface this effect can be explained with a true radical quenching mechanism by the catalytic surface on the bulk gas phase. Therefore, while the homogeneous reaction (and thus particularly flames and explosions) can be suppressed in a catalytic microreactor, the overall conversion of the reactants into products is still taking place on the catalytic surface and the range of reactive conditions is even substantially increased in comparison to purely homogeneous reactions (as well known from catalytic combustion studies).

The simulation results were in good qualitative agreement with the results from previous experimental and theoretical investigations of this reaction system. Particularly the complete suppression of the homogeneous reaction in the transition from a 500  $\mu\text{m}$  channel diameter to a 100  $\mu\text{m}$  diameter for the catalytic platinum surface qualitatively is in good agreement with the studies. This result of ‘size-effect’ pinpoints again one of the most interesting aspects of catalytic microreactors: due to the very large surface-to-volume ratio that can be realized in these systems, they can be manufactured to be *intrinsically* safe for highly explosive and dangerous reactions.

Reaction pressure is also an important parameter regarding reactor safety. Studying the effect of pressure into detail we found that the ignition behavior is determined by an intricate interplay between homogeneous and heterogeneous reactions and diffusion transport. While increasing pressure slows diffusion, it accelerates the overall heterogeneous surface reaction and leads to an even more pronounced acceleration of homogeneous gas phase reactions. Therefore, an acceleration of ignition with increasing pressure was observed for high reaction temperatures ( $T > 1200\text{-}1500\text{ K}$ ), and an increased ignition delay for low reaction temperatures ( $T < 1200\text{ K}$ ).

After investigating size-effect and pressure-effect on overall ignition, a mathematical fit of critical ignition distance as a function of pressure and reactor diameter allowed us to precisely calculate the critical diameter and pressure for the H<sub>2</sub> oxidation reaction system. This calculation yields that 285 μm is the critical diameter at ambient conditions for Pt surface, and 9.7 bar as the critical pressure below which there is no reasonable reactor diameter to obtain the reactor safety. For Pd, these critical values are 125 μm as critical diameter and 3.8 bar as the critical reaction pressure.

The ignition delay was furthermore found to increase with increasing fuel-to-air ratio (i.e. equivalence ratio  $\phi$ ). While  $\phi$  was found to have a rather weak influence on the homogeneously dominated ignition at higher temperatures, an increasing hydrogen poisoning of the catalyst surface at lower temperatures leads to a pronounced increase in ignition distance at lower reaction temperatures.

Furthermore, air is found to be the safer oxidant for H<sub>2</sub>-oxidation than pure O<sub>2</sub>, as the presence of diluent decreases the concentration of the reactants which helps to quench homogeneous ignition.

While the results of this simulation study will quantitatively only be valid for the specific system studied (i.e. hydrogen oxidation over platinum, palladium and a strict “radical recombination surface”), it can be expected that qualitatively similar quenching effect should be observable for a wide range of similar catalytic and non-catalytic materials as well as for many chemically similar reaction systems, in particular for the oxidation of simple hydrocarbons for which the H<sub>2</sub> oxidation reactions form a sub-set of the complete reaction scheme.

Most importantly, our results indicate that increasing pressure leads to reduced quenching of homogeneous reactions by surface reactions, and hence the observed intrinsic safety in

microchannel reactors [2, 11, 13] can not be taken for granted any more and needs to be re-evaluated for specific cases.

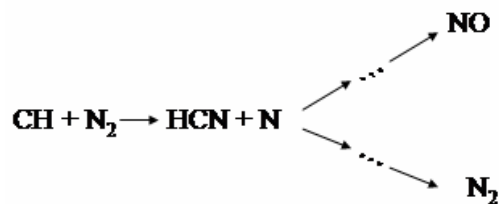
## 6.0 OUTLOOK

### 6.1 POSSIBLE APPLICATIONS TO OTHER REACTIONS

The results of this simulation study will of course quantitatively only be valid for the specific reaction system studied (i.e. hydrogen oxidation over platinum, palladium and a strict radical recombination surface), it can be expected that qualitatively similar quenching effect should be observable for a wide range of similar catalytic and non-catalytic materials as well as for other high temperature catalytic reactions. Preferential CO oxidation has been studied here to evaluate the applicability of safe reactor operation in microchannel reactor by selectively oxidizing CO from the CO-H<sub>2</sub> gas mixture while CO acts as a poison for PEM fuel cell. Instead of different well-known methods applied for preferential CO oxidation, i.e. removal of reverse water-gas shift reaction, use of various catalysts for enhancing selectivity etc., we carried out CO oxidation in microreactor as an alternative avenue. Nonetheless, due to faster catalytic reaction of CO on Pt surface no interaction of homogeneous and heterogeneous reactions are observed which makes the system uninteresting to look at. On the contrary, the system indicated a delayed ignition than H<sub>2</sub> oxidation in RR wall while adding moisture in it and possibly opens up a new avenue for quenching CO ignition even before H<sub>2</sub> ignition sets in. This study can also be applied for water-gas shift reactions in the similar way for CO removal from the mixture.

Radical quenching effect in microreactor also can be applied for higher hydrocarbon oxidation when NO<sub>x</sub> formation poses a crucial problem in terms pollution abatement. Prompt NO<sub>x</sub> occurs

through radical chain branching when CH radicals react with N<sub>2</sub> and forms NO<sub>x</sub> through the following reaction mechanism:



Therefore, if microreactor can effectively quench CH radical formation in gas phase no nitric oxide will be formed in the gas phase and microreactor will hold a great potential in terms of environmental abatement. Hence, we also studied NO<sub>x</sub> formation for hydrogen oxidation in microchannel reactor which results in a negligible amount of nitrogen oxides re-addressing the reactor safety.

The exploitation of natural gas (i.e. methane, ethane, higher hydrocarbons) is gaining increased attention in recent years. Efficient strategies for the use of natural gas is under ongoing researches by several groups in academia and industry as well. Among three major one-step process to form syn gas from methane, one efficient method is partial oxidation. Total oxidation of methane is detrimental for syn gas production due to highly explosive nature ( $\Delta H_r = -800$  kJ/mol). It would be beneficial in terms of conversion if the total oxidation can be quenched from the system and that problem possibly can be resolved in catalytic microreactors with its *radical quenching* concept running the safe reactor operation.

A catalytic microreactor, to investigate the reactor safety with our calculated reactor conditions and configuration for hydrogen oxidation system, is currently under fabrication in our group. Following is the designed microreactor for further experimental evaluation of numerical results.

## 6.2 DESIGN & FABRICATION OF A MICROREACTOR

Microchannel of depth  $250\ \mu\text{m}$  and width of  $604\ \mu\text{m}$  is fabricated in  $525\ \mu\text{m}$  thick silicon substrates using photolithography followed by wet etching. A photoresist coating of  $10\ \mu\text{m}$  thickness (single/double coat) is used as the etch mask for wet etching. Silicon is considered as a suitable material for the fabrication of microreactors due to the high strength of the Si-Si bonds which results in the chemical inertness and thermal stability of silicon. The proposed design in AutoCAD for the mask is shown in the following figure.

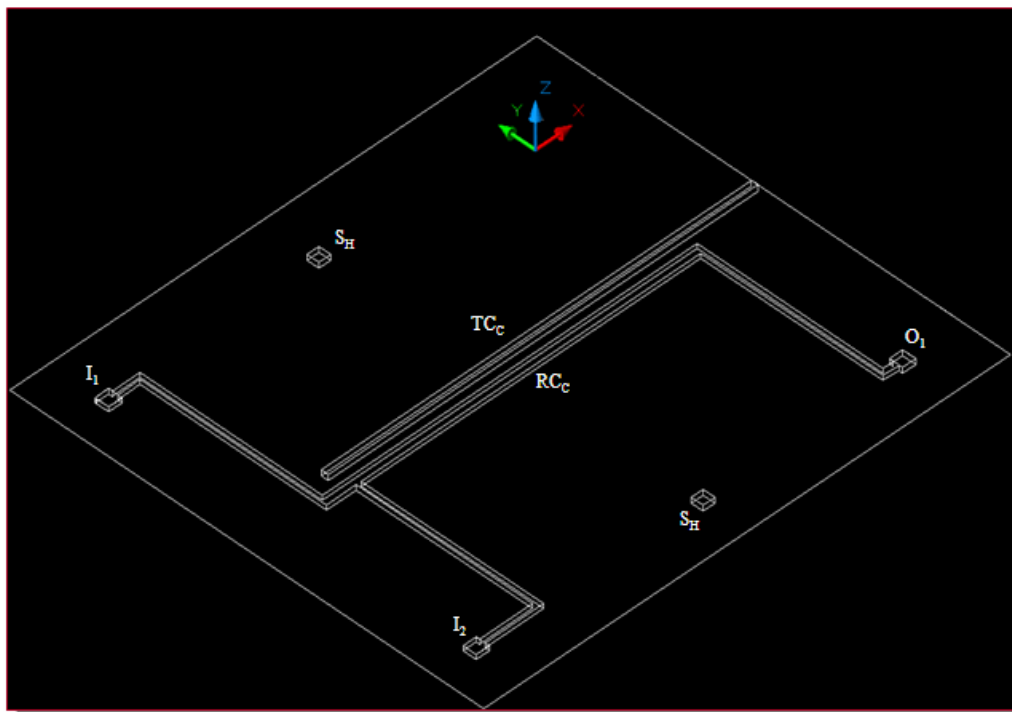


**Figure 53:** 3-dimensional microreactor design in AutoCAD program.

In the above microreactor design, major parts are denoted by abbreviations. The reactor has two inlet ports for H<sub>2</sub> and O<sub>2</sub> feed, i.e. I<sub>1</sub> and I<sub>2</sub> and the outlet port for H<sub>2</sub>O vapor is referred as O<sub>1</sub>. These inlets and outlet have a dimension of 1.8 mm in width and length while the depth is of 285 micron. The main reaction channel is denoted by RC<sub>C</sub>. It is 25 mm long and width and depth of that channel are dimensionalized with 275 micron. According to our numerical calculation, any diameter < 285 μm diameter at atmospheric pressure would be entirely safe to run homogeneous ignition without explosions in a microchannel reactor. As pressure drop calculations [Appendix C] show a maximum pressure could be obtained in this micro-channel reactor of up to 1 bar, we conducted calculations [see Figure 17] to ensure that 275 μm could also be safe at 2 bar. In addition to that, reactor safety with 275 μm is also verified with planar symmetric channel as that might lead to different ignition behavior than with the symmetric tubular channel used in our study. Interestingly, planar symmetric plates show extended ignition delay than the tubular channel, but 300 μm reassures the reactor safety also in that planar geometry (see subsection 4.2.7) which means diameters below 300 μm would safely carry out isothermal H<sub>2</sub> oxidation. That is why we have selected 275 μm channel depth in our new microreactor fabrication.

Thermocouple is to be placed in a parallel channel as close to the RC<sub>C</sub>, so that temperature profiles in the channel can be measured. This thermocouple channel is denoted by TC<sub>C</sub> in Figure 53. Thermocouple (TC) configuration is 250 micron o.d (outer diameter) and 127 micron i.d (inner diameter), considering this dimension of TC the dimension of TC<sub>C</sub> is set to 0.4602 and 0.325 mm maintaining 54.7° angle for etching. This TC provides the temperature profile during ignition studies.

Some considerations for the design are as follows:

- For clipping those two wafers together 2.5 mm distance is kept from the edge to the inlet-outlet ports.
- To properly align those two wafers we etch two square hollow grooves ( $S_H$ ) of 0.8 mm and with 275  $\mu\text{m}$  depth in both sides of the reaction channel. A pin of that width will be pushed through to align the two wafers.
- PDMS (poly dimethyl siloxane) is deposited on the inlets and outlet port through which bevel-port needles can be poked for the purpose of feeding and collecting gases.
- Gases are fed from the top through a bevel-port needle.
- An external heater will be placed at the top of the microreactor to initially heat up the gas mixture.
- For this initial design, no catalyst deposition method is considered in the reaction channel. Studies are thus restricted to purely homogeneous ignition.

For non-isothermal reactor operation, the wall temperature is not constant any more and a high temperature gradient is developed between catalytic wall and the reactor material due to different temperature expansion coefficient. This temperature flux is conducted through the wall to the outer boundary, i.e. reactor materials, adding up a constant temperature gradient to the inlet flow and results a shift in the ignition profile towards shorter axial length of the reactor. This can not be addressed through simplified boundary layer model and a full Navier Stokes model coded in commercial CFD (Computational Fluid Dynamics) software Fluent would be implemented for this study.

In this regard, numerical investigation of non-isothermal operation with Navier Stokes equations is preliminary performed where Figure 54 shows the view of designed microreactor from Figure 53 as imported into FLUENT for the mentioned purpose.

In the above imported geometry left two blue colored blocks are inlet ports and the right red colored block is the outlet port. The whole channel is tightly meshed with Hex/Wedge elements and Cooper type fine mesh in Gambit. In Fluent, the refined geometry is called from Gambit as 3-dimensional double precision, segregated, laminar flow model with energy balance and species transport in it.

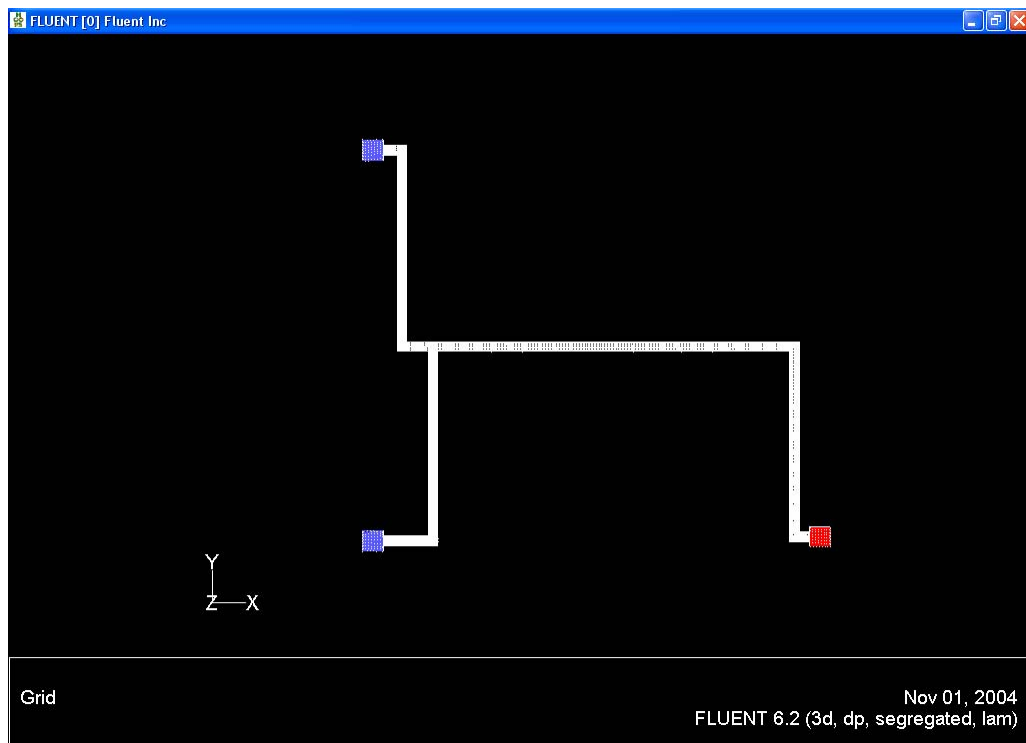


**Figure 54:** Imported view of the new microreactor in Fluent software.

As a very preliminary simulation attempt for gas flow, enormous back-mixing of gases are noticed in the results which need to be looked into detail.

## APPENDIX A

### MODEL DESCRIPTION & DETAILED KINETICS

CRESLAF employs boundary-layer approximation for the fluid-flow equations, coupled to gas phase and surface species continuity equations. Boundary layer approximations, originally conceived by Ludwig Prandtl, are very well-known in fluid mechanics and have been widely used since 1900s. Boundary layer behavior can be anticipated when there is a dominant flow direction. It is thus capable of describing coupled hydrodynamics, gas-phase chemistry and surface chemistry in a laminar flow channel. The boundary layer equations represent a coupled, nonlinear system of parabolic partial differential equations. It is restricted to a two-dimensional geometry, using either planar or radial coordinates. The simplification of this approximation leads to efficient computational algorithms. After finite difference discretization the resulting problem can be solved numerically by the method of lines as a differential-algebraic system. The applicability of these equations relies on the existence of a principal flow direction in which flow-wise diffusive transport is negligible compared to convective transport. Mathematically this reduction causes the boundary layer equations to essentially have parabolic characteristics whereas Navier-Stokes equations have the elliptic characteristics. As a result computational simulation of these boundary layer equations are much simpler and efficient.

Boundary conditions are required at the channel inlet where the dependent variables need to be specified, i.e. linear velocity, temperature, initial concentration of surface species. Heterogeneous

chemistry occurs on the wall where species boundary condition is derived from a species mass balance. The set of these equations describing the boundary layer model is listed in Table 2.

**Table 2:** Governing equations of the boundary layer model

<p>Momentum Balance:</p> $\rho u \cdot \frac{\partial u}{\partial x} - \frac{\rho u}{M} \left( \xi \cdot \frac{dM}{dx} - \frac{dM_l}{dx} \right) \frac{\partial u}{\partial \xi} + \frac{dp}{dx} = \frac{\rho u}{M^2} \cdot \frac{\partial}{\partial \xi} \left( \rho u \mu y^{2\alpha} \cdot \frac{\partial u}{\partial \xi} \right) + g \cdot (\rho_i - \rho)$ <p>Species Balance:</p> $\rho u \cdot \frac{\partial Y_k}{\partial x} - \frac{\rho u}{M} \left( \xi \cdot \frac{dM}{dx} - \frac{dM_l}{dx} \right) \frac{\partial Y_k}{\partial \xi} = \dot{\omega}_k W_k - \frac{\rho u}{M} \cdot \frac{\partial}{\partial \xi} (y^\alpha \cdot \rho Y_k V_{k,y}) \quad (k=1, \dots, K_g)$ <p>Energy Balance:</p> $\rho u c_p \cdot \frac{\partial T}{\partial x} - \frac{\rho u c_p}{M} \cdot \left( \xi \cdot \frac{dM}{dx} - \frac{dM_l}{dx} \right) \frac{dT}{d\xi} = \frac{\rho u}{M^2} \cdot \frac{\partial}{\partial \xi} \left( \rho u \lambda y^{2\alpha} \cdot \frac{\partial T}{\partial \xi} \right) - \sum_{k=1}^{K_g} \dot{\omega}_k W_k h_k - \frac{\rho^2 u y^\alpha}{M} \cdot \sum_{k=1}^K Y_k V_{k,y} c_{p,k} \cdot \frac{\partial T}{\partial \xi}$ <p>State equation [Ideal gas law]:</p> $P = \rho R T / \bar{W}$
---

For a flow in cylindrical coordinate, parameter  $\alpha$  is 1 and  $y$  represents the radius measured from the flow centerline. For further simplification of the numerical procedure, the equations are recasted by using the Von Mises Transformation in which cross-stream coordinate is replaced by the stream function as an independent variable. The detail of the numerical procedure is available in Chemkin user's guide manual [11].

## CHEMICAL KINETIC MODEL:

### Gas phase chemistry:

In our simulation, we have used the gas phase mechanism given in Table 2, from GRI mechanism [14]. The rate constant is computed using the modified Arrhenius expression,  $k = k_0 * T^\beta * \exp(-E/RT)$ , where E, R, and T are the activation energy, the universal gas constant and the temperature respectively.

**Table 3:** Gas-phase kinetics of H<sub>2</sub> – air mixture

No.	Reactions	$k_0$ [mol,cm,s]	$\beta$	E [kJ/mol]
1.	$H + O_2 \leftrightarrow O + OH$	$5.13 \times 10^{16}$	-0.82	69.1
2.	$H_2 + O \leftrightarrow H + OH$	$1.8 \times 10^{10}$	1.0	37.0
3.	$H_2 + OH \leftrightarrow H_2O + H$	$1.2 \times 10^9$	1.3	15.2
4.	$OH + OH \leftrightarrow H_2O + O$	$6.0 \times 10^8$	1.3	0.0
5.	$H_2 + O_2 \leftrightarrow OH + OH$	$1.7 \times 10^{13}$	0.0	200.0
6.	$H + OH + M \leftrightarrow H_2O + M^*$	$7.5 \times 10^{23}$	-2.6	0.0
7.	$O_2 + M \leftrightarrow O + O + M$	$1.9 \times 10^{11}$	0.5	400.1
8.	$H_2 + M \leftrightarrow H + H + M^{**}$	$2.2 \times 10^{12}$	0.5	387.7
9.	$H + O_2 + M \leftrightarrow HO_2 + M^\ddagger$	$2.1 \times 10^{18}$	-1.0	0.0
10.	$H + O_2 + O_2 \leftrightarrow HO_2 + O_2$	$6.7 \times 10^{19}$	-1.42	0.0
11.	$H + O_2 + N_2 \leftrightarrow HO_2 + N_2$	$6.7 \times 10^{19}$	-1.42	0.0
12.	$HO_2 + H \leftrightarrow H_2 + O_2$	$2.5 \times 10^{13}$	0.0	2.93
13.	$HO_2 + H \leftrightarrow OH + OH$	$2.5 \times 10^{14}$	0.0	7.9
14.	$HO_2 + O \leftrightarrow OH + O_2$	$4.8 \times 10^{13}$	0.0	4.2
15.	$HO_2 + OH \leftrightarrow H_2O + O_2$	$5.0 \times 10^{13}$	0.0	4.2
16.	$HO_2 + HO_2 \leftrightarrow H_2O_2 + O_2$	$2.0 \times 10^{12}$	0.0	0.0
17.	$H_2O_2 + M \leftrightarrow OH + OH + M$	$1.3 \times 10^{17}$	0.0	190.5
18.	$H_2O_2 + H \leftrightarrow HO_2 + H_2$	$1.7 \times 10^{12}$	0.0	15.9
19.	$H_2O_2 + OH \leftrightarrow H_2O + HO_2$	$1.0 \times 10^{13}$	0.0	7.5

M=third-body enhancement factors;

\*H<sub>2</sub>O/20.0/    \*\*H<sub>2</sub>O/6.0/ H/2.0/ H<sub>2</sub>/3.0/

‡H<sub>2</sub>O/21.0/ H<sub>2</sub>/3.3/ O<sub>2</sub>/0.0/ N<sub>2</sub>/0.0/

**GRI mechanism:** This is essentially a list of elementary chemical reactions and associated rate constant expressions. This is an optimized detailed chemical reaction mechanism capable of the best representation of natural gas flames and ignition which has been carried out at The University of California at Berkeley, Stanford University, the University of Texas at Austin, and SRI International.

***Surface Chemistry:***

The reactor model is coupled with detailed elementary step reaction kinetics, which considers catalytic reactions and intermediate products of oxidation of hydrogen on platinum surface. The SURFACE CHEMKIN software is used for the formulation of the surface mechanism. Surface kinetic model conserves the total number of surface sites:

$$\sum_{K_s^f}^{K_s^l} \Theta_k(n) = 1 \quad n = 1, \dots, N_s$$

To describe the influence of the wall on combustion, we have used four different surface mechanisms in our simulations: Three on platinum surface and one on a wall which promotes recombination of radicals.

For catalytic wall (Pt), the surface chemistry consists of 6 species and 13 reversible reactions [9] and the elementary step kinetics is listed below (Table 4). In addition to that, to examine the influence of different surface mechanisms of Pt wall on ignition behavior, which consists of individual forward and backward reaction steps, we have used two other surface kinetics in our simulations. Overall, the kinetic equations and rate parameters on platinum for these three different surface mechanisms are used from (I).Andrae et.al [9] (Table 5), (II) Park et.al [16] (Table 6) and (III) Aghalayam et.al [17] (Table 7).

The surface site density of the catalytic surface (Pt) is 2.71E-9 mol/cm<sup>2</sup>. Reaction rates for all reaction steps except for the adsorption of the gas phase species are calculated with the Arrhenius Law:  $k = k_0 \cdot \exp(-E/RT)$ . The adsorption steps are non-activated and are calculated

$$\text{using the kinetic gas theory: } k_{\text{ads}} = \frac{s}{\sqrt{2\pi \cdot M \cdot R \cdot T_g}}$$

### Catalytic Material: Pt

**Table 4:** Surface reaction steps and rate parameters by Andrae et.al [63].

No.	Reactions	s	$k_0$ [mol,cm,s]	$E_{\text{des/act}}$ [kJ/mol]
1.	$\text{H}_2 + \text{PT}(\text{S}) \leftrightarrow \text{H}_2(\text{S})$	0.05		0.0
2.	$\text{H}_2(\text{S}) + \text{PT}(\text{S}) \leftrightarrow \text{H}(\text{S}) + \text{H}(\text{S})$		$7.5 \times 10^{22}$	15.6
3.	$\text{O}_2 + \text{PT}(\text{S}) \leftrightarrow \text{O}_2(\text{S})$	0.023		0.0
4.	$\text{O}_2 + \text{PT}(\text{S}) \leftrightarrow \text{O}(\text{S}) + \text{O}(\text{S})$		$2.5 \times 10^{24}$	0.0
5.	$\text{H}(\text{S}) + \text{O}(\text{S}) \leftrightarrow \text{OH}(\text{S}) + \text{PT}(\text{S})$		$3.7 \times 10^{21}$	19.3
6.	$\text{H}(\text{S}) + \text{OH}(\text{S}) \leftrightarrow \text{H}_2\text{O}(\text{S})$		$3.7 \times 10^{21}$	0.0
7.	$\text{OH}(\text{S}) + \text{OH}(\text{S}) \leftrightarrow \text{H}_2\text{O}(\text{S}) + \text{O}(\text{S})$		$3.7 \times 10^{24}$	100.5
8.	$\text{H} + \text{PT}(\text{S}) \leftrightarrow \text{H}(\text{S})$	1.00		0.0
9.	$\text{O} + \text{PT}(\text{S}) \leftrightarrow \text{O}(\text{S})$	1.00		0.0
10.	$\text{H}_2\text{O} + \text{PT}(\text{S}) \leftrightarrow \text{H}_2\text{O}(\text{S})$	0.75		0.0
11.	$\text{OH} + \text{PT}(\text{S}) \leftrightarrow \text{OH}(\text{S})$	1.00		0.0
12.	$\text{H}_2\text{O}_2 + \text{PT}(\text{S}) \leftrightarrow \text{OH}(\text{S}) + \text{OH}(\text{S})$	1.00		0.0
13.	$\text{HO}_2 + \text{PT}(\text{S}) \leftrightarrow \text{OH}(\text{S}) + \text{O}(\text{S})$	1.00		0.0

s= sticking coefficient;  $k_0$  = pre-exponential factor;  $E_{\text{des/act}}$  = desorption or activation energy

Most surface science experiments are conducted under low or well characterized adsorbate coverages on single crystals and the role of adsorbate coverage in surface reaction pathways is known only for limited conditions. Using available experimental data for Pt catalyzed H<sub>2</sub>-oxidation in the literature for adsorbate-adsorbate interactions and with the help of UBI-QEP method, a surface reaction mechanism has been developed for oxidation of H<sub>2</sub> by Park et.al [16]. This kinetics is thermodynamically consistent and takes into consideration the change in

activation energies of reaction pathways with varying adsorbate coverages of surface species.

This has been used in our simulation (II) and the following tabulates the detailed kinetics.

**Table 5:** Surface reaction steps and rate parameters by Park et.al [60].

No.	Reactions	s	$k_0$ [mol,cm,s]	$E_{des/act}$ [kJ/mol]		
				$\Theta^* = 1$	$\Theta_H = 1$	$\Theta_O = 1$
1.	$H_2 + 2PT(S) \Rightarrow 2H(S)$	0.50		0.0	0.0	0.0
2.	$2H(S) \Rightarrow H_2 + 2PT(S)$		1.0E+12	83.7	58.6	83.7
3.	$O_2 + PT(S) \Rightarrow 2O(S)$	0.03		0.0	0.0	0.0
4.	$2O(S) \Rightarrow O_2 + PT(S)$		1.0E+13	213.4	213.4	794.96
5.	$OH + PT(S) \Rightarrow OH(S)$	1.00		0.0	0.0	0.0
6.	$OH(S) \Rightarrow OH + PT(S)$		5.0E+14	263.6	263.6	125.52
7.	$H_2O + PT(S) \Rightarrow H_2O(S)$	0.70		0.0	0.0	0.0
8.	$H_2O(S) \Rightarrow H_2O + PT(S)$		1.0E+13	41.84	41.84	41.84
9.	$H + PT(S) \Rightarrow H(S)$	1.00		0.0	0.0	0.0
10.	$H(S) \Rightarrow H + PT(S)$		1.0E+13	251.88	251.88	251.88
11.	$O + PT(S) \Rightarrow O(S)$	1.00		0.0	0.0	0.0
12.	$O(S) \Rightarrow O + PT(S)$		1.E+13	387.44	387.44	280.33
13.	$OH(S) + PT(S) \Rightarrow O(S) + H(S)$		6.1E+11	102.1	108.4	769.9
14.	$H(S) + O(S) \Rightarrow OH(S) + PT(S)$		1.7E+10	51.88	36.8	56.1
15.	$H_2O(S) + PT(S) \Rightarrow H(S) + OH(S)$		1.2E+10	77.28	84.52	163.6
16.	$H(S) + OH(S) \Rightarrow H_2O(S) + PT(S)$		3.5E+11	51.88	38.91	0.0
17.	$H_2O(S) + O(S) \Rightarrow 2OH(S)$		1.E+11	52.8	52.8	142.7
18.	$2OH(S) \Rightarrow H_2O(S) + O(S)$		1.E+11	79.1	79.1	0.0

In succession to the previous study Aghalayam et.al used sensitivity analysis to identify the key kinetic parameters and calculated adsorbate-adsorbate interaction with regard to their influence on activation energies. This methodology is identical with the previous one by Park et.al. The difference between those two methodologies is that in the following mechanism Aghalayam et.al optimized the pre-exponential factors to refine kinetic parameters using  $H_2$ -oxidation as a model system on Pt.

**Table 6:** Surface reaction steps and rate parameters by Aghalayam et.al [62]

No.	Reactions	s	$k_0$ [1/s]	$E_{des/act}$ [kJ/mol]
1.	$H_2 + 2PT(S) \Rightarrow 2H(S)$	0.48		0.0
2.	$2H(S) \Rightarrow H_2 + 2PT(S)$		9.4E+11	84.0
3.	$O_2 + PT(S) \Rightarrow O_2(S)$	0.03		0.0
4.	$O_2(S) \Rightarrow O_2 + PT(S)$		1.0E+13	214.2
5.	$OH + PT(S) \Rightarrow OH(S)$	1.00		0.0
6.	$OH(S) \Rightarrow OH + PT(S)$		1.0E+13	264.6
7.	$H_2O + PT(S) \Rightarrow H_2O(S)$	0.75		0.0
8.	$H_2O(S) \Rightarrow H_2O + PT(S)$		1.0E+13	42.0
9.	$H + PT(S) \Rightarrow H(S)$	1.00		0.0
10.	$H(S) \Rightarrow H + PT(S)$		1.0E+13	252.84
11.	$O + PT(S) \Rightarrow O(S)$	1.00		0.0
12.	$O(S) \Rightarrow O + PT(S)$		1.E+13	281.4
13.	$OH(S) + PT(S) \Rightarrow O(S) + H(S)$		6.1E+11	102.48
14.	$H(S) + O(S) \Rightarrow OH(S) + PT(S)$		1.7E+10	50.82
15.	$H_2O(S) + PT(S) \Rightarrow H(S) + OH(S)$		1.2E+10	77.28
16.	$H(S) + OH(S) \Rightarrow H_2O(S) + PT(S)$		3.5E+11	52.08
17.	$H_2O(S) + O(S) \Rightarrow 2OH(S)$		1.E+11	52.92
18.	$2OH(S) \Rightarrow H_2O(S) + O(S)$		1.E+11	79.38

**Catalytic Material: Pd**

In the following table (Table 7) elementary kinetics of H<sub>2</sub>-oxidation on Pd surface is enlisted

[67] where surface site density of the clean surface is used as  $2.54 \cdot 10^{-9}$  cm<sup>2</sup>/s.

**Table 7:** Detailed surface kinetics of H<sub>2</sub>-oxidation on Pd surface [67]

No.	Reactions	s	k (mol,cm,s)	E <sub>act/des</sub> (kJ/mol)
1.	H <sub>2</sub> + 2PD(S) => 2H(S)	0.32		0.0
2.	2H(S) => H <sub>2</sub> + 2PD(S)		3.95*10 <sup>21</sup>	41.5
3.	O <sub>2</sub> + PD(S) => 2O(S)	0.45		0.0
5.	2O(S) => O <sub>2</sub> + 2PD(S)		3.95*10 <sup>19</sup>	180.0
6.	OH + PD(S) => OH(S)	0.99		0.0
8.	OH(S) => OH + PD(S)		1.*10 <sup>13</sup>	251.0
9.	H <sub>2</sub> O + PD(S) => H <sub>2</sub> O(S)	0.99		0.0
10.	H <sub>2</sub> O(S) => H <sub>2</sub> O + PD(S)		1.*10 <sup>13</sup>	41.9
11.	H + PD(S) => H(S)	0.99		0.0
12.	H(S) => H + PD(S)		1.*10 <sup>13</sup>	236.0
13.	O + PD(S) => O(S)	0.99		0.0
14.	O(S) => O + PD(S)		1.*10 <sup>13</sup>	340.0
15.	H(S) + O(S) = OH(S) + PD(S)		3.95.*10 <sup>18</sup>	59.8
16.	H(S) + OH(S) = H <sub>2</sub> O(S) + PD(S)		3.95.*10 <sup>21</sup>	40.5
17.	H(S) + O(S) = OH(S) + PD(S)		3.95.*10 <sup>21</sup>	40.5

*s* = sticking coefficient; *k*<sub>0</sub> = pre-exponential factor; *E*<sub>des/act</sub> = desorption or activation energy where PD(S) denotes the vacant surface sites on Pd surface and (S) designates the corresponding surface species.

It is reported in [67] with regards to the above mentioned surface kinetics that reactions 16, 17 and 18 are the Langmuir-Hinshelwood surface reactions and the kinetics of the reverse reactions are not measured in there. Therefore we again modified the kinetics and measured the activation energy of the reverse reactions of 16, 17 and 18, i.e. 304.19, 162.77 and 86.95 kJ/mol using the energy cycle from the corresponding heat of reactions. We incorporated these energies with pre-

exponential factor of  $1 \cdot 10^{13}$  1/s for 16, 17 & 18 reactions in the improved kinetics which gave insignificant difference in the ignition results with the kinetics in Table 7.

Non-catalytic Material: Quartz/Silicon (Radical Recombination reactions)

In our study a RR wall is treated which surface recombines the intermediate species i.e. radicals, such as H, OH, O, H<sub>2</sub>O<sub>2</sub>, HO<sub>2</sub> and produces stable species, finally that desorbs into the gas phase. Furthermore, the surface mechanism for RR wall is comprised of 6 species and 8 irreversible reactions (Table 8) [8]. The thermodynamic and transport database are used from GRI mechanism. Surface site density for a clean quartz surface is used identical as Pt surface, i.e.  $2.71 \cdot 10^{-9}$

**Table 8:** Surface reaction steps and rate parameters by Andrae et.al [63]

No.	Reactions	s	k (1/s)	E (kJ/mol)
1.	H + S => H(S)	1.00		0.0
2.	2H(S) => H <sub>2</sub> + 2S		$1 \cdot 10^{13}$	0.0
3.	O + S => O(S)	1.00		0.0
4.	2O(S) => O <sub>2</sub> + 2S		$1 \cdot 10^{13}$	0.0
5.	OH + S => OH(S)	1.00		0.0
6.	2OH(S) => H <sub>2</sub> O + O(S) + S		$1 \cdot 10^{13}$	0.0
7.	HO <sub>2</sub> + 2S => OH(S) + O(S)	1.00		0.0
8.	H <sub>2</sub> O <sub>2</sub> + 2S => 2OH(S)	1.00		0.0

*s* = sticking coefficient; *k*<sub>0</sub> = pre-exponential factor; *E*<sub>des/act</sub> = desorption or activation energy where *S* denotes the vacant surface sites on quartz surface and (*S*) corresponding surface species.

All the reactions are irreversible and non-activated in the above mechanism which is doesn't hold up the reversibility in the elementary reaction steps. Therefore, to justify the reversibility, we modified the above mechanism where reverse reaction steps are added for the desorption reactions. From the heat of formation of individual species and using Hess's law, the activation energy of the corresponding elementary steps is calculated. This modified mechanism of radical recombination wall is tabulated in Table 9.

**Table 9:** Modified surface kinetics of Radical Recombination wall

No.	Reactions	s	k (1/s)	$E_{act/des}$ (kJ/mol)
1.	$H + S \Rightarrow H(S)$	1.00		0.0
2.	$2H(S) \Rightarrow H_2 + 2S$		$1.*10^{13}$	0.0
3.	$H_2 + 2S \Rightarrow 2H(S)$		$1.*10^{13}$	436.015
4.	$O + S \Rightarrow O(S)$	1.00		0.0
5.	$2O(S) \Rightarrow O_2 + 2S$		$1.*10^{13}$	0.0
6.	$O_2 + 2S \Rightarrow 2O(S)$		$1.*10^{13}$	498.314
7.	$OH + S \Rightarrow OH(S)$	1.00		0.0
8.	$OH(S) \Rightarrow OH + S$		$1.*10^{13}$	160.440
9.	$2OH(S) \Rightarrow H_2O + O(S) + S$		$1.*10^{13}$	0.0
10.	$HO_2 + 2S \Rightarrow OH(S) + O(S)$	1.00		0.0
11.	$OH(S) + O(S) \Rightarrow HO_2 + 2S$		$1.*10^{13}$	131.880
12.	$H_2O_2 + 2S \Rightarrow 2OH(S)$	1.00		0.0
13.	$2OH(S) \Rightarrow H_2O_2 + 2S$		$1.*10^{13}$	106.260

$s$  = sticking coefficient;  $k_0$  = pre-exponential factor;  $E_{des/act}$  = desorption or activation energy where  $S$  denotes the vacant surface sites on quartz surface and  $(S)$  corresponding surface species.

Now the surface kinetics of radical recombination wall consists of 13 reactions where 5 reactions are reversible excepting adsorption of atomic oxygen and hydrogen (heat of reaction of atomic H and O from quartz surface are not available in literature) and H<sub>2</sub>O adsorption on the surface. Surface site density remains unchanged as the clean quartz surface. Pre-exponential factor of those reverse reactions are all set to  $1 \times 10^{13}$ .

To investigate the influence of individual radicals on overall ignition we isolated the kinetics of individual radicals from Table 9. Ignition of H, OH, O, H<sub>2</sub>O<sub>2</sub> and HO<sub>2</sub> are independently studied in our numerical approach where notably HO<sub>2</sub> did not show any numerically detectable conversion of reactants indeed.

**Table 10:** Individual radical kinetics on Radical Recombination surface

No.	Reactions	s	k (1/s)	E (kJ/mol)
<i>Individual H radical assisted radical recombination reaction:</i>				
1.	$H + S \Rightarrow H(S)$	1.00		0.0
2.	$2H(S) \Rightarrow H_2 + 2S$		$1.*10^{13}$	0.0
3.	$H_2 + 2S \Rightarrow 2H(S)$		$1.*10^{13}$	436.015
<i>Individual O radical assisted radical recombination reaction:</i>				
1.	$O + S \Rightarrow O(S)$	1.00		0.0
2.	$2O(S) \Rightarrow O_2 + 2S$		$1.*10^{13}$	0.0
3.	$O_2 + 2S \Rightarrow 2O(S)$		$1.*10^{13}$	498.314
<i>Individual OH radical assisted radical recombination reaction:</i>				
1.	$OH + S \Rightarrow OH(S)$	1.00		0.0
2.	$OH(S) \Rightarrow OH + S$		$1.*10^{13}$	160.440
3.	$2OH(S) \Rightarrow H_2O + O(S) + S$		$1.*10^{13}$	0.0
<i>Individual H<sub>2</sub>O<sub>2</sub> radical assisted radical recombination reaction:</i>				
1.	$H_2O_2 + 2S \Rightarrow 2OH(S)$	1.00		0.0
2.	$2OH(S) \Rightarrow H_2O_2 + 2S$		$1.*10^{13}$	106.260
<i>Individual HO<sub>2</sub> radical assisted radical recombination reaction:</i>				
1.	$HO_2 + 2S \Rightarrow OH(S) + O(S)$	1.00		0.0
2.	$OH(S) + O(S) \Rightarrow HO_2 + 2S$		$1.*10^{13}$	131.880

## CO oxidation on Pt catalyst

Gas phase kinetics for CO oxidation reaction system is primarily taken from Yetter et.al [42] while homogeneous kinetics from GRI mechanism [66] is compared with the result. GRI shows shorter ignition delay and hence simulation of coupled mechanism is performed with GRI mechanism instead of Yetter kinetics tabulated in Table 11.

**Table 11:** The gas phase CO oxidation mechanism from Yetter et.al [42]

No.	Reactions	$k_0$ [mol,cm,s]	$\beta$	E [kcal/mol]
<i>H<sub>2</sub>-O<sub>2</sub> Chain Reactions</i>				
1.	H + O <sub>2</sub> = O + OH	1.900E+14	0.00	16.44
2.	O + H <sub>2</sub> = H + OH	5.13E+4	2.67	6.29
3.	OH + H <sub>2</sub> = H + H <sub>2</sub> O	2.14E+8	1.51	3.43
4.	OH + OH = O + H <sub>2</sub> O	5.00E+11	0.00	16.29
<i>H<sub>2</sub>-O<sub>2</sub> Dissociation/Recombination Reactions</i>				
5.	H <sub>2</sub> + N <sub>2</sub> = H + H + N <sub>2</sub>	4.57E+19	-1.40	104.38
6.	H <sub>2</sub> + AR = H + H + AR	5.89E+18	-1.10	104.38
7.	O + O + N <sub>2</sub> = O <sub>2</sub> + N <sub>2</sub>	6.17E+15	-0.50	0.00
8.	O + O + AR = O <sub>2</sub> + AR	1.91E+13	0.00	-1.79
9.	O + H + M = OH + M	4.68E+18	-1.00	0.00
10.	H + OH + N <sub>2</sub> = H <sub>2</sub> O + N <sub>2</sub>	2.24E +22	-2.00	0.00
11.	H + OH + AR = H <sub>2</sub> O + AR	8.32E+21	-2.00	0.00
<i>Formation and Consumption of HO<sub>2</sub></i>				
12.	H + O <sub>2</sub> + N <sub>2</sub> = HO <sub>2</sub> + N <sub>2</sub>	6.76E+19	-1.42	0.00
13.	H + O <sub>2</sub> + AR = HO <sub>2</sub> + AR	1.15E+15	0.00	-1.0
14.	HO <sub>2</sub> + H = H <sub>2</sub> + O <sub>2</sub>	6.61E+13	0.00	2.13
15.	HO <sub>2</sub> + H = OH + OH	1.70E+14	0.00	0.87
16.	HO <sub>2</sub> + O = OH + O <sub>2</sub>	1.74E+13	0.00	-0.4
17.	HO <sub>2</sub> + OH = H <sub>2</sub> O + O <sub>2</sub>	1.45E+16	-1.00	0.00
<i>Formation and Consumption of H<sub>2</sub>O<sub>2</sub></i>				
18.	HO <sub>2</sub> + HO <sub>2</sub> = H <sub>2</sub> O <sub>2</sub> + O <sub>2</sub>	3.02E+12	0.00	1.39

19.	$\text{H}_2\text{O}_2 + \text{N}_2 = \text{OH} + \text{OH} + \text{N}_2$	1.20E+17	0.00	45.5
20.	$\text{H}_2\text{O}_2 + \text{AR} = \text{OH} + \text{OH} + \text{AR}$	8.51E+16	0.00	45.5
21.	$\text{H}_2\text{O}_2 + \text{H} = \text{H}_2\text{O} + \text{OH}$	1.00E+13	0.00	3.59
22.	$\text{H}_2\text{O}_2 + \text{H} = \text{H}_2 + \text{HO}_2$	4.79E+13	0.00	7.95
23.	$\text{H}_2\text{O}_2 + \text{O} = \text{OH} + \text{HO}_2$	9.55E+6	2.00	3.97
24.	$\text{H}_2\text{O}_2 + \text{OH} = \text{H}_2\text{O} + \text{HO}_2$	7.08E+12	0.00	1.43
<i>Oxidation of CO</i>				
25.	$\text{CO} + \text{O} + \text{N}_2 = \text{CO}_2 + \text{N}_2$	2.51E+13	0.00	4.54
26.	$\text{CO} + \text{O} + \text{AR} = \text{CO}_2 + \text{AR}$	2.19E+13	0.00	-4.54
27.	$\text{CO} + \text{O}_2 = \text{CO}_2 + \text{O}$	2.51E+12	0.00	47.69
28.	$\text{CO} + \text{OH} = \text{CO}_2 + \text{H}$	5.00E+12	0.00	9.91
29.	$\text{CO} + \text{HO}_2 = \text{CO}_2 + \text{OH}$	6.03E+13	0.00	22.95
<i>Formation and Consumption of HCO</i>				
30.	$\text{HCO} + \text{N}_2 = \text{H} + \text{CO} + \text{N}_2$	1.86E+17	-1.00	17.0
31.	$\text{HCO} + \text{AR} = \text{H} + \text{CO} + \text{AR}$	1.86E+17	-1.00	17.0
32.	$\text{HCO} + \text{O}_2 = \text{CO} + \text{HO}_2$	7.59E+12	0.00	0.41
33.	$\text{HCO} + \text{H} = \text{CO} + \text{H}_2$	7.24E+13	0.00	0.00
34.	$\text{HCO} + \text{O} = \text{CO} + \text{OH}$	3.02E+13	0.00	0.00
35.	$\text{HCO} + \text{OH} = \text{CO} + \text{H}_2\text{O}$	3.02E+13	0.00	0.00

---

$M = \text{third-body factor, i.e. } \text{H}_2\text{O}/21.0/ \text{H}_2/3.3/$

### ***Surface Kinetics of CO oxidation:***

Kinetics of catalytic CO oxidation is shown in Table 12. The adsorbate-adsorbate interactions [91] considered are O-O and CO-CO, based on the available literature. Coverage dependence is applied in this mechanism for the desorption energy in case of two reaction steps. One is the activation energy for desorption of oxygen which is taken as  $E_d(\text{O}) = 212.42 - 134.4\theta_o$ , where  $\theta_o$  is the coverage of oxygen on the surface. A linear dependence of the activation energy on CO coverage has been assumed in this study as well with a repulsive interaction of 21 kJ/mol. Therefore, the activation energy for CO desorption is thus taken as  $E_d(\text{CO}) = 212.42 - 134.4\theta_{\text{CO}}$ .

**Table 12:** The Catalytic CO oxidation mechanism on clean polycrystalline platinum ( $\theta_{PT}=1$ )

No.	Reactions	s	$k_0$ [mol,cm,s]	$E_{des/act}$ [kJ/mol]
1.	$O_2 + 2PT(S) \Rightarrow 2O(S)$	0.1		0.0
2.	$2O(S) \Rightarrow O_2 + 2PT(S)$		$1.*10^{13}$	214.2
3.	$O + PT(S) \Rightarrow O(S)$	1.00		0.0
4.	$O(S) \Rightarrow O + PT(S)$		$1.*10^{13}$	281.4
5.	$CO + PT(S) \Rightarrow CO(S)$	0.89		0.0
6.	$CO \Rightarrow CO + PT(S)$		$1.*10^{15}$	184.8
7.	$CO_2 + PT(S) \Rightarrow CO_2(S)$	1.00		0.0
8.	$CO_2(S) \Rightarrow CO_2 + PT(S)$		$1.*10^{11}$	71.4
9.	$CO_2 + PT(S) \Rightarrow CO(S) + O(S)$		$1.*10^{11}$	79.8
10.	$CO + O(S) \Rightarrow CO_2(S) + PT(S)$		$1.*10^{11}$	46.2

**NO Oxidation:** Homogeneous kinetics is taken from GRI mechanism [66]. But for surface kinetics  $NH_3$  oxidized on Pt is taken into account according to Andrae et.al [73] and we add an  $NH_3$  subset in the Pt surface kinetics.

**Table 13:** The Catalytic  $NH_3$  oxidation mechanism on clean polycrystalline platinum [73]

No.	Reactions	s	$k_0$ [mol,cm,s]	$E_{des/act}$ [kJ/mol]
1.	$NH_3 + 2PT(S) \Rightarrow NH_2(S) + H(S)$	0.1		0.0
2.	$NH_2(S) + H(S) \Rightarrow NH(S) + H(S)$		$3.7*10^{21}$	20.0
3.	$NH(S) + H(S) \Rightarrow N(S) + H(S)$		$3.7*10^{21}$	20.0
4.	$N(S) + O(S) \Rightarrow NO(S) + PT(S)$		$3.7*10^{21}$	20.0
5.	$NO(S) \Rightarrow NO + PT(S)$		$1.0*10^{13}$	20.0

## APPENDIX B

### VALIDATION OF BOUNDARY LAYER MODEL & MEAN FREE PATH CALCULATION

The continuum assumption in the Navier-Stokes equations, which reflects in boundary layer model, is valid provided the mean free path of the molecules is smaller than the characteristic dimension of the flow domain. Otherwise, fluid will no longer be under local thermodynamic equilibrium and velocity profiles, boundary wall shear stresses, mass flow rates and pressure differences will then be influenced by non-continuum effects. Additionally, conventional no-slip boundary condition imposed at the gas-solid interface will begin to break down. The value of Knudsen number,  $Kn$ , [the ratio between the mean free path  $\lambda$  and the characteristic dimension of flow geometry] determines the validity of the continuum flow assumption. The range of calculated  $Kn$  number for the defined microreactor dimension in this study lies between  $1.E-5$  -  $1.E-4$ . As for  $Kn \leq 1.E-3$ , the continuum hypothesis is appropriate and the flow can be analyzed using the Navier-Stokes equations with conventional no-slip boundary conditions. Therefore, CRESLAF which describes a boundary layer flow can validate the gas-surface interactions in microreactor channel.

#### *Mean Free Path Calculation of Reactant Molecules:*

The mean free path,  $\lambda$ , is the average distance a molecule travels between collisions.  $\lambda$  is directly proportional to reaction temperature and mathematically can be expressed as follows [96]:

$$\lambda = \frac{1}{\sqrt{2}} \frac{kT}{\sigma P} \quad (1)$$

where,

k = boltzman constant = 1.3807E-23 N-m/K

T = temperature [K]

$\sigma$  = collision area [m<sup>2</sup>];  $\sigma_{H_2} = 2.827\text{\AA}$ ;  $\sigma_{H_2O} = 2.641\text{\AA}$ ;  $\sigma_{O_2} = 3.467\text{\AA}$ ;  $\sigma_{N_2} = 3.798\text{\AA}$  [96]

P = pressure [N/m<sup>2</sup>]

At ambient pressure, temperature ranging from room temperature to 1000K, the mean free path of H<sub>2</sub> molecule calculated using equation (1) of 137 to 458 nm. Similarly O<sub>2</sub> and N<sub>2</sub> molecules also exhibit  $\lambda$  in nanometer range which clearly explains the range of dimensionless Knudsen number at atmospheric conditions with diameters varying from 1mm to 250  $\mu\text{m}$ . It is known that when the dimension of a molecule becomes smaller than the mean free path of that molecule, quenching occurs. In our meso-scale study, these calculated mean free paths are too low in terms of 'micro-scale' reactor dimension which explains that the discussion of mean free path regarding quenching is trivial in microreactor systems.

## APPENDIX C

### CALCULATION OF PRESSURE DROP IN MICROCHANNEL

Laminar flow characteristics in microreactor imply that the Reynolds number (Re) of the flow lies < 21000.

$$\text{Re} = \frac{Dv\rho}{\mu} \quad (1)$$

$$D = 1 \text{ mm} - 1\mu\text{m},$$

$$v = 9 \text{ m/s},$$

$$\rho_{mix} = 0.071 \text{ g/l (300K and 1 bar)},$$

$$\mu_{mix} = 15.89 \cdot 10^{-6} \text{ Pa.s (300K and 1 bar)},$$

Equation (1) results in Re ranging from 40.21 to 4.21.

Similarly important dimensionless number for heat transfer is Prandtl number (Pr) and that is 1.77 for this reaction system which is calculated via following expression:

$$\text{Pr} = \frac{\mu C_p}{k} \quad (2)$$

$$\mu_{mix} = 15.89 \cdot 10^{-6} \text{ Pa.s (300K and 1 bar)},$$

$$C_{p\ mix} = 4.85 \text{ J/g.K (300K and 1 bar)},$$

$$k_{mix} = 43.6 \text{ mW/m.K (300K and 1 bar)},$$

To calculate the pressure drop in the flow tube we used the following Hagen Poiseuille equation as the flow is laminar in microreactor which correlates pressure drop and average linear velocity in horizontal pipe [97].

$$\Delta P = 8 \frac{\mu L v_{x,ave}}{R^2} \quad (3)$$

In microreactor, pressure drop would be expected to be higher than the conventional reactor. To ensure whether the pressure drop is not high enough which can alter the characteristics of the intrinsic reactor safety in microchannel reactor we estimated the pressure drop at the extreme conditions operated in the microreactor. The calculation is tabulated as follows where the average linear velocity is 9 m/s.

**Table 14:** Pressure drop calculation in microreactor for two limiting cases

Limit I

	L [m]-R [μm]	$\mu_{mix}$ (300K, 10bar) [Pa-s]	$\Delta P$ [bar]
<b>reactants</b>	0.001-100	$17.28 * 10^{-6}$	$4.98 * 10^{-3}$
<b>products</b>	0.001-100	$17.42 * 10^{-6}$	$5.02 * 10^{-3}$

Limit II:

	L [m]-R [μm]	$\mu_{mix}$ (1500K, 1bar) [Pa-s]	$\Delta P$ [bar]
<b>reactants</b>	1-1000	$35.75 * 10^{-6}$	$1.03 * 10^{-1}$
<b>products</b>	1-1000	$36.26 * 10^{-6}$	$2.95 * 10^{-1}$

The pressure drop calculation of these limiting cases designates that pressure drop will not exceed the maximum of 0.3 bar in any combination of stoichiometric H<sub>2</sub>-air mixture in catalytic microrecators and that is not that significant for the safe reactor operation.

For the critical quenching in case of isothermal H<sub>2</sub> oxidation operation, the calculated pressure drop with 275 μm diameter at ambient condition would be 0.018 bar within 25 mm reactor length.

In addition to this pressure drop calculation in microchannel, we also developed a correlation between ignition distance (X<sub>ign</sub>) for homogeneously dominated high temperature branch for Pt wall and separately for heterogeneously dominated low temperature branch. We mathematically fitted ignition distance as a function of pressure separately for homogeneous branch at 1758K and heterogeneous branch at 973K which are shown in the following figure. At higher temperature X<sub>ign</sub> shows an inverse dependency with pressure while at low temperature direct dependence is apparent in the fitted expression. The mathematical fitting expression is discussed in section 4.2.4.

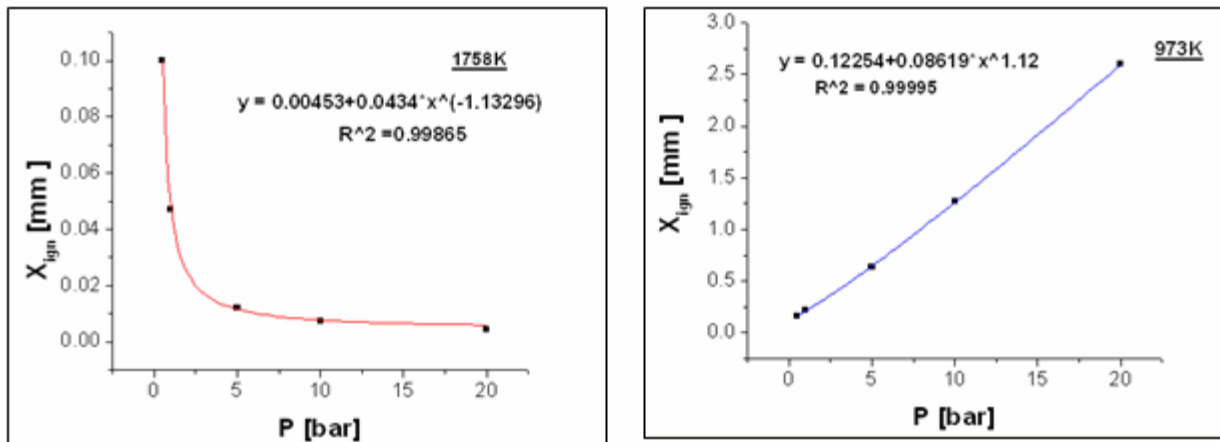


**Figure 55:** Mathematical fit of ignition distance vs. pressure at 1758K (left) and at 973K (right).

## APPENDIX D

### INFLUENCE OF VELOCITY DISTRIBUTION ON OVERALL IGNITION

All these discussed simulations have been performed with a fully developed parabolic velocity profile. According to the experiment, feed gases are not premixed before and therefore velocity enters with a flat entrance and then gradually develops a parabolic velocity distribution. Reactant gases are not well mixed at the entrance which ensures flat profile and then it mixes well which designates fully developed flow in a flow tube reactor confirming the laminar flow in microchannel reactor.

Following Figure 56 shows the velocity distribution for both cases we have used for the entire simulation.

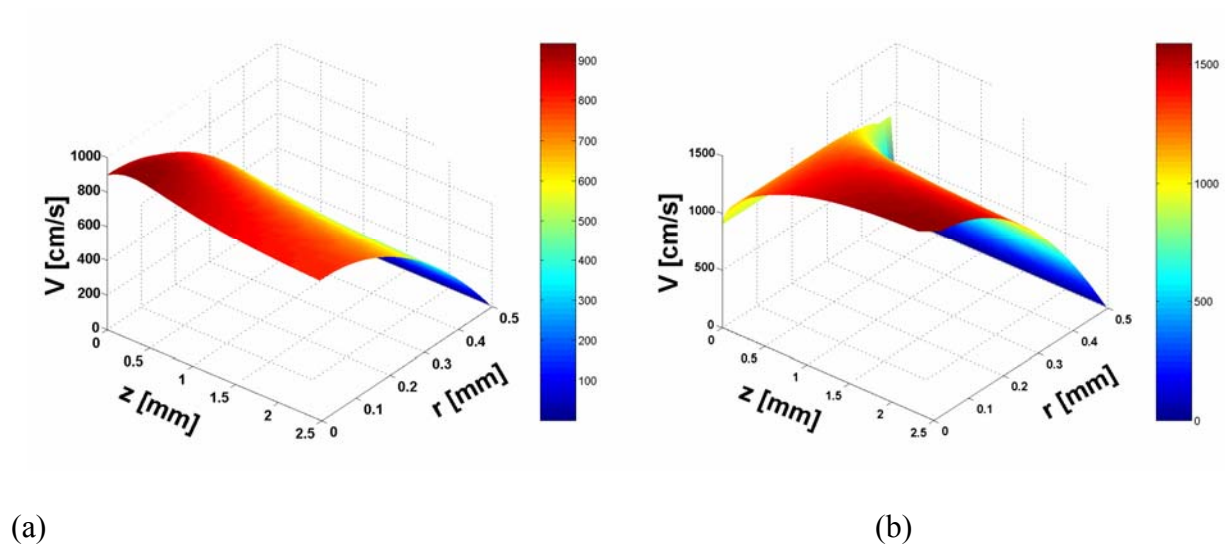


**Figure 56:** Velocity distribution in a microreactor with 1 mm diameter and inert wall for fully developed flow (left) and the flow having a flat entrance with gradually developing parabolic velocity (right) versus axial and radial length of the reactor at 1173K.

The distribution of linear velocity is displayed in the above plot as a function of reactor length and radius of the reactor for a stoichiometric H<sub>2</sub>-air mixture in a microreactor with 1 mm diameter for purely homogeneous case. where In the left graph, linear inlet velocity is 9 m/s when a parabolic velocity profile is developed from the reactor entrance. In the right graph to maintain a flat entrance and consequently develop a fully developed flow of 9 m/s average linear velocity, the calculated inlet velocity is set to 6 m/s. In this later case, after 0.2 mm axial distance parabolic velocity profile is gradually developed in the microreactor. Both cases designate a laminar flow in the channel that is one of the major characteristics of microreactor which validates our BL model.

Hence, we also investigated the influence of fully developed velocity profile with a flat entrance to assure the observed quenching phenomenon with Pt catalytic wall. Figure 57 shows the size effect where ignition distance is plotted as a function of temperature varying different microreactor diameters from 1mm to 50  $\mu\text{m}$ .

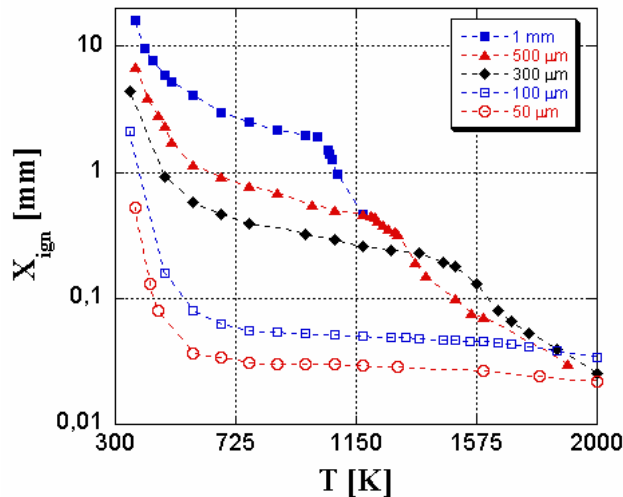


**Figure 57:** Ignition distance (y axis) versus reaction temperature(x axis) for a reactor with catalytic Pt-wall varying channel diameters with a constant velocity at the reactor entrance and subsequent parabolic velocity profile for stoichiometric H<sub>2</sub> oxidation.

Similar to Figure 7, we see the homogeneously dominated branch at higher reaction temperatures and heterogeneously dominated branch at lower reaction temperatures. Though we noticed a negligible amount of increase in ignition delay, but change in velocity distribution couldn't influence the quenching parameters. The entrance linear velocity is 6 m/s due to this flat entrance profile which is much smaller than the previous linear velocity, i.e. 9 m/s. This lower linear velocity, rather flow rate causes higher ignition delay in this case. Homogeneous reactions quenched below 300  $\mu\text{m}$  reactor diameters are seen in the size effect with flat entrance and fully developed velocity profile. It shows slightly higher ignition delay (especially at low T) than those with a fully developed flow but results are qualitatively same.

## APPENDIX E

### VARIATION OF PLATINUM SURFACE KINETICS ON IGNITION

Obviously, the results from a detailed reactor simulation study are dependent on the reaction kinetics used. To evaluate the sensitivity of our results to the kinetics used, we tested three different published reaction mechanisms for H<sub>2</sub>-oxidation on Pt surfaces. The results of this comparison are shown in Figure 58 where the ignition distance (in a logarithmic scale) is shown vs. reaction temperature for a 300 μm microchannel diameter.

In our study, so far we used a surface mechanism for H<sub>2</sub>-oxidation on Pt wall by Andrae et.al [63] in which the enthalpy of the surface species is defined as the sum of enthalpy of the corresponding species in gas phase and the heat of adsorption of this species, while the entropy of the species is assumed to be constant in the gas phase and on the surface (degrees of freedom are considered identical for both phases). Kinetic parameters for the forward reactions are explicitly given, while the rates of the back reactions are calculated from thermodynamic equilibrium. Results with this mechanism are represented by the filled squares in Figure 58.

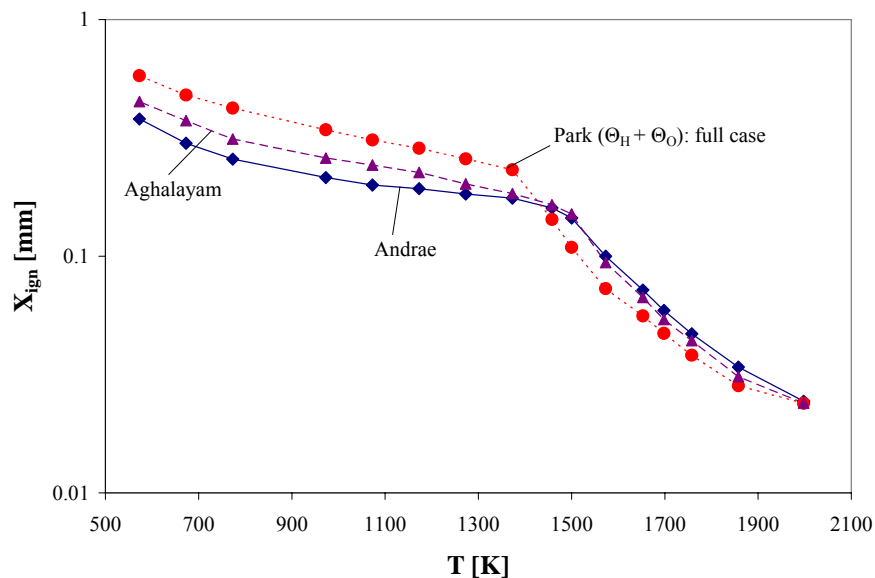


**Figure 58:** Ignition distance vs. temperature using Andrae et.al (filled diamonds and solid lines), Park et.al (filled circles and dotted lines) and Aghalayam et.al (filled triangles and dashed lines) surface kinetics. Kinetics by Park et.al is based on a clean Pt surface (full case:  $\Theta_H + \Theta_O$ ). The simulation is performed using  $300\mu\text{m}$  reactor diameter.

For comparison, we used another surface kinetics by Park. et.al [60] where the kinetic parameters have been explicitly defined for forward and back reaction steps on a clean Pt surface. In this plot filled circles represent the second surface kinetics and the effect of these two described different kinetics has been compared on  $\text{H}_2$ -oxidation ignition behavior.

The third curve in Figure 58 represents the ignition distance using elementary step kinetics from Aghalayam et.al. [62] (Filled triangles).

In the third kinetics, activation energy of the elementary steps are almost the same as Park et.al, but only pre-exponential factors are optimized taking the initial values from different experimental results. This kinetics is an extension of the mechanism given by Park et.al. The surface kinetics by Park et.al for the “full case” (circles) is based on adsorbate-adsorbate

interaction and the kinetics instead of referring a clean Pt surface, designates a H/O covered surface.

One can see from Figure 58 that at higher reaction temperatures, ignition distances using two mechanisms by Andrae and Aghalayam, are identical but at lower temperatures small deviations are observed. However, the differences are sufficiently small to be negligible in the context of the above discussion. Most significantly, for both plots, the transition point which separates two branches (as discussed above) remains at the same position. The ignition distance by Park et.al shows a noticeable deviation from the two other kinetics at all temperatures. Ignition delay decreases at higher temperature but at lower temperature heterogeneous ignition delay increases.

The coverage-dependent surface kinetics [16] was further studied (Figure 59) to see the impact of adsorbate-adsorbate interactions onto ignition behavior. Park et.al developed a thermodynamically consistent surface mechanism including adsorbate-adsorbate interactions. In this kinetics, they took into account the change in activation energies with varying coverage of surface species and calculated surface kinetic parameters on clean Pt surface and on O/H covered surface.

In Figure 59, ignition distance (logarithmic scale) is plotted against reaction temperatures for a 300  $\mu\text{m}$  reactor diameter with Pt wall. Three limiting cases for the surface kinetics from Park et.al were calculated on a clean Pt surface ( $\Theta_{\text{free}}=1$ ), an O covered surface ( $\Theta_{\text{o}}=1$ ) and the full kinetics (full case) including O and H surface coverage dependencies.

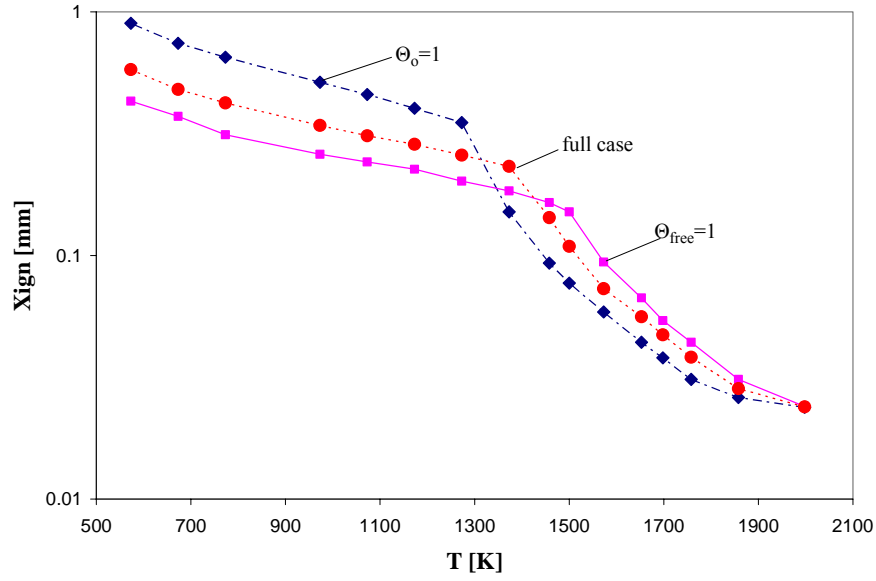


**Figure 59:** Ignition distance vs. temperature using Park et.al where surface mechanism is based on a surface having  $\Theta_o=1$  (filled diamonds and dotted lines), on a clean surface having  $\Theta_{free}=1$  (filled squares and solid lines) and on a surface having  $\Theta_o+\Theta_H$ , full case (filled circles and dotted lines). The simulation is performed for a  $300\mu\text{m}$  reactor diameter.

The plot shows that at higher reaction temperatures, the curve for  $\Theta_o=1$ , is shifted to lower ignition distances while at lower temperatures it shifts to higher ignition distances in comparison to the curves for  $\Theta_{free}=1$  and the “full case”. The transition point also changes its position and shifts to higher ignition distances. The ignition distance with the “full case” kinetics lies in between the ignition profile using the kinetics of  $\Theta_o=1$  and  $\Theta_{free}=1$  surfaces.

The surface having  $\Theta_o = 1$  shows higher activation energy (see Table 5 ) for some of the reaction steps than the surface having  $\Theta_{free} = 1$  and the “full case”, which contains O and H surface coverages. Higher amount of desorption energy of adsorbed O species, dissociation energy of adsorbed OH and H<sub>2</sub>O species (reaction step.4, 13, 15, 17 in Table 5) indicate that the surface has a high O surface coverage. This high value of activation energy hinders surface reactions in comparison to that using a clean surface ( $\Theta_{free} = 1$ ). A clean surface offers more free sites on the

surface and accelerates catalytic reactions the most. Due to the lower surface reaction rates for  $\Theta_o = 1$ , higher amount of gas phase radicals are expected to be available which enhances gas phase reactions at higher temperatures than that for  $\Theta_{\text{free}} = 1$  and “full case”. As a result, in Figure 59, lowest ignition delay is observed for  $\Theta_o = 1$  among these three cases. Conversely, highest ignition delay is observed for  $\Theta_o = 1$  at the low temperature regime of the ignition curve as this surface has the least rate of surface reactions while this low temperature branch favors surface reactions. If O coverage increases, overall reaction would be expected to behave homogeneously and the ignition profile would result an asymptotic behavior like inert wall. Therefore, surface with  $\Theta_o = 1$  is not a limiting approximation as it shows distinctly different behavior than a clean surface.

Due to the lower influence of surface for  $\Theta_o = 1$ , this surface prevails homogeneous ignition longer at higher temperatures. Consequently the transition point (between homogeneously dominated and heterogeneously dominated branches) shifts to lower temperature. The same reasoning holds for the shift in transition point for other two cases. As the surface for  $\Theta_{\text{free}} = 1$  has the highest surface influence among these three cases, therefore the transition point lies at higher temperature comparing other two cases.

The ignition profile for a “full case” should lie in between as it is considered to have H/O coverages initially which signifies higher energetics than a clean surface and lower than a full covered surface. Therefore the surface with “full case” kinetics manifests the ignition behavior which lies in between for  $\Theta_{\text{free}} = 1$  and  $\Theta_o = 1$ .

## APPENDIX F

### VALIDATION OF Pd SURFACE KINETICS FOR H<sub>2</sub>O<sub>2</sub> PRODUCTION

Surface kinetics calculated by H. Sellers on Pd surface [Table 16] using bond order conservation-morse potential (BOC-MP) approach, shows that the formation of H<sub>2</sub>O<sub>2</sub> on catalyst surface is very small. Among those given elementary steps in Table 16, reaction 31 shows the highest rate of H<sub>2</sub>O<sub>2</sub> production among four H<sub>2</sub>O<sub>2</sub> formation reactions, i.e. 29, 31, 33, 35. All of these reactions have same pre-exponential factors, which practically should not be identical. Looking at reactions 29 and 31, we can see that reaction 29 involves breaking of H-Pd bond and the formation of H-HO<sub>2</sub> bond, while reaction 31 consists of breaking of H-Pd bond, formation of H-HO<sub>2</sub> bond and on top of that the dissociation of H-H bond. Therefore, the pre-exp factor ( $k_0$ ) for reaction 29 might have larger value than that of reaction 31. But we do not see the difference in  $k_0$  in that energetics.

Secondly, if we calculate rate constants of all H<sub>2</sub>O<sub>2</sub> formation reactions using Table 15, we will get largest rate constant for reaction 2. Here, (S) represents the corresponding surface species.

**Table 15:** Rate constants calculation of H<sub>2</sub>O<sub>2</sub> formation from H.Sellers surface kinetics

---

H <sub>2</sub> O(S) + H(S) = H <sub>2</sub> O <sub>2</sub> (S) + PD(S) .....	(1) $k_1 = k_{o1} * \exp[-E_a/R*T] = 1.15E+16$
HO <sub>2</sub> (S) + H <sub>2</sub> (S) = H <sub>2</sub> O <sub>2</sub> (S) + H(S) .....	(2) $k_2 = 4.41E+20$
2OH(S) = H <sub>2</sub> O <sub>2</sub> (S) + PD(S) .....	(3) $k_3 = 3.61E+8$
OH(S) + HO <sub>2</sub> (S) = H <sub>2</sub> O <sub>2</sub> (S) + O(S) .....	(4) $k_4 = 3.11E+16$
H <sub>2</sub> O <sub>2</sub> (S) = H <sub>2</sub> O <sub>2</sub> + PD(S) .....	(5) $k_5 = 1.824E+17$

---

$$d[H_2O_2(S)]/dt = k_1*[HO_2(S)]*[H(S)] + k_2*[HO_2(S)]*[H_2(S)] + 2k_3*[OH(S)]^2 + k_4*[OH(S)]*[HO_2(S)] - k_5*[H_2O_2(S)]$$

Therefore, to increase H<sub>2</sub>O<sub>2</sub> production on Pd surface, rate of reaction 2 i.e. disproportionation reaction of HO<sub>2</sub>(S) and H<sub>2</sub>(S), has to be increased. H<sub>2</sub>O<sub>2</sub> formation in reaction 2 involves two surface species, i.e. HO<sub>2</sub>(S) and H<sub>2</sub>(S). These are two competing paths of forming reactants to produce more H<sub>2</sub>O<sub>2</sub> on surface. Now analyzing the rate of formation of those species, we see that the highest rate of formation of H<sub>2</sub>(S) [molecular adsorption of gas phase H<sub>2</sub> on catalyst surface] is 26 times larger than the highest rate of formation of HO<sub>2</sub>(S) via recombination of H(S) and O<sub>2</sub>(S). We can produce larger amount of H<sub>2</sub>(S) because the adsorption step of H<sub>2</sub> on Pd is non-activated. On other hand, HO<sub>2</sub>(S) breaks down into OH(S) much faster than forming H<sub>2</sub>O<sub>2</sub>(S) due to the lower activation barrier of that reaction steps involved. Reaction 36 and reaction 27 have no activation barrier due to the fact that formed OH(S) on surface is highly stable. If we can reduce the heat of chemisorption of OH(S) on Pd surface, then in one way we might increase H<sub>2</sub>O<sub>2</sub> production on catalyst.

Otherwise, if we increase the inlet gas flow rate which gears up the concentration of gas phase H<sub>2</sub>, as a result it will increase the concentration of adsorbed H<sub>2</sub>(S) than H(S), which might lead to another way of increasing H<sub>2</sub>O<sub>2</sub> production on catalyst surface.

In spite of that, feeding a fuel lean mixture in the reactor will end up with high conversion of H<sub>2</sub>O<sub>2</sub> on catalyst. In this regard, I checked the sensitivity of reactions 21, 23 and 27 in Table 16 because if we can make HO<sub>2</sub>(S) =>H<sub>2</sub>O<sub>2</sub>(S) reaction selective, then H<sub>2</sub>O<sub>2</sub> production might get enhanced, but they turned out to be the same in terms of H<sub>2</sub>O<sub>2</sub> production.

**Table 16:** Energetics of Pd surface under low surface coverage

No.	Reactions	cm,s,mol	β	J/mol
1.	H <sub>2</sub> + PD(S) => H <sub>2</sub> (S)	1.0	0.0	0.0
		<b>(0.32)</b>		
2.	H <sub>2</sub> (S) => H <sub>2</sub> + PD(S)	1E+13	0.0	27706.8
3.	H <sub>2</sub> (S) + PD(S) => 2H(S)	3.96E+21	0.0	36942.4
4.	2H(S) => H <sub>2</sub> (S) + PD(S)	3.96E+21	0.0	93195.6
	<b>2H(S) =&gt; H<sub>2</sub> + 2PD(S)</b>	<b>3.96E+21</b>	<b>0.0</b>	<b>(41500)</b>
5.	O <sub>2</sub> + PD(S) => O <sub>2</sub> (S)	1.0	0.0	0.0
		<b>(0.45)</b>		
6.	O <sub>2</sub> (S) => O <sub>2</sub> + PD(S)	1E+13	0.0	46178.0
7.	O <sub>2</sub> (S) + PD(S) => 2O(S)	3.96E+21	0.0	0.0
8.	2O(S) => O <sub>2</sub> + 2PD(S)	3.96E+19	0.0	183872.4
	<b>(2H(S) =&gt; H<sub>2</sub> + 2PD(S)</b>	<b>3.96E+21</b>	<b>0.0</b>	<b>(180000))</b>
9.	H(S) + O(S) => OH(S) + PD(S)	3.96E+21	0.0	48696.8
				<b>(79130)</b>
10.	OH(S) + PD(S) => H(S) + O(S)	3.96E+21	0.0	103270.8
11.	H(S) + O <sub>2</sub> (S) => OH(S) + O(S)	3.96E+21	0.0	0.0
12.	OH(S) + O(S) => H(S) + O <sub>2</sub> (S)	3.96E+21	0.0	194367.4
13.	H <sub>2</sub> (S) + O(S) => OH(S) + H(S)	3.96E+21	0.0	8815.8
14.	OH(S) + H(S) => H <sub>2</sub> (S) + O(S)	3.96E+21	0.0	119643.0
15.	H(S) + OH(S) => H <sub>2</sub> O(S) + PD(S)	3.96E+21	0.0	49536.4
				<b>(40500)</b>
16.	H <sub>2</sub> O(S) + PD(S) => H(S) + OH(S)	3.96E+21	0.0	78922.4
17.	OH(S) + H <sub>2</sub> (S) => H <sub>2</sub> O(S) + H(S)	3.96E+21	0.0	0.0
18.	H <sub>2</sub> O(S) + H(S) => OH(S) + H <sub>2</sub> (S)	3.96E+21	0.0	60871.0
19.	2OH(S) => H <sub>2</sub> O(S) + O(S)	3.96E+21	0.0	75564.0
				<b>(40500)</b>

20. $\text{H}_2\text{O}(\text{S}) + \text{O}(\text{S}) \Rightarrow 2\text{OH}(\text{S})$	3.96E+21	0.0	50376.0
--	----------	-----	---------

HO<sub>2</sub> FORMATION AND DISSOCIATION

21. $\text{H}(\text{S}) + \text{O}_2(\text{S}) \Rightarrow \text{HO}_2(\text{S}) + \text{PD}(\text{S})$	3.96E+21	0.0	0.0
22. $\text{HO}_2(\text{S}) + \text{PD}(\text{S}) \Rightarrow \text{H}(\text{S}) + \text{O}_2(\text{S})$	3.96E+21	0.0	69686.8
23. $\text{OH}(\text{S}) + \text{O}_2(\text{S}) \Rightarrow \text{HO}_2(\text{S}) + \text{O}(\text{S})$	3.96E+21	0.0	0.0
24. $\text{HO}_2(\text{S}) + \text{O}(\text{S}) \Rightarrow \text{OH}(\text{S}) + \text{O}_2(\text{S})$	3.96E+21	0.0	42399.8
25. $\text{HO}_2(\text{S}) + \text{PD}(\text{S}) \Rightarrow \text{O}(\text{S}) + \text{OH}(\text{S})$	3.96E+21	0.0	4617.8
26. $\text{O}(\text{S}) + \text{OH}(\text{S}) \Rightarrow \text{HO}_2(\text{S}) + \text{PD}(\text{S})$	3.96E+21	0.0	144411.2
27. $\text{HO}_2(\text{S}) + \text{H}(\text{S}) \Rightarrow 2\text{OH}(\text{S})$	3.96E+21	0.0	0.0
28. $2\text{OH}(\text{S}) \Rightarrow \text{HO}_2(\text{S}) + \text{H}(\text{S})$	3.96E+21	0.0	160783.4

H<sub>2</sub>O<sub>2</sub> FORMATION AND DISSOCIATION

29. $\text{HO}_2(\text{S}) + \text{H}(\text{S}) \Rightarrow \text{H}_2\text{O}_2(\text{S}) + \text{PD}(\text{S})$	3.96E+21	0.0	75564.0
30. $\text{H}_2\text{O}_2(\text{S}) + \text{PD}(\text{S}) \Rightarrow \text{HO}_2(\text{S}) + \text{H}(\text{S})$	3.96E+21	0.0	41140.4
31. $\text{HO}_2(\text{S}) + \text{H}_2(\text{S}) \Rightarrow \text{H}_2\text{O}_2(\text{S}) + \text{H}(\text{S})$	3.96E+21	0.0	13013.8
32. $\text{H}_2\text{O}_2(\text{S}) + \text{H}(\text{S}) \Rightarrow \text{HO}_2(\text{S}) + \text{H}_2(\text{S})$	3.96E+21	0.0	34843.4
33. $2\text{OH}(\text{S}) \Rightarrow \text{H}_2\text{O}_2(\text{S}) + \text{PD}(\text{S})$	3.96E+21	0.0	177995.2
34. $\text{H}_2\text{O}_2(\text{S}) + \text{PD}(\text{S}) \Rightarrow 2\text{OH}(\text{S})$	3.96E+21	0.0	0.0
35. $\text{OH}(\text{S}) + \text{HO}_2(\text{S}) \Rightarrow \text{H}_2\text{O}_2(\text{S}) + \text{O}(\text{S})$	3.96E+21	0.0	69686.8
36. $\text{H}_2\text{O}_2(\text{S}) + \text{O}(\text{S}) \Rightarrow \text{OH}(\text{S}) + \text{HO}_2(\text{S})$	3.96E+21	0.0	0.0
37. $\text{H}_2\text{O}_2(\text{S}) \Rightarrow \text{H}_2\text{O}_2 + \text{PD}(\text{S})$	1.0E+13	0.0	59191.8
38. $\text{H}_2\text{O}_2 + \text{PD}(\text{S}) \Rightarrow \text{H}_2\text{O}_2(\text{S})$	1.0E+13	0.0	0.0
39. $\text{H}_2\text{O}(\text{S}) \Rightarrow \text{H}_2\text{O} + \text{PD}(\text{S})$	1.0E+13	0.0	41980.0
			<b>(41900)</b>
40. $\text{H}_2\text{O} + \text{PD}(\text{S}) \Rightarrow \text{H}_2\text{O}(\text{S})$	1.0E+13	0.0	0.0

---

In the above table pre-factor values within parenthesis represents measured by Johansson et.al [67] which we have used for the ignition study with Pd surface in our work to directly compare with sellers kinetics. In this modified kinetics, there is no molecular adsorption (no H<sub>2</sub>(S) or O<sub>2</sub>(S)) considered on the surface unlike sellers kinetics except H<sub>2</sub>O produced in gas phase adsorbs directly on the surface without any activation barrier. In Sellers kinetics no H, O, OH formed in gas phase adsorbs on the surface which indicates no atomic adsorption is in there. Surface species like OH(S) is formed either through decomposition of HO<sub>2</sub>(S) or H<sub>2</sub>O<sub>2</sub>(S) and

different recombination reaction among HO containing species. In experiments activation barrier for OH(S) formation (in reaction (9)) is higher than calculated activation energy value by Sellers, therefore OH(S) with modified kinetics destabilizes faster than with sellers kinetics. In addition to that, though the rates of desorption of H<sub>2</sub>O(S) (reaction 39) are similar in both cases but formation of H<sub>2</sub>O via recombination of OH(S) (reaction 15 and 19) has larger activation barrier in case of sellers kinetics, which reduces conversion than with the modified kinetics. Ultimately in case of Sellers kinetics, Pd surface gets covered with O coverage after the reaction while desorption of intermediate surface species is so fast with modified kinetics compared to Sellers kinetics that it leaves an almost bare catalyst surface at the end of the reaction. The numerical calculation shows the higher conversion (99.3%) achieved with modified kinetics than that with Sellers kinetics (97%). Overall energetics is quite different in those two cases.

In improving the formation of H<sub>2</sub>O<sub>2</sub> in gas phase we check the surface coverage at low temperatures. In gas phase, the selectivity of H<sub>2</sub>O<sub>2</sub> is almost nil at low temperature like 440°C, but modifying those parameters if we can diminish the activation barrier of desorption step of H<sub>2</sub>O<sub>2</sub>(S) in gas phase, which will improve the selectivity of that particular product. At this temperature, surface coverage of the important species is tabulated in Table 17 at the end of the reaction.

**Table 17:** Surface coverage of main species on Pd surface at 713K with modified kinetics

Species (i)	Maximum Surface Coverage ( $\theta_i$ )
H <sub>2</sub> O <sub>2</sub>	1.3*10 <sup>-11</sup>
HO <sub>2</sub>	3*10 <sup>-06</sup>
H <sub>2</sub>	2.9*10 <sup>-04</sup>
OH	2.3*10 <sup>-01</sup>
H	6.8*10 <sup>-01</sup>

## BIBLIOGRAPHY

1. B.Lewis and G.v.Elbe, *Combustion and Flames and Explosions of Gases*. 1987, New York: Academic Press.
2. G.Veser, *Chem.Eng.Sci.*, 2001. **56**: p. 1265.
3. G.Veser, et.al., *Micro-Electro-Mechanical Systems (MEMS) (ASME-DSC)*, 1988. **66**: p. 199.
4. G. Veser and L.D. Schmidt, *AIChE*, 1996. **47**: p. 1077.
5. Editorial, *Fuel Processing Technology*, 2003. **83**: p. 1.
6. Editorial, *Science*, 2004. **305**: p. 917.
7. D.G.Vlachos, *Chem.Eng. Sci*, 1996. **51**(10): p. 2429.
8. Enomoto.K, F.S., Kobayashi.Y, *Hydrogen Energy Prog.*, 1981. **2**: p. 1149.
9. Griffin T.A, Pfefferle.L.D., *AIChE.J*, 1990. **36**: p. 861.
10. M.A.Mueller, R.A.Yetter, and F.L.Dryer, *Int.J.Chem.Kinetics*, 1999. **31**(10): p. 705.
11. G.Veser, et al., *Stud.Surf.Sci.Catal.*, 1999. **122**: p. 237.
12. K.Jensen, *Chem.Eng. Sci*, 2001. **56**: p. 293.
13. S.Chattopadhyay and G. Veser, *Proc. IChE, CHEMCON*, 2001, p. 65.
14. F.Schueth et.al, *Surf. Sci.Catal*, 2000. **130**: p. 437.
15. Ehrfeld.W, Hessel.V, and Lowe. H, *Microreactors: New technology for modern chemistry*. 2000, Weinheim: Wiley-VCH.
16. Andrea. W Chow, *AIChE J*, 2002. **48**(8): p. 1590.
17. K.D.Wise and K.Najafi, *Science*, 1991. **254**(5036): p. 1335.
18. J.M.Ramsey, S.C Jacobson, and R.S.Foote, *Microreaction Technology: Proc. The First International Conference on Microreaction Technology*, Editor: W.H.Ehrfeld, 1998. **IMRET-1**: p. 204.

19. Lowe H and E. W, *Electrochimica Acta*, 1999. **44**.
20. Maluf, N., *An introduction to microelectromechanical systems engineering*. 2000, Boston: Artech House Publishers.
21. R.Srinivasan and et.al., *AIChE.J*, 1997. **43**: p. 3059.
22. S. Srinivas, A.Dhingra, and E.G. H. Im, *Applied Catalysis A*, 2004. **274**: p. 285.
23. Gunther Kolb and V. Hessel, *Chemical Engineering Journal*, 2004. **98**: p. 1.
24. S.K.Ajmera, M.W.Losey, and K.F.Jensen, *AIChE.J*, 2001. **47**(7): p. 1639.
25. M.W.Losey, M.A.Schmidt, and K.F.Jensen, *Ind.Eng.,Chem.Res.*, 2001. **40**(12): p. 2555.
26. T.Floyd, K.Jensen, and M.Schmidt. *Proc. 4th Int.Conf.Microreaction Technol*. 2000. Atlanta, GA.
27. Ashish V.Pattekari and M. V.Kothare, *J.MEMS*, 2004. **13**(1): p. 7.
28. A.Gavrilidis, et al., *Trans IChemE*, 2002. **80**, part A: p. 3.
29. Hickman D.A and L.D.Schmidt, *Science*, 1993. **259**: p. 343.
30. P.Cho and C.K.Law, *Combust. Flame*, 1986. **66**: p. 159.
31. B.Kasemo et.al, *Surf. Sci*, 1997. **376**: p. 297.
32. Pfefferle L.D and W.M. Griffin T.A, Crosley D.R and Dyer. M, J and Crosley D.R, *Combust. Flame*, 1989. **76**: p. 339.
33. Pfefferle L.D and W.M. Griffin T.A, Crosley D.R and Dyer. M, *Combust. Flame*, 1989. **76**: p. 325.
34. Pfefferle, L.D., and Pfefferle W.C, *Catalysis Rev.Sci.Eng*, 1987. **29**: p. 219.
35. Fisher.G.B, Gland. J.L, and Schmiegel.S.J, *J.Vac.Sci.Technol*, 1982. **20**: p. 518.
36. Verheij.L.K and Hugenschmidt.M.B, *Surf. Sci*, 1998. **37**: p. 416.
37. Rinnemo.M, Fassihi.M, and Kasemo.B, *Chem.Phys.Lett*, 1993. **60**: p. 211.
38. Fernandes.N.E, Park.Y.K, and Vlachos.D.G, *Combust. Flame*, 1999. **118**: p. 164.
39. Michael. T. Janicke, Ferdi Schueth, and K. Schubert, *J. Catal*, 2000. **191**: p. 282.

40. Dean A.M, S. D.C, and a.W. E.E, *Combust. Flame*, 1978. **32**: p. 78.
41. Hottel H.C, et al. in *Tenth symposium international on combustion, The combustion institute*. 1965. Pittsburgh, PA.
42. R.A.Yetter, F.L.Dryer, and H.Rabitz, *Combust. Sci. and Tech*, 1991. **79**: p. 97.
43. G.Hadman, H.W.Thompson, and C.N.Hinshelwood. *Royal Society of London, Series A*. 1932. London.
44. V.P.Zhdanov and B.Kasemo, *Appl.Surf.Sci*, 1994. **74**: p. 147.
45. G.K.Hori and L.D.Schmidt, *J. Catal*, 1975. **38**(1-3): p. 335.
46. M. Rinnemo, et al., *Surf. Sci*, 1997. **376**: p. 297.
47. F.Zaera, J.Liu, and M.Xu, *J.Chem.Phys*, 1997. **106**: p. 4204.
48. M.Ehsasi, et al., *J.Chem.Phys*, 1989. **91**(8): p. 4949.
49. H.P.Bonzel and J.J.Burton, *Surf. Sci*, 1975. **52**: p. 223.
50. Hickman D.A and L.D.Schmidt, *J. Catal*, 1992. **163**(2): p. 267.
51. X.Song, et al. *Proc. 23rd International Symposium on combustion*. 1990: The Combustion Institute.
52. Popp. P, Smooke M, and B. M. in *26th Int. Symp. on Combustion*. Pittsburgh.
53. Popp. P and Baum. M, C., *Combust. Flame*, 1997, 108, 327.
54. I.Ming Hsing, et al., *Chem.Eng.Sci.*, 2000. **55**: p. 3.
55. D.J.Quiram, et al., *Chem.Eng.Sci*, 2000. **55**: p. 3065.
56. C.T.Goralski Jr. and L.D.Schmidt, *Chem.Eng.Sci*, 1999. **54**: p. 5791.
57. G.Veser and J.Frauhammer, *Chem.Eng. Sci*, 2000. **55**: p. 2271.
58. O.Deutschmann, et al. *Twenty-Sixth Symposium (International) on Combustion*. 1996. Pittsburgh, PA: The Combustion Institute.
59. P.Aghalayam, P.A.Bui, and D.G.Vlachos, *Combustion Theory Modelling.*, 1998. **2**: p. 515.

60. Y. K. Park, P. Aghalayam, and D.G.Vlachos, *J.Phys.Chem.A.*, 1999. **103**: p. 8101.
61. Shustorovich.E and Sellers.H, *Surf.Sci.Rep*, 1998. **31**: p. 1.
62. P.Aghalayam, Y.Park, and D.G.Vlachos, *AIChE.J*, 2000. **46**(10): p. 2017.
63. J.C.G Andrae and P.H.Bjoernbom, *AIChE. J*, 2000. **46**(7): p. 1454.
64. D.G.Vlachos, *Chem.Eng.Sci.*, 1998. **53**: p. 157
65. R.J.Kee, F.M.Rupley, et.al. M.E.Coltrin, *CHEMKIN Collection Release 3.6*. 2000.
66. GRI and mechanism, [http://www.me.berkeley.edu/gri\\_mech](http://www.me.berkeley.edu/gri_mech).
67. A.Johansson, M.Foersth, and A.Rosen, *Surf. Sci*, 2003. **529**: p. 247.
68. Giovangigli, V. and M. D. Smooke, *Combust.Sci.Tech*, 1987. **53**: p. 23.
69. J. Warnatz, et al., *Combust. Flame*, 1994. **96**: p. 393.
70. M.Foersth, *Combust. Flame*, 2002. **130**: p. 241.
71. W.R.Williams, C.M.Marks, and L.D.Schmidt, *J.Phys.Chem*, 1992. **96**: p. 5922.
72. M. Rinnemo, et al., *Combust. Flame*, 1997. **111**: p. 312.
73. Andrae, J, 2002, *PhD thesis*, Royal Institute of Technology: Sweden.
74. G.Veser, M.Ziauddin, and L.Schmidt, *Catal Today*, 1999. **47**: p. 219.
75. Dhammike P.Dissanayake and Jack H.Lunsford, *J. Catal*, 2003. **214**: p. 113.
76. P.Paredes Olivera, E.M.Patrito, and Harrell Sellers, *Surf. Sci*, 1994. **313**: p. 25.
77. G.Veser, A.Wright, and R.Caretta, *Catalysis Letters*, 1999. **58**: p. 199.
78. D.L.Weissman-Wenocur and W.E.Spicer, *Surf. Sci*, 1983. **133**: p. 499.
79. D.Dissanayake and J.H.Lunsford, *J. Catal*, 2002. **206**: p. 173.
80. Adris A.M and et.al, *Can.J.Chem.Eng*, 1996. **74**: p. 177.
81. J.Zhu, D.Zhang, and K.D.King, *Fuel*, 2001. **80**: p. 899.
82. J.Agrell and et.al, *J. Catal*, 2003. **219**: p. 389.

83. E.C.Wanat, K.Venkataramana, and L.D.Schmidt, *Appl.Catal.A*, 2004. **276**: p. 155.
84. Jens.R.Rostrup-Nielsen, *Catal Today*, 2002. **71**: p. 243.
85. M.J.Kahlich, H.A.Gasteiger, and R.J.Behm, *J. Catal*, 1997. **171**: p. 93.
86. T.V.Chowdhury and D.W.Goodman, *J. Catal*, 2000. **192**: p. 316.
87. R.Metkemeijer and P.Achard, *J.Power Sources*, 1994. **49**: p. 271.
88. X.Ouyang and R.S.Besser, *J.Power Sources*, 2004. **article in press**.
89. Y.Choi and H.G.Stenger, *J.Power Sources*, 2004. **129**: p. 246.
90. B.Lewis and G.v.Elbe, *Combust. Flame*, 1986. **63**: p. 135.
91. P. Aghalayam, Y. K. Park, and D.G.Vlachos. *A detailed surface reaction mechanism for CO oxidation on Pt*. in *Combustion Institute*. 2000.
92. Constantin Bratianu and Cristina Opera, *Key Engineering Materials*, 2003. **243-244**: p. 231.
93. Bowman C.T. in *Twenty-Fourth Symposium (International) on Combustion*. 1992. Pittsburgh, PA: The Combustion Institute.
94. Miller J.A and Bowman C.T, *Int. J.Chem. Kin*, 1991. **23**: p. 289.
95. P.Glarborg, D.Kubel, and K.Dam-Johansen, *Combust.Sci and Tech*, 1995. **110-111**: p. 461.
96. Atkins, P., *Physical Chemistry*. Sixth ed. 1999, New Jersey: W.H.Freeman & Company.
97. J.Geankopolis, C., *Transport process and unit operation*. 3rd ed. 1999, N.J: Prentice Hall Inc.